https://doi.org/10.15388/vu.thesis.333
https://orcid.org/0000-0001-8437-5982

VILNIUS UNIVERSITY
CENTER FOR PHYSICAL SCIENCES AND TECHNOLOGY

Dovilė Lengvinaitė

Modeling of NMR spectral parameters of complex molecular systems by quantum mechanics and molecular dynamics methods

DOCTORAL DISSERTATION

Natural Sciences,
Physics (N 002)

VILNIUS 2022

The dissertation was prepared between 2016 and 2021 at the Institute of Chemical Physics, Vilnius University. The research was supported by Research Council of Lithuania.

Academic supervisor – Assoc. Prof. Dr. Kęstutis Aidas (Vilnius University, natural sciences, physics – N 002).

This doctoral dissertation will be defended in a public meeting of the Dissertation Defence Panel:

Chairman – Prof. Habil. Dr. Sigitas Tumkevičius (Vilnius University, physical sciences, chemistry – N 003).
Members:
doc. dr. Justinas Čeponkus (Vilnius University, physical sciences, physics – N 002),
dr. N. Arul Murugan (Delhi University, India, physical sciences, physics – N 002),
dr. Jelena Tamulienė (Vilnius University, physical sciences, physics – N 002),
dr. Linas Vilčiauskas (Center for physical sciences and technology, physical sciences, chemistry – N 003).

The dissertation shall be defended at a public meeting of the Dissertation Defence Panel at 11 o'clock on 1st of July, 2022 in A101 meeting room, National Center of Physical and Technologies Sciences.
Address: Saulėtekio av. 3, Vilnius, Lithuania.
Tel. +370 5 223 4594; e-mail: dovile.lengvinaite@ff.vu.lt

The text of this dissertation can be accessed at the libraries of Vilnius University and the Centre of Physical Sciences and Technology, as well as on the website of Vilnius University:
www.vu.lt/lt/naujienos/ivykiu-kalendorius

https://doi.org/10.15388/vu.thesis.333
https://orcid.org/0000-0001-8437-5982

VILNIAUS UNIVERSITETAS
FIZINIŲ IR TECHNOLOGIJOS MOKSLŲ CENTRAS

Dovilė Lengvinaitė

Sudėtingų molekulinių sistemų BMR spektrinių parametrų modeliavimas kvantinės mechanikos ir molekulinės dinamikos metodais

DAKTARO DISERTACIJA

Gamtos mokslai
Fizika (N 002)

VILNIUS 2022

Disertacija rengta 2016–2021 Vilniaus universitete.
Mokslinius tyrimus rėmė Lietuvos mokslo taryba.

Mokslinis vadovas – doc. dr. Kęstutis Aidas (Vilniaus universitetas, gamtos mokslai, fizika – N 002).

Gynimo taryba:
Pirmininkas – prof. dr. Sigitas Tumkevičius (Vilniaus universitetas, gamtos mokslai, chemija – N 003).
Nariai:
doc. dr. Justinas Čeponkus (Vilniaus universitetas, gamtos mokslai, fizika – N 002),
dr. N. Arul Murugan (Delhi universitetas, Indija, gamtos mokslai, fizika – N 002),
dr. Jelena Tamulienė (Vilniaus universitetas, gamtos mokslai, fizika – N 002),
dr. Linas Vilčiauskas (Fizinių ir technologijos mokslo centras, gamtos mokslai, chemija – N 003).

Disertacija ginama viešame Gynimo tarybos posėdyje 2022 m. liepos mėn. 1 d. 11 val. Nacionalinio fizinių ir technologijos mokslo centro A101 auditorijoje. Adresas: (Saulėtekio al., 3, A101, Vilnius, Lietuva), Tel. +370 5 223 4594; el. paštas dovile.lengvinaite@ff.vu.lt

Disertaciją galima peržiūrėti Vilniaus universiteto ir Fizinių ir technologijos mokslo centro bibliotekose ir VU interneto svetainėje adresu: *https://www.vu.lt/naujienos/ivykiu-kalendorius*

ACKNOWLEDGEMENTS

The knowledge and experience gained during the years of my PhD studies widely exceeds the content of this thesis. I would like to take the opportunity and express my most sincere gratitude to the many people who made it possible.

First, I would like to thank my supervisor, Assoc. Prof. Kęstutis Aidas, for introducing me to the science, long before the actual start of the PhD studies, for guidance, for the immense patience and support, for encouraging and, sometimes, pushing me forward.

Second, I wish to thank my scientific advisors, Prof. Francesca Mocci for welcoming me to Cagliari University and challenging me with new and interesting tasks, and for, together with Prof. Aatto Laaksonen, giving new scientific insights.

Third, I am grateful to all my colleagues at the Institute of Chemical Physics for creating a nice and friendly atmosphere to work in. Many thanks go to Valdas, Justinas, and Vidita for sharing their knowledge and encouragement. My special thanks go to NMR experimental group, especially Vytautas Balevičius, Vytautas Klimavičius, and Liudvikas Kimtys for collaboration and NMR experimental results.

Further, I would like to sincerely thank *Molecule* gang – Martynas, Rasa, Rimantė, Sonata, Gerda, and Jogilė for the joyful atmosphere, moral support, inspiration, and also fruitful discussions in the office.

Finally, I am grateful to my parents Daiva, and Rimantas for their continuous support, appreciation, and encouragement and keep interested in my academic achievements. Thank you, dear brother Andrius, and his beloved Agnė for your company and passion for board games. I would like to thank Ovidijus for continuous support and for seeing in me much more than I could. I am thankful for the unconditional love and support throughout the entire thesis process and every day.

Contents

LIST OF ABBREVATIONS

AA – acetic acid
ACN – acetonitrile
B3LYP – Becke'3 functional combined with Lee, Yand and Parr.
CCSD – coupled cluster singles and doubles
CHELPG – charges from electrostatic potentials using a grid-based method
DCM – dichloromethane
DFT – density functional theory
DFT/MM – density functional theory/molecular mechanics
FF – force field
GAFF – generalized amber force field
GIAO – gauge-including atomic orbitals
HF – Hartree-Fock
IL – ionic liquid
KT3 – Keal-Tozer functional no.3
LJ – Lennard-Jones
MD – molecular dynamics
MM – molecular mechanics
MP2 – Møller-Plesset perturbation theory
NMR – nuclear magnetic resonance
OPLS – optimized potential for liquid simulations
PBE0 – Perdew, Burke and Ernzerhof functional
QM – quantum mechanics
QM/MM – quantum mechanics/molecular mechanics
RDF – radial distribution function
RESP – restrained electrostatic potential
RTIL – room temperature ionic liquid
PCM – polarizable continuum model
SDF – spatial distribution function
TIP3P – transferable intermolecular potential 3 points
TIP4P_ew – modified 4-site transferable intermolecular potential
TMS – tetramethylsilane

Ionic liquids designations:
[C4mim][Cl] – 1-butyl-3-methylimidazolium chloride
[C10mim][Cl] – 1-decyl-3-methylimidazolium chloride
[C10mim][Br] – 1-decyl-3-methylimidazolium bromide

INTRODUCTION

Ionic liquids (ILs) are liquid salts, typically composed of bulky and asymmetrical organic cations and organic or inorganic anions with their melting points below 100°C. [1] Many ILs remain liquid at or near room temperature and are called room–temperature ionic liquids (RTILs). The first report is generally credited to the P. Walden with the first documented liquid salt material at ambient temperature in 1914.[2] He synthesized an ionic salt, ethylammonium nitrate, which displays a melting point of 12°C and a rather low viscosity. However, this early report did not receive much consideration from various scientific communities and it was not recognized that chemistry in such solvents would become of widespread interest. Later, Hurley and Wier recognized the potential benefit of decreasing melting points of molten salt materials via the synthesis of organic chloroaluminates and it was reported in 1951.[3] The obtained organic chloroaluminates are now considered as the first generation of ILs. Studies of these compounds started in the 1970s.[4] In the 1990s, it became clear that many ion combinations form air- and water-stable ILs.[5,6] Since then ILs were proposed as solvents for organic synthesis and became increasingly popular in academia and industry. By a careful selection of cation–anion combinations, it is possible to prepare a large variety of ILs. These pioneering works and significant breakthroughs in IL communities opened up avenues for a surge of research on ILs and initiated paramount research activities across areas of physics, chemistry, biology, material science and engineering, and environmental science, which are subjected to numerous reviews and other published materials.[7–17]

ILs have attracted attention for their excellent physicochemical characteristics, such as negligible volatilities, reasonable conductivity-viscosity properties, high thermal stability, wide electrochemical windows, high thermal- and chemical-oxidative stabilities, as well as capabilities to dissolve liquid and solid solute materials.[18,19] ILs are often considered as green solvents due to its extremely low vapor pressure, high thermal stability, and excellent capability in replacing the traditional volatile organic solvents. The environmentally benign solvent also promotes ease of recovery and recycling ability.[20] Additionally, these fascinating physicochemical qualities are related to hydrophilicity/hydrophobicity, polarity, and solvent power as well as their microstructural organization, and these properties can be widely tuned by combinations of different cations and anions.[18,19] Therefore, ILs can be tailored and tuned

for specific tasks, and they are referred to as designer solvents. These striking features render ILs as dependable candidates and benign alternatives to conventional molecular solvents in material synthesis to control precise structures and patterns of nanomaterials;[8,21] valuable reaction media in catalytic chemistry;[21,22] promising working fluids in separation technology; [9,10] unique tunable platforms to design task-specific advanced materials;[8,9] reliable solvent electrolytes in electrochemical devices with tunable electrochemical windows and ion conductivities.[11–13,23–25] As a result of an enormous number of promising applications, the playing field for additional applications and related investigations for physicists, chemists, biologists, materials scientists, and engineers is vast and has yet to see its limitation.

The most important cations are imidazolium, pyridinium, pyrrolidinium, tetraalkylammonium, phosphonium and choline. Anions are weakly basic inorganic or organic compounds that have a negative charge. Although numerous possible combinations of cations and counter anions are available, much research has focused on imidazolium-based ionic liquids due to the fact that they are relatively easy to synthesize as well as air- and moisture-stable. Imidazolium-based ILs are nitrogen-rich heteroatomic compounds with a low melting point, high chemical stability, and high ionization performance.[26] Imidazolium-based ILs offer many useful applications in cellulose processing,[27] lubrication,[14] solvent-free electrolytes for solar cells,[28] CO_2 capture,[29,30] or extraction of metals from aqueous solutions.[15,31]

It is worth mentioning that ILs are typically not used in their pure form but as co-solvents or additives. In this role, they demonstrate improved and more desirable thermodynamic and transport properties in many processes. Many of them are very hygroscopic and may readily absorb considerable amounts of water from the atmosphere.[32] Water may have both detrimental and favorable effects on the properties of ILs. For example, even trace amounts of water were seen to significantly diminish the solubility of cellulose in the 1-butyl-3-methyl-imidazolium chloride, [C4mim][Cl], IL.[27] On the other hand, the role of water was recognized as crucial for the stabilization of the native state of the cytochrome c protein in the biocompatible IL over periods of time significantly exceeding those seen in protein's natural aqueous environment.[33,34] Mixtures of IL and water may also exhibit unexpected behavior such as recently demonstrated increasing viscosity induced by heating the sample.[35] ILs are notoriously viscous, and the addition of a molecular cosolvent reduces the viscosity considerably and thus renders these liquids easier to handle.[36,37] The

conductivities of pure ILs are typically rather low, but they are markedly higher for their mixtures with traditional solvents.[38] Mixtures of IL and acetonitrile were seen to possess an improved electrochemical window as compared to those of pure components,[39] and they have been used as electrolytes in electrochemical production of graphene[40] or for the electrocatalytic enhancement of the reduction of CO_2 to CO.[41]

To rationalize the modulating effect of the molecular solvent on the properties of the IL, a thorough understanding of intermolecular interactions between the constituent ionic and molecular species that govern molecular association in the mixture is crucial.[16,42] There is a general trend for polar solvents to be capable of breaking the ion pairs into separate ions, while nonpolar solvents tend to favor ion aggregation.[43,44] This can be exemplified by the association constants of 1-butyl-3-methyl-imidazolium tetrafluoroborate, which range from the order of 10^5 dm^3/mol in dichloromethane to 10^{-1} dm^3/mol in water.[45] Dimethyl sulfoxide has also demonstrated the capability of breaking ionic aggregates into separate ions,[46–49] but, here too, some ILs have displayed slight association at high dilutions.[50,51] Remarkably, however, higher-order supramolecular ionic clusters were found to persist at rather low concentrations of [C4mim][Cl] IL in dimethyl sulfoxide.[50] Even though acetonitrile is rather similar to dimethyl sulfoxide in polarity, it does not seem to break ionic aggregates into separate ions, apparently due to the poorer hydrogen-bond accepting abilities.[48,52–54] At low concentrations in nonpolar solvents, ILs tend to form supramolecular aggregates,[45,47,55–57] although lone contact ion pairs were seen to be the dominant association pattern for some ILs in chloroform[51] and dichloromethane.[58,59] However, the dissociation* of [C4mim][Cl] ion pairs into separate ions in solutions of chloroform and carbon tetrachloride has been observed very recently.[60,61]

Water is the most abundant fluid on earth and it is important in many biological and chemical systems. Almost all biological activity goes on in aqueous systems. Water has unique physicochemical properties based on strong hydrogen bonding.[62] Water has long been regarded as inimical to pure IL science because the presence of trace amounts of water significantly impairs the remarkable properties of pure ILs. Even a small amount of water can dramatically influence the properties of ILs such as diffusion coefficient,[63] viscosity,[37] polarity,[64] and surface tension.[65] Miscibility is impor-

*In this thesis, dissociation will be defined as the process when contact ion pairs break into free solvated ions.

tant in considering the properties of IL/water mixtures. It is well known that the miscibility of ILs with water depends strongly on the nature of anions. In general, ILs with highly-fluorinated and charge-delocalised anions, such as bis(trifluoromethanesulfonyl)imide and PF_6^-, tend to form hydrophobic ILs and are immiscible with water. On the other hand, ILs with hydrophilic ions such as halide (i.e. Cl^- or Br^-), phosphate ($R_2PO_4^-$), or carboxylate ($RCOO^-$) are mostly miscible with water.[66] It has been reported for imidazolium-based ILs that hydrophobicity increases with the length of the cations alkyl tail and the size of anions.[37] The mixtures of IL and water may acquire unique properties which are not necessarily associated with any of the two components.[17,33–35,67] For example, the mixtures of phosphonium IL and water can be used for effective extraction of water-soluble proteins through a temperature-controlled reversible transition between homogeneous and separated liquid-liquid phases.[32,68]

To disclose the molecular mechanisms behind the physicochemical properties of IL/water mixtures, various experimental and theoretical techniques have been called in order to provide a detailed insight into the molecular structure and dynamics of these heterogeneous systems.[16,17,69,70] In particular, classical molecular dynamics (MD) simulations have led to the general conclusion that solitary water molecules are dispersed throughout the bulk of the IL when the water content is rather low.[69,71–75] Under these circumstances, the isolated water molecules are found to primarily form hydrogen bonds with the anions,[71,72,75] acting as bridges between them.[74,76] When the molar fraction of water increases, clusters of water molecules begin to emerge,[72,73,76] and the nanostructural organization of the mixture is enhanced.[77] Eventually, a continuous water network is formed, which percolates the entire system and surrounds the ionic clusters.[73–76]

The hydrogen bond is a unique phenomenon in structural chemistry and biology. Hydrogen bonding plays a decisive role in the structure, function, and dynamics of a wide range of molecular systems.[78,79] It causes molecular network formation in liquids like water or determines the configuration of numerous biomolecules, like DNA and proteins,[80,81] polymers[82] or other complex supermolecular structures, highly relevant for life and engineering of new materials. Carboxylic acids interact mainly through hydrogen bonding. The carboxyl group can be both a hydrogen bond donor and an acceptor. The double hydrogen bonding character enables carboxylic acids to establish a strong intermolecular bond which leads them to form very stable dimers. Acetic acid

is considered as a simple organic acid and an important substance in biochemistry. Molecular association in this carboxylic acid has been the subject of extensive investigations.

It is well known that in the gas phase the predominant structure of acetic acid is a cyclic dimer and in the solid phase (crystalline form) the structure is described as hydrogen bonded linear chains.[83,84] In liquid acetic acid (AA), a dynamic equilibrium between various kinds of AA molecular aggregates, primarily cyclic dimers and linear chains, is established.[85] However, experimental measurements have led to rather conflicting conclusions concerning the amount of each type of association of AA molecules in the neat liquid. Neutron diffraction experiments[86] and more recent low-frequency ultrafast time-domain Raman spectroscopic measurements[87] indicate that liquid AA is predominantly composed of cyclic dimers. Conversely, Raman[88] and large-angle X-ray scattering experiments,[89] as well as IR absorption measurements[90] indicate linear solid-state-like chains to be the main association motif for AA molecules in the neat liquid. More recent ultrafast coherent Raman scattering measurements of carbonyl stretching indicate clearly the presence of cyclic dimers which coexist with other configurations of hydrogen bonding, presumably linear chain structures.[91] The splitting of the hydroxyl oxygen signal in the X-ray emission spectrum of liquid AA could also indicate at least two different hydrogen bonding configurations between AA molecules.[92] Raman scattering experiments have also been invoked to show that, in addition to cyclic dimers and linear chains, a considerable amount of unassociated AA monomers coexist in the liquid.[93] Eminent formation of cyclic trimers and linear chains of at least three AA molecules in the neat liquid has been recently proposed based on neutron scattering measurements.[94] Molecular simulations generally show that both cyclic and linear aggregates are formed in liquid AA, yet an unequivocal conclusion regarding the balance between different aggregation types seems not to have been reached.

Nuclear magnetic resonance, NMR, spectroscopy has proven to be a useful tool for the investigations of the structure and dynamics of molecular systems, especially in many areas of chemistry and biology. [95,96] Over the years, NMR spectroscopy has given access to unique information of molecular systems, for example, chemical shifts, nuclear Overhauser effects, relaxation times, or self-diffusion coefficients. Also, NMR spectroscopy is a very powerful tool for the structural and dynamical investigations of IL systems.[1,16] For the imidazolium family of ILs, the chemical shift of the H2 proton has been recognized

to be a sensitive probe of the local environment of the imidazolium cation[50,97] because the C2-H2 bond is the most acidic bond in the imidazolium ring and thus is typically the most favorable site for hydrogen bonding.[98,99] Unfortunately, the rationalizations of experimental results such as the NMR shielding constants are necessary yet virtually unachievable by measurements due to the fast chemical exchange. Also, the capabilities of nuclear magnetic resonance for clarifying the local structure of glacial acetic acid ought to be limited because different aggregation patterns cannot be resolved in the NMR spectra due to the same problem.

Combined quantum mechanics and molecular mechanics force fields (QM/MM) have been shown to be very successful in the description of condensed phase problems in chemistry. [100–105] The success of this method is due to the fact that the QM/MM method allows for a detailed description of the interesting part of the system, whereas the solvent or surrounding medium may be described using a classical method. In this approach, the total system is divided into at least two subsystems treated at different levels of theory. The MM system is described using classical force fields as in molecular mechanics (MM), whereas the QM part is evaluated using a quantum mechanical treatment of the electrons. The QM/MM model is superior compared to other approaches designed to model condensed phase molecules. In contrary to the continuum model, the discrete nature of solvent molecules is kept intact. Methods based on QM/MM are in this respect promising since they are capable of taking the molecular details of the environment into account. Molecular dynamics (MD) is a computer simulation method for analyzing the physical movements of atoms and molecules. The atoms and molecules are allowed to interact for a fixed period of time, giving a view of the dynamic "evolution" of the system. The trajectories of atoms and molecules are determined by numerically solving Newton's equations of motion for a system of interacting particles, where forces between the particles and their potential energies are often calculated using molecular mechanics force fields. Molecular systems typically consist of a vast number of particles and it is impossible to determine the properties of such complex systems analytically. MD simulations circumvent this problem by using numerical methods. The method is applied mostly in chemical physics, materials science, and biophysics.

Only a few works are published where the hybrid MD-QM/MM approach is applied to the study of ionic liquid systems. For example, Bagno et al. investigated the dependence of ^{1}H and ^{13}C NMR chemical shifts of 1-butyl-

3-methylimidazolium-based room temperature ionic liquids on the counteranion ([BF_4], [$MeSO_4$]) using both the classical Car-Parrinello MD simulations, and QM/MM method.[106,107] Moreover, Mao et al. systematically investigated the mechanism of CO_2 capture by 1,3 di-substituted imidazolium acetate ionic liquids using density functional theory. Solvent effects were analyzed using QM/MM and QM/QM approaches with the help of MD simulations and ONIOM methods.[108] Very recently, Saielli combined classical MD simulations with quantum ONIOM calculations of NMR chemical shifts of the [C4mim][Cl] IL and its mixtures with water.[109]

The properties of the formation of ion pairs at very low concentrations of IL in polar and non-polar solvents have been studied both experimentally and theoretically.[17,45,46,48,50,110,111] However, there is still disagreement about the dynamic equilibrium between free ions, solvent-separated and contact ion pairs in traditional solvents. NMR spectroscopy is an excellent tool for studying the structure of such complex systems. However, this method is incapable of predicting structural changes due to the fast chemical exchange in the system. Nevertheless, the combined MD-QM/MM approach can rationalize the experimental results and explain the dynamic equilibrium in the system. Mixtures of ionic liquids and water have a complex dynamical equilibrium. Information about the structure of such systems is hidden and is not visible in NMR spectroscopy because NMR signals are averages of the entire system. In such cases, the NMR experiment is incapable of predicting structural changes in the system. However, the combined MD-QM/MM method may help to rationalize the experimental NMR data of IL/water mixtures. A similar situation exists in strongly-associating carboxylic acids with complex dynamical equilibrium such as glacial acetic acid. Due to the reasons mentioned above, the NMR experiment cannot fully determine the structural features of carboxylic acids because these acids tend to aggregate into different types of molecular aggregates. Moreover, it is possible to determine which aggregates are prone to form in glacial acetic acid and which of the aggregates determine the changes in the chemical shift of the acidic proton in acetic acid using the mentioned theoretical method. Therefore, the applicability and use of a combined MD-QM/MM method to rationalize experimental NMR data of molecular systems with complex dynamical equilibrium would be very welcome.

GOAL AND TASKS OF THE WORK

The main goal of this thesis is to get insight into the structural properties of heterogeneous ILs and their mixtures with molecular solvents as well as of strongly-associating carboxylic acids with complex dynamical equilibrium. To this end, an advanced MD-QM/MM computation method will be used in combination with experimental NMR measurements. The following tasks have been set:

1. Elucidate ion pairing processes in low concentration solution of the 1-decyl-3-methyl-imidazolium chloride in traditional solvents of different polarity and capabilities of hydrogen bonding.

2. Scrutinize nanostructural organization in mixtures of [C4mim][Cl] IL and water.

3. Get molecular-level insight into intermolecular structure of glacial acetic acid.

STATEMENTS OF THE THESIS

1. At low concentration of 1-decyl-3-methyl-imidazolium chloride ionic liquid in aqueous solution, complete dissociation of ion pairs into free ions takes place. Dissociation of ionic pairs does not occur of this ionic liquid in dichloromethane solution. In acetonitrile, an equilibrium is established between dissociated ions and contact ion pairs that is shifted more towards free ions.

2. In mixtures of 1-butyl-3-methyl-imidazolium chloride ionic liquid and water, there is an equilibrium between the water molecules which form hydrogen bonds with each other and the water molecules which form hydrogen bonds with chloride anions; as the molar fraction of the ionic liquid in the binary mixture increases, the equilibrium changes, the population of the first type of aggregates decreases and this results in the non-monotonic evolution of the chemical shift of water observed experimentally.

3. Cyclic dimers are not the dominant type of aggregation of acetic acid mole-cules in pure acetic acid. The experimentally observed decrease in the ^{1}H NMR chemical shift of acidic proton of acetic acid in the binary

mixture with cyclohexane with the increasing molar fraction of AA is a combined effect of the proliferation of open dimers, dimers with hydrogen bonding between hydroxyl groups, and monomeric acetic acid molecules.

SCIENTIFIC NOVELTY

In this thesis, an advanced computational procedure based on MD-QM/MM methodology is applied to model structure, dynamics, and NMR properties of complex molecular systems in the condensed-phase. The MD-QM/MM approach was for the first time applied for the analysis of the ion pairing phenomenon of [C10mim][Cl] IL in traditional molecular solvents. This study proves that [C10mim][Cl] ion pairs break into free ions in an aqueous solution, while ion pairs are not disrupted in a dichloromethane solution. In acetonitrile solvent, an equilibrium is established between contact ion pairs and free ions. The nanostructural organization in mixtures of the [C4mim][Cl] IL and water was in great detail investigated for the first time by applying the MD-QM/MM approach. It has been shown, that the non-monotonic evolution of the chemical shift of water is due to an equilibrium between water molecules which form hydrogen bonds with other water molecules and water molecules which form hydrogen bonds with chloride anions. The MD-QM/MM approach was for the first time applied for the analysis of the intermolecular structure of glacial acetic acid. The study proves that cyclic dimers are not the dominant aggregation type in glacial acetic acid and the lowering of the chemical shift of the acidic proton in neat acetic acid as compared to the corresponding proton signal of cyclic dimer in cyclohexane solution is due to rising populations of the acetic acid aggregates with hydrogen bonding between hydroxyl moieties and of monomeric acetic acid molecules with increasing molar fraction of acetic acid. The results of this thesis show that MD-QM/MM computational methodology is a promising scheme to get physical insight into the intermolecular structure and dynamics of complex materials such as IL and their mixtures with traditional solvents.

PUBLICATIONS INCLUDED IN THE THESIS

1. Lengvinaite Dovile, Kvedaraviciute Sonata, Bielskute Stase, Vytautas Klimavicius, Vytautas Balevicius, Mocci Francesca, Laaksonen Aatto,

Aidas Kestutis, Structural Features of the [C4mim][Cl] Ionic Liquid and Its Mixtures with Water: Insight from a ^{1}H NMR Experimental and QM/MD Study, *The Journal of Physical Chemistry B*, 2021, **125**, 13255–13266.

2. Lengvinaite Dovile, Vytautas Klimavicius, Vytautas Balevicius, Aidas Kestutis, Computational NMR Study of Ion Pairing of 1-Decyl-3-methylimidazolium Chloride in Molecular Solvents, *The Journal of Physical Chemistry B*, 2020, **124**, 10776–10786.

3. Lengvinaite Dovile, Aidas Kestutis, Kimtys Liudvikas, Molecular aggregation in liquid acetic acid: insight from molecular dynamics/quantum mechanics modelling of structural and NMR properties, *Physical Chemistry Chemical Physics*, 2019, **21**, 14811–14820.

OTHER PUBLICATIONS

1. Vytautas Klimavicius, Dagys Laurynas, Klimkevicius Vaidas, Lengvinaite Dovile, Aidas Kestutis, Balciunas Sergejus, Banys Juras, Chizhik Vladimir, Balevicius Vytautas, Solid-State NMR and Impedance Spectroscopy Study of Spin Dynamics in Proton-Conducting Polymers: An Application of Anisotropic Relaxing Model, *The Journal of Physical Chemistry B*, 2021, **125**, 12592–12602.

CONFERENCE ABSTRACTS

1. D. Lengvinaite, S. Grubisic, K. Aidas, I. Cvijetic, A. Laaksonen, F. Mocci, QM/MM protocol for studying interactions in ionic liquids: charges optimization, 2nd MOLIM general meeting of COST action MOLIM: molecules in motion, Dubrovnik, Croatia, 2016.

2. D. Lengvinaite, S. Grubisic, K. Aidas, I. Cvijetic, A. Laaksonen, F. Mocci, QM/MM protocol for studying interactions in ionic liquids: charges optimization, 60th Scientific Conference for Students of Physics and Natural Sciences "Open Readings 2017", Vilnius, Lithuania, 2017.

3. D. Lengvinaite, V. Klimavicius, K. Aidas, NMR spectra of imidazolium based ionic liquids: insights from large-scale QM/MD calculations,

Joint training school of the COST actions: CM1401 our astrochemical history and CM1405 MOLIM - molecules in motion, Belgrade, Serbia, 2017.

4. D. Lengvinaite, V. Klimavicius, K. Aidas, NMR spectra of imidazolium based ionic liquids: insights from large-scale QM/MD calculations, Lithuanian National Conference of Physics (LNFK–42), Vilnius, Lithuania, 2017.

5. D. Lengvinaite, K. Aidas, Molecular dynamics/quantum mechanics modeling of structural and NMR properties of acetic acid/cyclohexane binary solutions, 61st Scientific Conference for Students of Physics and Natural Sciences "Open Readings 2018", Vilnius, Lithuania, 2018.

6. D. Lengvinaite, K. Aidas, Structure and NMR properties of acetic acid/cyclohexane binary solutions studied using molecular dynamics/quantum mechanics approaches, European Congress on Molecular Spectroscopy -EUCMOS, Coimbra, Portugal, 2018.

7. D. Lengvinaite, K. Aidas, NMR spectra of water-ionic liquid mixtures: large-scale molecular dynamics and quantum mechanics/molecular mechanics modelling, HPC-Europa Transnational Access Meeting (TAM 2018), Edinburgh, Scotland, 2018.

8. D. Lengvinaite, K. Aidas, Molecular self-aggregation in glacial acetic acid: insights from molecular dynamics/quantum mechanics modelling of structural and ^{1}H NMR properties, 4th General Meeting of the CM1405 COST Action MOLIM: Molecules in Motion, Bologna, Italy, 2019.

9. D. Lengvinaite, K. Aidas, NMR spectra of water-ionic liquid mixtures: large-scale molecular dynamics and quantum mechanics/molecular mechanics modelling, 62st Scientific Conference for Students of Physics and Natural Sciences "Open Readings 2019", Vilnius, Lithuania, 2019.

10. D. Lengvinaite, V. Klimavicius, K. Aidas, Molecular aggregation in liquid acetic acid: insights from molecular dynamics/quantum mechanics modelling of structural and NMR properties, 18th International Conference on Density-Functional Theory and its Applications, Alicante, Spain, 2019.

11. D. Lengvinaite, K. Aidas, Molecular self-aggregation in glacial acetic acid: insight from molecular dynamics/quantum mechanics modelling of structural and ^{1}H NMR properties, Grand Challenges for Theoretical Chemistry, Helsingor, Denmark, 2019.

12. D. Lengvinaite, V. Klimavicius, K. Aidas, Molecular aggregation in liquid acetic acid: insights from molecular dynamics/quantum mechanics modelling of structural and NMR properties, Lithuanian National Conference of Physics (LNFK–43), Kaunas, Lithuania, 2019.

13. D. Lengvinaite, V. Klimavicius, V.Balevicius, K. Aidas, Computational NMR study of ion pairing of 1-decyl-3-methylimidazolium chloride in molecular solvents, International Symposium on Molecular Spectroscopy (ISMS), Illinois, USA, 2021.

14. D. Lengvinaite, NMR spectra of ionic liquids and its mixtures: insight from QM/MD calculations, Lithuanian National Conference of Physics (LNFK–44), Vilnius, Lithuania, 2021.

AUTHOR'S CONTRIBUTION

Author's contribution to the performed computations is 80%. Author's contribution to data analysis is 80%. Author's contribution to writing publications is 75%. The experimental NMR measurements were carried out by experimental NMR group at the Institute of Chemical Physics of Vilnius University.

CHAPTER 1
THEORETICAL OUTLINE

In this chapter, an outline of the principal aspects of the QM/MM model and classical MD simulations used in this thesis will be given. The first focus will be on the derivation of the general expression of the QM/MM Hamiltonian. This general QM/MM Hamiltonian serves to derive the effective QM/MM equations for any variational quantum chemical method. In the subsequent section, the main principles of the DFT method are provided. Finally, a review of the classical molecular dynamics will be given.

1.1. THE QM/MM HAMILTONIAN

The idea of the hybrid QM/MM model is to divide the total molecular system into at least two parts, which are treated at different levels of theory. In the QM/MM model, the region of the system where chemical processes are important, is treated at an appropriate level of quantum chemistry theory, while the other part is described by a molecular mechanics force field. The QM/MM partitioning is illustrated in Figure 1, which also contains the prescriptions of the electronic and nuclear coordinates in the QM region and the coordinates of the sites in the MM subsystem for which MM parameters are assigned. In the QM subsystem, the electrons and the nuclei are labeled separately at positions $\vec{r}_i$ and $\vec{R}_n$, respectively. In the MM subsystem, the particles are presented through effective charges positioned at the atomic sites $\vec{R}_s$. In order to model polarization interactions explicitly, molecular electronic polarizability tensors have to be considered which are attributed, for example, to the center of mass of the molecules in the classical region or alternatively distributed over the atomic sites. The polarizability tensors give rise to induced dipole moments in the MM subsystem and are labeled as $\vec{R}_a$.

In the QM/MM approach the energy of the total system is expressed ac-

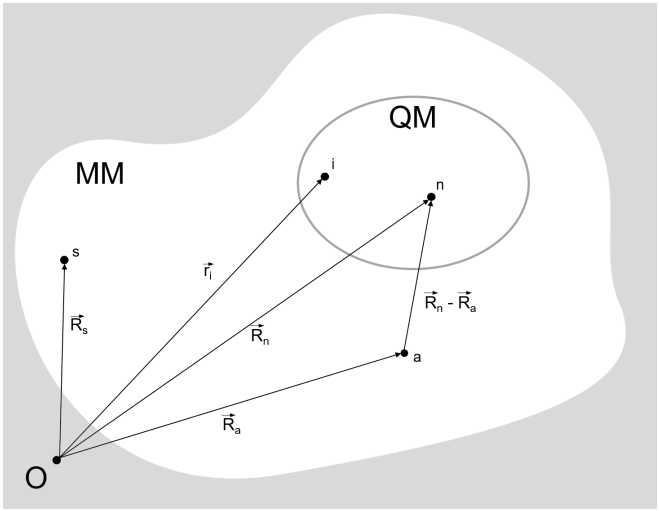

Figure 1: An illustration of the QM/MM concept. The term, $\vec{r}_i$ is a vector describing an electron in the QM part while $\vec{R}_n$ is a vector to a nucleus in the QM part. The term, $\vec{R}_a$ is a vector to an induced dipole moment in the MM part of the system and the vector $\vec{R}_s$ describes the position of an effective point charge in the MM part.

cording to[112] as

$$E = E^{QM} + E^{QM/MM} + E^{MM} \tag{1}$$

where the term E^{QM} is the usual expression of the energy of the QM subsystem. The term $E^{QM/MM}$ represents the interaction energy between the QM and MM regions and, E^{MM} describes the energy of the MM subsystem. Eq. 1 implies that the Hamiltonian of the whole system is given by

$$\hat{H} = \hat{H}^{QM} + \hat{H}^{QM/MM} + \hat{H}^{MM}, \tag{2}$$

here, $\hat{H}^{QM}$, is the many-body molecular Born-Oppenheimer Hamiltonian, in atomic units given according to[113]

$$\begin{aligned} \hat{H}^{QM} = & \sum_i \left(-\frac{1}{2}\nabla_i^2 - \sum_n \frac{Z_n}{\left|\vec{r}_i - \vec{R}_n\right|} \right) + \frac{1}{2} \sum_{i,j(i\neq j)} \frac{1}{\left|\vec{r}_i - \vec{r}_j\right|} \\ & + \frac{1}{2} \sum_{m,n(m\neq n)} \frac{Z_m Z_n}{\left|\vec{R}_m - \vec{R}_n\right|} \end{aligned} \tag{3}$$

where $\vec{r}_i$ and $\vec{R}_n$ are the position vectors of the i'th electron and the n'th nucleus, respectively, and Z_n is the nuclear charge of the n'th nucleus. The Laplacian operator, ∇_i^2, involves differentiation with respect to the coordinates of the

i'th electron. The first term in eq. 3 represents the kinetic energy of the electrons, while the second term describes the interactions between the electrons and the nuclei. The third and fourth terms represent the electron-electron and the nuclear-nuclear repulsion energy, respectively.

The QM/MM interaction Hamiltonian, $\hat{H}^{QM/MM}$, is expressed in the mean-field description[114] as

$$\hat{H}^{QM/MM} = \hat{H}^{el} + \hat{H}^{pol} + \hat{H}^{vdw}. \tag{4}$$

The first term represents the electrostatic interactions between the partial atomic charges in the MM system and electrons as well as nuclei in the QM part. The term, $\hat{H}^{pol}$, is an effective Hamiltonian which accounts for the explicit mutual polarization between the QM and MM parts. The last term, $\hat{H}^{vdw}$, models the van der Waals interactions between the two regions. The electrostatic interaction Hamiltonian can thus be expressed as

$$\hat{H}^{el} = -\sum_{s=1}^{S} \hat{N}_s + E_{S,N}^{el,nuc}, \tag{5}$$

here the first term describes the interaction between the electrons of the QM region and the partial atomic charges in the MM part. The electronic contribution is written in terms of

$$\hat{N}_s = \sum_{pq} \left\langle \phi_p \left| \frac{q_s}{\left|\vec{R}_s - \vec{r}_i\right|} \right| \phi_q \right\rangle \hat{E}_{pq} = \sum_{pq} n_{pq}^{s} \hat{E}_{pq}. \tag{6}$$

The set, $\left|\phi_q\right\rangle$, represents the molecular orbitals. The quantity, $\hat{E}_{pq}$, is a one-electron excitation operator written in terms of creation, $\hat{a}_{p\sigma}^{\dagger}$, and annihilation, $\hat{a}_{p\sigma}$ operators

$$\hat{E}_{pq} = \sum_{\sigma} \hat{a}_{p\sigma}^{\dagger} \hat{a}_{p\sigma} \tag{7}$$

where, σ, refers to spin projection. The second term of eq. 5 expresses the electrostatic energy due to the interaction of nuclei of the QM region and the partial charges in the MM region and is written as

$$E_{S,N}^{el,nuc} = \sum_{s=1}^{S} \sum_{n=1}^{N} \frac{q_s Z_n}{\left|\vec{R}_s - \vec{R}_n\right|}. \tag{8}$$

The index s in both equations runs over all of the sites in the MM system. These sites are usually located at the MM atoms while q_s is the charge at the site s.

In some cases, for the calculation of molecular properties it is important to include polarization effects in the interaction between the QM and MM subsystems. If the MM subsystem does not contain polarizable centers, the QM subsystem is polarized by partial point charges in the classical part. This polarization is static. However, when polarizable centers are present in the MM subsystem, the MM part responds to changes in the QM part, implying that it is necessary to account for the polarization properly. The mutual polarization between QM and MM regions which is achieved by introducing dipole polarizability tensors assigned to the molecular system in the MM region will be discussed. The polarization interactions are represented by the polarization Hamiltonian, $\hat{H}^{pol}$, in the general expression for the QM/MM Hamiltonian in eq. 4. The energy contributions due to the induced dipole moments are not completely straightforward. The part of the interaction energy (between all molecules in the system) which depends directly on the induced dipole moments, $\vec{\mu}_a^{ind}$, is given as

$$\begin{aligned} E\left[\vec{\mu}_a^{ind}\right] = &-\sum_{a=1}^{A} \vec{\mu}_a^{ind}\left(\vec{E}^{el}\left(\vec{R}_a\right) + \vec{E}^{n}\left(\vec{R}_a\right) + \vec{E}^{s}\left(\vec{R}_a\right)\right) \\ &-\frac{1}{2}\sum_{a}^{A}\sum_{a'\neq a}^{A} \vec{\mu}_a^{ind}\mathbf{T}_{aa'}\vec{\mu}_{a'}^{ind} \end{aligned} \tag{9}$$

Here, $\vec{\mu}_a^{ind}$, is the induced dipole moment due to ath polarizability at site $\vec{R}_a$. $\vec{E}^{el}\left(\vec{R}_a\right)$, $\vec{E}^{n}\left(\vec{R}_a\right)$ and $\vec{E}^{s}\left(\vec{R}_a\right)$ are the electric field strengths at site $\vec{R}_a$ due to, respectively, electrons and nuclei in the QM subsystem and charges in the MM subsystem. The, $\mathbf{T}_{aa'}$, is the dipole interaction tensor. The summation is over all the polarizable sites in the first term and over all pairs of the polarizable sites in the second term on the right hand side of eq. 9, where the factor of 1/2 is introduced due to the double counting. In eq. 9, the electric field due to the electrons in the QM subsystem at site $\vec{R}_a$ is given as an expectation value, $\vec{E}^{el}\left(\vec{R}_a\right)$. The vector, $\vec{E}^{n}\left(\vec{R}_a\right)$, is the electric field due to the QM nuclei. Here, $\vec{E}^{s}\left(\vec{R}_a\right)$, represents the electric field at the center-of-mass a of the MM molecule due to the partial charges. The, $\mathbf{T}_{aa'}$, is the dipole interaction tensor is given as

$$\mathbf{T}_{aa'} = \frac{1}{\left|\vec{R}_a - \vec{R}_{a'}\right|^3}\left[\frac{3\left(\vec{R}_a - \vec{R}_{a'}\right)\left(\vec{R}_a - \vec{R}_{a'}\right)^T}{\left|\vec{R}_a - \vec{R}_{a'}\right|^2} - \mathbf{1}\right], \tag{10}$$

and the index a refers to polarizable site.

The vector, $\vec{\mu}_a^{ind}$, is the dipole moment at the center-of-mass a of each MM molecule. In a linear approximation, the induced dipole moment is related to the total electric field, $\vec{E}_a^{total}$.

$$\vec{\mu}_a^{ind} = \boldsymbol{\alpha}_a \vec{E}_a^{total} \tag{11}$$

where, $\boldsymbol{\alpha}_a$, is the polarizability tensor at the center-of-mass of each MM molecule. The total electric field has four contributions

$$\vec{E}_a^{total} = \vec{E}^{el}\left(\vec{R}_a\right) + \vec{E}^{n}\left(\vec{R}_a\right) + \vec{E}^{s}\left(\vec{R}_a\right) + \vec{E}^{ind}\left(\vec{R}_a\right) \tag{12}$$

where the last term represents the electric field due to the other induced dipole moments.

To obtain the correct expression for the polarization Hamiltonian, there is also a self energy, E^{self}, which is used to create the induced dipole moments.[115] Using the relation between the total electric field and the induced dipole moment in eq. 11, the self energy can be expressed as follows

$$\begin{aligned} E_{self} = &\frac{1}{2}\sum_{a=1}^{A} \vec{\mu}_a^{ind}\left(\vec{E}^{s}\left(\vec{R}_a\right) + \vec{E}^{el}\left(\vec{R}_a\right) + \vec{E}^{n}\left(\vec{R}_a\right)\right) \\ &+ \frac{1}{2}\sum_{a,a'(a\neq a')}^{A} \vec{\mu}_a^{ind}\mathbf{T}_{aa'}\vec{\mu}_{a'}^{ind}. \end{aligned} \tag{13}$$

An addition of the energy contributions in eq. 9 and eq. 13 gives

$$\begin{aligned} E\left[\vec{\mu}_a^{ind}\right] + E_{self} = &-\frac{1}{2}\sum_{a=1}^{A} \vec{\mu}_a^{ind}\left(\vec{E}^{el}\left(\vec{R}_a\right) + \vec{E}^{n}\left(\vec{R}_a\right)\right) \\ &-\frac{1}{2}\sum_{a=1}^{A} \vec{\mu}_a^{ind}\vec{E}^{s}\left(\vec{R}_a\right). \end{aligned} \tag{14}$$

The first term in eq. 14 is here referred to as the polarization energy for the QM "solute" in the solvent due to the MM polarizabilities. For the QM part of the system, it can be described in terms of the corresponding effective operator

$$\hat{H}^{pol} = -\frac{1}{2}\sum_{a=1}^{A} \vec{\mu}_a^{ind} \cdot \left(\vec{E}^{el}\left(\vec{R}_a\right) + \vec{E}^{n}\left(\vec{R}_a\right)\right) \tag{15}$$

where the dependency of the vector of the induced dipole moments, $\vec{\mu}_a^{ind}$, and therefore also the polarization operator, $\hat{H}^{pol}$, on the electronic wave function through the electronic field is to be remembered. The second term in eq. 14

only involves particles and induced moments both situated in the MM system. Correspondingly, this last term is included in the MM interaction energy. However, this term is explicitly accounted for in the optimization condition of the QM wave function.

The third term in the Hamiltonian in eq. 4, is the van deer Waals term, $\hat{H}^{vdw}$. This term accounts for all non-electrostatic interactions like dispersion and short-range exchange repulsion. These interactions are short-range and they are usually modeled by the 6-12 type Lennard-Jones potential,

$$\hat{H}^{vdw} = \sum_{a=1}^{A} \sum_{n:center} \left[\frac{A_{na}}{\left|\vec{R}_n - \vec{R}_a\right|^{12}} - \frac{B_{na}}{\left|\vec{R}_n - \vec{R}_a\right|^{6}} \right]. \tag{16}$$

In eq. 16 the index *a(n)* refers to the center-of-mass of each MM(QM) molecule. These sums may easily be extended to summations over sites in the MM and QM molecules. However, usually, when describing solvation processes the quantum system only consists of one QM molecule and in this case, the sum over *n* drops out of eq. 16. This term does not include any electronic coordinates and thereby it is a simple constant, which does not have an influence on any molecular properties, which are not described as derivatives of the energy with respect to molecular geometry.

In eq. 15 the vector of the induced dipole moment, $\vec{\mu}_a^{ind}$, is expressed as

$$\vec{\mu}_a^{ind} = \alpha_a \left(\vec{E}_a^{el} + \vec{E}_a^{n} + \vec{E}_a^{s} + \vec{E}_a^{ind} \right), \tag{17}$$

Now, the polarization Hamiltonian can be rewritten to read

$$\hat{H}^{pol} = -\frac{1}{2} \sum_{a=1}^{A} \vec{E}_a^{el} \alpha_a \left(\vec{E}_a^{el} + \vec{O}_a^{ns} \right) + O_{ind}^{ns}, \tag{18}$$

where the vector, $\vec{O}_a^{ns}$, and the energy term, O_{ind}^{ns}, are defined according to

$$\vec{O}_a^{ns} = 2\vec{E}_a^{n} + \vec{E}_a^{s} + \vec{E}_a^{ind} \tag{19}$$

and

$$O_{ind}^{ns} = -\frac{1}{2} \sum_{a=1}^{A} \vec{E}_a^{n} \alpha_a \left(\vec{E}_a^{n} + \vec{E}_a^{s} + \vec{E}_a^{ind} \right) \tag{20}$$

By taking the expectation value of eq. 4 and making use of eq. 11, the

following expression for the total interaction energy is obtained

$$\begin{aligned} E_{QM/MM} &= E^{el} + E^{vdw} + E^{pol} \\ &= -\sum_{s=1}^{S} \hat{N}_s + E_{S,N}^{el,nuc} + E^{vdw} \\ &- \frac{1}{2}\sum_{a=1}^{A} \vec{E}_a^{el}\alpha_a \left(\vec{E}_a^{el} + \vec{O}_a^{ns}\right) + O_{ind}^{ns}. \end{aligned} \tag{21}$$

and the coupling Hamiltonian, $\hat{H}_{QM/MM}$, can be expressed as

$$\hat{H}_{QM/MM} = -\sum_{s=1}^{S} \hat{N}_s + E_{S,N}^{el,nuc} + E^{vdw} - \frac{1}{2}\sum_{a=1}^{A} \vec{\mu}_a^{ind}\left(\vec{E}_a^{el} + \vec{E}_a^{n}\right) \tag{22}$$

The classical part of the total Hamiltonian in eq. 2, $\hat{H}_{MM}$, is decomposed into a intramolecular and intermolecular contribution.

$$\hat{H}_{MM} = \hat{H}_{MM}^{intra} + \hat{H}_{MM}^{inter} \tag{23}$$

The, $\hat{H}_{MM}^{intra}$, includes all traditional molecular mechanical potential terms related to stretching, bending and torsional motions. The, $\hat{H}_{MM}^{inter}$, is written according to

$$\hat{H}_{MM}^{inter} = \frac{1}{2}\sum_{s\neq s'}^{S} \frac{q_s q_{s'}}{\left|\vec{R}_s - \vec{R}_{s'}\right|} - \frac{1}{2}\sum_{a=1}^{A} \vec{\mu}_a^{ind}\vec{E}^s\left(\vec{R}_a\right) + E_{MM}^{vdw} \tag{24}$$

where the term, E_{MM}^{vdw}, is the van der Waals MM energy. The second term on the right hand side of eq. 24 comes from eq. 14. The interaction term between partial point charges and induced dipole moments is scaled by a factor of 2. Also, the classical Hamiltonian implicitly depends on the wavefunction through induced dipole moments.

1.2 THE DFT METHOD

Density functional theory (DFT) is a very powerful and relatively cost-effective quantum-mechanics tool for the calculation of energies and other properties of molecules.[116] DFT theory is based on a theorem due to Hohenberg and Kohn,[117] which states that a knowledge of the electron density of a system in its ground state is enough to determine the energy. In other words, the energy is a function of the density. The molecular ground state energy is the functional of the ground state electron density.[118]

$$E[\rho] = T[\rho] + V_{Ne}[\rho] + J[\rho] + E_{ee}[\rho] + h_{nuc} \tag{25}$$

In this expression, $T[\rho]$ is the kinetic energy associated with the given electron density. The term $V_{Ne}[\rho]$ accounts for the interactions of the electronic density with the external potential and usually corresponds to the electron-nuclear attraction energy. The term, $J[\rho]$, is the classical self-repulsion energy of the electronic density distribution. The term, $E_{ee}[\rho]$ is the electron-electron interaction energy. The last term, h_{nuc} is the energy of the internuclear repulsion. The problem is that the exact forms of the kinetic energy, $T[\rho]$, and non-classical electron-electron interaction energy, $E_{ee}[\rho]$, are not known.

Here, the starting point is a determinantal wavefunction for N *non-interacting* electrons in N orbitals φ_i. The electronic density is then expressed in terms of the Kohn-Sham orbitals according to

$$\rho(\vec{r}) = \sum_{i=1}^{N} |\varphi_i(\vec{r})|^2, \tag{26}$$

and the approximation of the kinetic energy functional is

$$T_s[\rho] = -\frac{1}{2}\sum_{i=1}^{N} \langle \varphi_i(\vec{r})| \nabla^2 |\varphi_i(\vec{r})\rangle . \tag{27}$$

Using the later approximation of the kinetic energy functional, the energy functional in eq. 25 now takes a form

$$E[\rho] = T_s[\rho] + V_{Ne}[\rho] + J[\rho] + E_{xc}[\rho] + h_{nuc}, \tag{28}$$

where $E_{xc}[\rho]$ is the exchange-correlation functional contains not only the functional $E_{ee}[\rho]$ but also residual error due to the approximate treatment of the kinetic energy *via* eq. 27. For eq. 27 to be valid, the Kohn-Sham orbitals have to be orthonormal. $E_{xc}[\rho]$ is defined as

$$E_{xc}[\rho] = T[\rho] - T_s[\rho] + E_{ee}[\rho] - J[\rho] . \tag{29}$$

The orbitals φ_i satisfy the Kohn-Sham equations:

$$\hat{h}^{KS}\varphi_i = \epsilon_i \varphi_i. \tag{30}$$

The Kohn-Sham operator is

$$\hat{h}^{KS} = -\frac{1}{2}\nabla^2 + v_{Ne}(\vec{r}) + j(\vec{r}) + v_{xc}(\vec{r}) . \tag{31}$$

The term, $v_{xc}(\vec{r})$ is the exchange-correlation potential, which is the functional derivative of $E_{xc}[\rho]$:

$$v_{xc}(\vec{r}) = \frac{\delta E_{xc}[\rho]}{\delta \rho(\vec{r})}. \tag{32}$$

Therefore, just like the Hartree-Fock equations, the Kohn-Sham one-electron equations also have to be solved iteratively. The exchange-correlation functional $v_{xc}(\vec{r})$ in DFT calculations is not known exactly, therefore approximations of the functional have to be used. DFT results firmly depend on the choice of functionality, so different functionalities are applied in different models. Two classes of functionalities are commonly used in molecular calculations which are gradient-corrected (e.g. BLYP) and hybrid (e.g. B3LYP) functionals. Gradient-corrected functionals are based on the local density approximation incorporating gradient of an electron density. Hybrid functionals also have gradient–corrections, but an empirically adapted exact HF substitution is additionally taken into account. Calculations using both gradient–corrected and hybrid functionals give sufficiently good results.

1.3 NUCLEAR MAGNETIC SHIELDING TENSORS

The nuclear magnetic shielding tensor σ^N for nucleus N is defined as the second–order response of the electronic energy to an external magnetic induction $\vec{B}$ and a nuclear magnetic moment $\vec{m}_N$. In the atomic orbital basis, the expression becomes[119,120]

$$\begin{aligned}\sigma_{ij}^N &= 1 + \left[\frac{d^2E}{dB_i dm_{N_j}}\right]_{B=m_{N_j}=0} \\ &= 1 + \sum_{\mu\nu} D_{\mu\nu}\frac{\partial^2 h_{\mu\nu}}{\partial B_i \partial m_{N_j}} + \sum_{\mu\nu}\frac{\partial D_{\mu\nu}}{\partial B_i}\frac{\partial h_{\mu\nu}}{\partial m_{N_j}},\end{aligned} \tag{33}$$

where $D_{\mu\nu}$ is an element of the density matrix in the atomic orbital basis and $h_{\mu\nu}$ is a matrix element of the effective one-electron Hamiltonian. The second term in eq. 33 is paramagnetic contribution which can be determined by solving a set of DFT/MM response equations for the three components of the magnetic induction. [121,122] In order to ensure origin-independent results for the nuclear magnetic shielding constants, the gauge-including atomic orbitals (GIAOs) are employed, that is, the atomic orbitals basis functions depend explicitly on the magnetic induction through

$$X_\mu\left(\vec{B}\right) = \exp\left[(-i/2)\left(\vec{B}\times\vec{R}_\mu\right)\cdot\vec{r}\right] X_\mu(0), \tag{34}$$

where $\vec{R}_\mu$ is the vector giving the position of the nucleus to which the field-dependent basis function is attached relative to the global gauge origin, and

$X_\mu(0)$ indicates a conventional atomic orbitals basis function not depending on $\vec{B}$.

Equation 33 applies both to the case of a molecule in vacuum and in solution or an environment. The (polarizable) environment makes contributions both through the density matrix, which is obtained self-consistently including the perturbation from the surroundings, and through the derivative of the density matrix with respect to the magnetic induction, i.e., both terms in eq. 33 contain the effect of the environment.

The first derivative of the density matrix with respect to the magnetic induction is obtained by solving the coupled-perturbed Kohn-Sham equations to which the first derivative of the effective Kohn-Sham operator with respect to the magnetic induction contributes. This method represents a convenient and flexible scheme for the calculation of nuclear magnetic shielding tensors of molecules coupled to a discrete medium in which environmental polarization effects are treated in a self-consistent way.[123]

1.4 MOLECULAR DYNAMICS METHOD

Molecular dynamics simulation is a technique for computing the statistical, structural, and dynamical properties of classical many-body systems. The principle of the classical molecular dynamics simulation is the classical Newton's equations of motion solution for many-body systems. Molecular dynamics simulations are widely used in chemical physics, material science, and modeling of various biomolecules. In the classical mechanics approach to MD simulations, molecules are treated as classical objects, resembling the 'ball and spring' model. Therefore, the classical MD simulations are often used to perform simulations of large systems and allow simulating systems containing 10^1-10^5 number of atoms in microseconds timescale.

MD simulations are conducted in accordance with clearly defined steps. Each molecular simulation starts from the initial conditions of the system, such as temperature, density, number of particles, the simulation duration, molecular structural parameters, etc. At each step, the forces on the atoms are computed and combined with the current positions and velocities to generate new positions and velocities a short time ahead. The force acting on each atom is assumed to be constant during the time interval. The atoms are then moved to the new positions, an updated set of forces is computed, and so on. In this way, a molecular dynamics simulation generates a trajectory that describes how the dynamic variables change with time.

1.4.1 Integration the equations of motion

MD simulation is a technique to produce a dynamical trajectory for a system composed of N particles by integrating Newton's equations of motion. Unfortunately, such a system is described by N coupled second order nonlinear differential equations that cannot be solved exactly and has to be solved numerically step by step using an appropriate integration algorithm.

There are many algorithms for integrating the equations of motion using finite difference methods, several of which are commonly used in molecular dynamics calculations. All algorithms assume that the positions and dynamic properties (velocities, accelerations, etc.) can be approximated as Taylor series expansions of the coordinate of a particle around time t_0:

$$\vec{r}_i\left(t_0+\Delta t\right)=\vec{r}_i\left(t_0\right)+\Delta t\vec{v}_i\left(t_0\right)+\frac{1}{2}\Delta t^2\vec{a}_i\left(t_0\right)+O\left(\Delta t^3\right) \tag{35}$$

where $\vec{r}_i$ is the position of particle i, $\vec{v}_i$ is the velocity (the first derivative of the

positions with respect to time), $\vec{a}_i$ is the acceleration (the second derivative of the positions with respect to time), and so on. The Verlet algorithm[124] is probably the most widely used method for integrating the equations of motion in a molecular dynamics simulation. The Verlet algorithm uses the positions and accelerations at time $\vec{t}_0$, and the positions from the previous step, $\vec{r}_i\left(t_0 - \Delta t\right)$, to calculate the new positions at $t_0 + \Delta t$, $\vec{r}_i\left(t_0 + \Delta t\right)$. Adding the Taylor expansions for $+\Delta t$ and $-\Delta t$, the terms in Δt, Δt^3, etc. cancel and gives

$$\vec{r}_i\left(t_0 + \Delta t\right) = -\vec{r}_i\left(t_0 - \Delta t\right) + 2\vec{r}_i\left(t_0\right) + \vec{a}_i\left(t_0\right)\Delta t^2. \tag{36}$$

The velocities do not explicitly appear in the Verlet integration algorithm. The velocities can be calculated in a variety of ways; a simple approach is to divide the difference in positions at times $t_0 + \Delta t$ and $t_0 - \Delta t$ by $2\Delta t$:

$$\vec{v}_i\left(t_0\right) = \frac{1}{2\Delta t}\left[\vec{r}_i\left(t_0 + \Delta t\right) - \vec{r}_i\left(t_0 - \Delta t\right)\right]. \tag{37}$$

Several variations of the Verlet algorithm have been developed. One of the frequently used Verlet algorithm is the so-called Leap Frog algorithm.[125] This algorithm evaluates the velocities at half-integer time steps and uses these velocities to compute the new positions. To derive the Leap Frog algorithm from the Verlet scheme is necessary to start by defining the velocities at half-integer time steps as follows

$$\vec{v}_i\left(t_0 - \frac{\Delta t}{2}\right) = \frac{\vec{r}_i\left(t_0\right) - \vec{r}_i\left(t_0 + \Delta t\right)}{\Delta t} \tag{38}$$

and

$$\vec{v}_i\left(t_0 + \frac{\Delta t}{2}\right) = \frac{\vec{r}_i\left(t_0 + \Delta t\right) - \vec{r}_i\left(t_0\right)}{\Delta t}. \tag{39}$$

New positions are computed from the current positions according eq. 38

$$\vec{r}_i\left(t_0 + \Delta t\right) = \vec{r}_i\left(t_0\right) + \vec{v}_i\left(t_0 - \frac{\Delta t}{2}\right)\Delta t. \tag{40}$$

The velocities at time $t_0 + \Delta t$ are determined using:

$$\vec{v}_i\left(t_0 + \frac{\Delta t}{2}\right) = \vec{v}_i\left(t_0 - \frac{\Delta t}{2}\right) + \vec{a}_i\left(t_0\right)\Delta t. \tag{41}$$

As the Leap Frog algorithm is derived from the Verlet scheme, it gives rise to identical trajectories. The Leap Frog method has two advantages over the standard Verlet algorithm: it explicitly includes the velocity and also does not

require the calculation of the differences of large numbers. However, it has the obvious disadvantage that the velocities are not defined at the same time as positions. As a consequence, kinetic and potential energy are also not defined at the same time, and hence the total energy cannot be directly computed in the Leap Frog scheme.

The velocity Verlet is also a commonly used algorithm and similar to the Leap Frog algorithm. The velocity Verlet[126] gives positions, velocities, and accelerations at the same time and does not compromise precision:

$$\vec{r}_i\left(t_0+\Delta t\right)=\vec{r}_i\left(t_0\right)+\vec{v}_i\left(t_0\right)\Delta t+\frac{1}{2}\Delta t^2\vec{a}_i\left(t_0\right) \tag{42}$$

$$\vec{v}_i\left(t_0+\Delta t\right)=\vec{v}_i\left(t_0\right)+\frac{1}{2}\left(\vec{a}_i\left(t_0\right)+\vec{a}_i\left(t_0+\Delta t\right)\right)\Delta t. \tag{43}$$

The velocity Verlet method is actually implemented as a three-stage procedure because, as can be seen from equation 43, to calculate the new velocities required the accelerations at both t_0 and $t_0+\Delta t$. Thus in the first step the positions at $t_0+\Delta t$ are calculated according to Equation 42 using the velocities and the accelerations at time t_0. The velocities at time $t_0+\frac{1}{2}\Delta t$ are then determined using:

$$\vec{v}_i\left(t_0+\frac{1}{2}\Delta t\right)=\vec{v}_i\left(t_0\right)+\frac{1}{2}\vec{a}_i\left(t_0\right)\Delta t. \tag{44}$$

New forces are next computed from the current positions, thus giving $\vec{a}_i\left(t_0+\Delta t\right)$. In the final step, the velocities at time $t_0+\Delta t$ are determined using:

$$\vec{v}_i\left(t_0+\Delta t\right)=\vec{v}_i\left(t_0+\frac{1}{2}\Delta t\right)+\frac{1}{2}\vec{a}_i\left(t_0+\Delta t\right)\Delta t. \tag{45}$$

The advantage of the velocity Verlet algorithm is that it requires less computer memory because only one set of positions, forces, and velocities needs to be carried at any one time. This convenience is not apparent in the original equations.

1.4.2 Force field

The accuracy of molecular dynamics simulations to predict parameters of various systems depends on the force field model. A force field is a mathematical expression describing the dependence of the energy of a system on the

coordinates of its particles. The parameters are typically obtained either from ab-initio or semi-empirical quantum mechanical calculations or by fitting to experimental data such as neutron, X–ray and electron diffraction, NMR, infrared, Raman and neutron spectroscopy, etc.[127] The most widely used force field, such as CHARMM,[128] AMBER,[129] GROMOS,[130] OPLS,[131] and COMPASS[132] are adapted for large and complex systems. The force fields can be non-polarizable and polarizable. In some cases, polarizable force fields can improve the accuracy of the simulation and provide more accurate information about the microscopic and thermodynamic properties of the system. However, the polarizable force field sharply increases the computational cost as well.

Many of the molecular modeling force fields in use today for molecular systems can be interpreted as a picture of the intra- and inter- molecular forces within the system. A typical expression for force field may look like this:

$$\begin{aligned} U(\vec{r}) = & \sum_{bonds} \frac{1}{2} k_b (r - r_0)^2 + \sum_{angles} \frac{1}{2} k_a (\theta - \theta_0)^2 \\ & + \sum_{torsions} \frac{V_n}{2} [1 + cos(n\phi - \delta)] + \sum_{LJ, i<j} 4\epsilon_{ij} \left(\frac{\sigma_{ij}^{12}}{r_{ij}^{12}} - \frac{\sigma_{ij}^{6}}{r_{ij}^{6}} \right) \\ & + \sum_{elec, i<j} \frac{q_i q_j}{r_{ij}}, \end{aligned} \tag{46}$$

where U denotes the potential energy, which is a function of the positions $(\vec{r})$ of N particles (usually atoms). The first three terms on the right side refer to intramolecular or local contributions to the total energy (bond stretching, angle bending, dihedral torsion), and the last two terms serve to describe the non-bonded interactions, including Van der Waals and the Coulombic interactions.

The various contributions are schematically represented in Figure 2. The first term in eq. 46 is the interaction between pairs of bonded atoms, modelled here by a harmonic potential that gives the increase in energy as the bond length r deviates from the reference value r_0. The second term in eq. 46 is a summation over all valence angles in the molecule, again modelled using a harmonic potential where a valence angle is an angle formed between three atoms A–B–C in which A and C are both bonded to B. The third term in eq. 46 is the dihedral or torsional term, which is included to any molecule containing more than four atoms in a row. While bond stretching and angle bending are high frequency motions that often are not relevant for the study of the properties of interest and can be replaced by a rigid approximation, torsional motions are typically hundreds of times less stiff than bond stretching

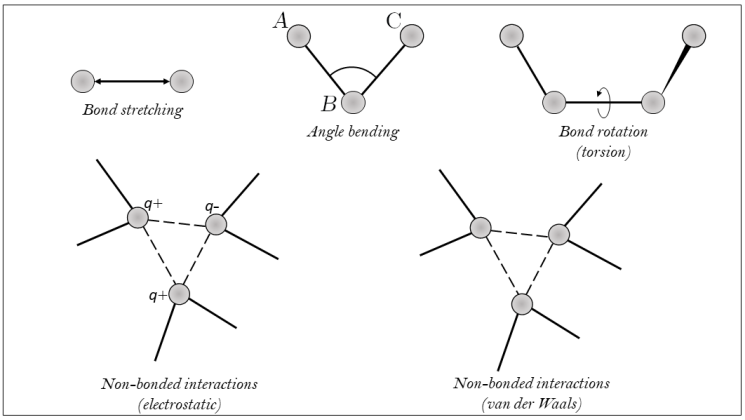

Figure 2: Schematic representation of the key contributions to a molecular mechanics force field: bond stretching, angle bending and torsional terms and non-bonded interactions.

motions and they are necessary to ensure the correct degree of rigidity of the molecule and to reproduce the major conformational changes due to rotations about bonds. Torsional energy is usually represented by a cosine function in eq. 46, where ϕ is the torsional angle, δ is the phase, n defines the number of minima or maxima between 0 and 2π, and V_n determines the height of the potential barrier.

The last two terms are the non-bonded terms, which are calculated between all pairs of atoms (i and j) that are in different molecules or that are in the same molecule but separated by at least three bonds. In a force field the non-bonded term is usually modelled using a Coulomb potential term for electrostatic interactions and a Lennard-Jones potential for the van der Waals interactions. Van der Waals interactions between two atoms arise from the balance between repulsive and attractive forces. Repulsion is due to the overlap of the electron clouds of both atoms, while the interactions between induced dipoles result in an attractive component that varies as r^{-6}. The Lennard-Jones 12-6 function is the most commonly used of the van der Waals potential, which takes the following form for the interaction between two atoms:

$$LJ = 4\epsilon \left[\left(\frac{\sigma}{r} \right)^{12} - \left(\frac{\sigma}{r} \right)^{6} \right] \tag{47}$$

The 12-6 Lennard-Jones potential contains just two adjustable parameters: the collision diameter σ (the separation for which the energy is zero) and the well

depth ϵ. These parameters are graphically illustrated in Figure 3. The Lennard-Jones potential is characterized by an attractive part that varies as r^{-6} and a repulsive part that varies as r^{-12}.

Van der Waals forces act between any pair of atoms belonging to different molecules, but they also intervene between atoms belonging to the same molecule that are sufficiently separated. It is possible to define a set of parameters (e.g. σ_{ij} and ϵ_{ij}) for each different pair of atoms, but for convenience, most force fields give individual atomic parameters (e.g. σ_i and ϵ_i), together with some rules to combine them. The determination of van der Waals parameters can be a difficult and time-consuming process and so it is common to assume that parameters for the cross interactions can be obtained from the parameters of the pure atoms using mixing rules. In the commonly used Lorentz-Berthelot mixing rules, the collision diameter σ_{ij} for the i-j interaction equals the arithmetic mean of the values for the two pure species, and the well depth ϵ_{ij} is given as the geometric mean:

$$\sigma_{ij} = \frac{1}{2}\left(\sigma_i + \sigma_j\right) \tag{48}$$

$$\epsilon_{ij} = \left(\epsilon_i \epsilon_j\right)^{\frac{1}{2}} \tag{49}$$

The final term in eq. 46 describes the electrostatic interactions. While the molecular electronic density can be obtained with a high accuracy by means of high-level quantum-mechanical calculations, the problem of reducing such density to a manageable description to be used in MD simulation is not trivial. The usual choice is to assign a partial atomic charge to each nucleus and use Coulomb's law to compute their contribution to the total energy. The partial charges can be derived from a fit to experimental thermodynamic data, but this approach is only practical for small molecules.[133] The most common way to obtain reliable partial charges consists of performing an *ab initio* calculation and deriving them from the quantum mechanical potential. Unfortunately, they cannot be derived unambiguously because atomic charges are not experimental observables, so many different methods have been developed to determine them and they do not always produce the same distribution of partial charges.[134,135] An important point to note is that in condensed phases there are polarization effects that cannot be fully described using fixed partial charges. Another point to note is that electrostatic interactions are long-ranged, so they require a particular treatment when truncating them in computation of

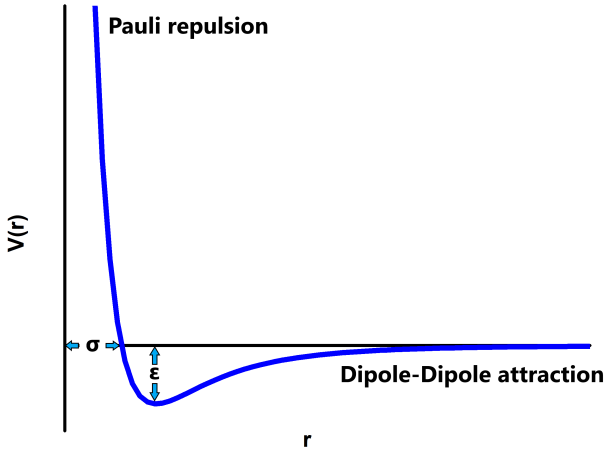

Figure 3: The Lennard–Jones potential.

the forces. A final remark is that for computational efficiency and practical reasons, partial charges are normally assigned only to atomic sites.

In most cases, both the van der Waals and electrostatic intramolecular interactions between atoms separated by more than three bonds are treated in the same way as if they were intermolecular, while interactions between 1-2 and 1-3 pairs are excluded. This is to avoid numerical problems, as the potential can become strongly repulsive or attractive due to the small distances involved, and also because the interactions between those atoms are considered to be already correctly described by the intramolecular terms.

1.4.3 Boundary conditions

Periodic boundary conditions enable a simulation to be performed using a relatively small number of particles in such a way that the particles experience forces as if they were in bulk fluid. The volume containing the N particles is treated as the primitive cell of infinite periodic lattice of identical cells as shown in Figure 4a. Periodic boundaries are widely used in computer simulations and prove to be a surprisingly effective method for simulating homogeneous bulk systems. One should always be aware that the use of such boundary conditions may lead to spurious correlations not present in a truly macroscopic bulk system. In particular, one consequence of the periodicity of

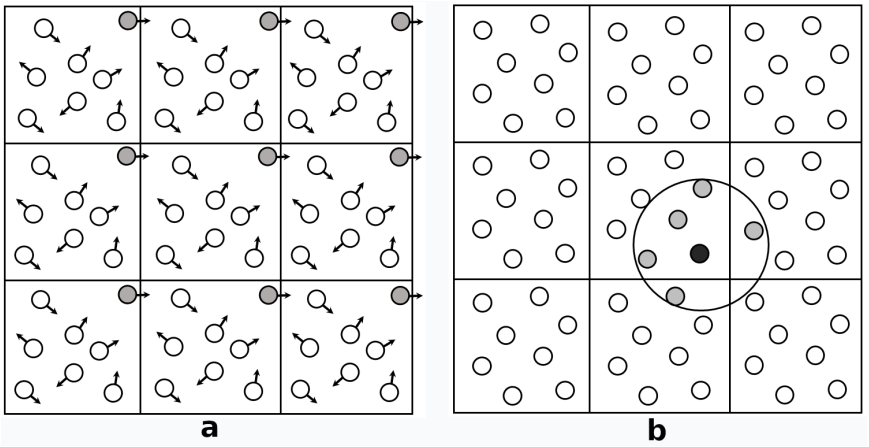

Figure 4: Two dimensional periodic boundary conditions (a) and the spherical cutoff and minimum image convention (b).

the model system is that only those fluctuations are allowed that have a wavelength compatible with the periodic lattice. The longest wavelength that still fits in the periodic box is the one for which $\lambda = L$, where L is the length of the simulation box. For longer-range electrostatic interactions the situation is more difficult and it is often necessary to accept that some long-range order will be imposed upon the system. The effects of imposing a periodic boundary can be evaluated empirically by comparing the results of simulations performed using a variety of cell shapes and size. The most time-consuming part of a molecular dynamics simulation is the calculation of the non-bonded energies or forces. The numbers of bond-stretching, angle-bending and torsional terms in a force field model are all proportional to the number of atoms but the number of non-bonded terms that need to be evaluated increases as the square of the number of atoms and is thus of order N^2. The non-bonded interactions are calculated between every pair of atoms in the system. However, for many interaction models this is not justified. If the interatomic potential has decayed to negligible value for distances much smaller than $L/2$, there is no need to compute all the interactions. The most popular way to deal with the non-bonded interactions is to use a non-bonded cutoff and apply the minimum image convention. In the minimum image convention model, each atom 'sees' at most just one image of every other atom in the system. The energy or force is calculated with the closest atom or image, see Figure 4b. When a cutoff is employed, the interactions between all pairs of atoms than are further apart that the cutoff value is set to zero, taking into account the closest image. When

periodic boundary conditions are being used, the cutoff should be no greater than half the length of the shortest side. There is no ideal truncation method, but the differences between them are less significant for larger cutoff radii, so R_c should be sufficiently large.[136] It must also be noted that this truncation should be applied only to short-ranged interactions. Long-range electrostatic interactions should never be truncated.

1.4.4 Statistical ensembles

The molecular dynamics technique is a scheme for studying the natural time evolution of classical system of the number of particles N in the volume of the simulation cell V. In such simulations, the total energy E is a constant of motion. Assuming that time averages are equivalent to ensemble averages, then the time averages obtained in a conventional MD simulation are equivalent to ensemble averages in the microcanical or constant-NVE ensemble. However, integration errors, force fluctations and inconsistencies in the forces usually generated by the cutoff may cause slow drifts in the total energy. Additionally, the total energy is constant, but not the kinetic and potential energy contributions, so a system that is not in equilibrium will go to it while the temperature changes. It is therefore desirable to have some way of controlling the temperature. Furthermore, it is more convenient to perform simulations at constant temperature or pressure in order to be able to compare the simulation results with experiment.

- Constant temperature simulations: The temperature of the system is related to the time average of the kinetic energy, which for an unconstrained system is given by:

$$E_{NVT} = \frac{3}{2} N k_B T. \tag{50}$$

An obvious way to alter the temperature of the system is thus to scale the velocities.[137] If the temperature at time t is $T(t)$ and the velocities are multiplied by a factor λ, then associated temperature change can be calculated as follows:

$$\Delta T = \frac{1}{2} \sum_{i=1}^{N} \frac{2}{3} \frac{m_i \left(\lambda v_i\right)^2}{N k_b} - \frac{1}{2} \sum_{i=1}^{N} \frac{2}{3} \frac{m_i v_i^2}{N k_b} \tag{51}$$

$$\Delta T = \left(\lambda^2 - 1\right) T\left(t\right) \tag{52}$$

$$\lambda = \sqrt{T_B / T\,(t)}. \tag{53}$$

The simplest scheme to control the temperature is the so called velocity scaling. It consists on scaling all the velocities by a factor $\lambda = \sqrt{T_B / T\,(t)}$, where T_B is the desired temperature and $T\,(t)$ is the current temperature of the system. This scaling can be done regurlaly, every N_{scale} steps, or whenever $T\,(t)$ goes out of some specified limits. However this method does not allow to sample the true canonical or NVT ensemble and the scaling affects the dynamics of the system in an unpredictable way.

A more physical way of controlling the temperature is to use the thermostat proposed by Berendsen,[138] consisting in a weak coupling of the system to a heat bath. The bath acts as a source of thermal energy, supplying or removing heat from the system as appropriate. The velocities are scaled at each step, such that the rate of change of temperature is proportional to the difference in temperature between the bath and the system:

$$\frac{dT\,(t)}{dt} = \frac{1}{\tau}\left(T_{bath} - T\,(t)\right), \tag{54}$$

τ is a coupling parameter whose magnitude determines how tightly the bath and the system are coupled together. The scaling factor for the velocities is

$$\lambda^2 = 1 + \frac{\delta t}{\tau}\left(\frac{T_{bath}}{T\,(t)} - 1\right). \tag{55}$$

If τ is large, then the coupling will be weak, $\tau_T \rightarrow \infty$. If τ is small, the coupling will be strong and when the coupling parameter equals the time step $(\tau_T = \delta t)$ the the algorithm is equivalent to the simple velocity scaling method. The advantage of this approach is that it does permit the system to fluctuate about the desired temperature. However it does not allow to sample the correct canonical ensemble and it can affect the system dynamics when small values of τ_T are used.

The Andersen thermostat also uses the coupling to a heat bath, but in this case the coupling is represented by stochastic forces that act occasionally on randomly selected particles and the coupling strength determines the frequency of the collisions. Between stochastic collisions, the system evolves at constant energy according to the normal Newton laws of motion. At each collision the particle gets a new velocity selected from a Maxwell-Boltzmann distribution corresponding to the bath temperature T_B.[139] Contrary to the previous

methods, the Andersen thermostat samples the canonical ensemble, but the dynamics of the system are depend on the collision frequency.

The Langevin thermostat is also a stochastic thermostat that controls the temperature by modifying the forces by adding a frictional force and a random force.[140] The balance of these two contributions mimics the exchange of energy with a surrounding heat bath. The frictional force and the random force combine to give the correct canonical ensemble. The amount of friction is controlled by the damping coefficient. If its value is high, atoms will experience too much unnatural friction, however, if the coefficient is too low, the system will fluctuate too far away from the desired temperature. One advantage of the Langevin thermostat and other stochastic-based thermostats is that they can be used with a larger time step than in NVE simulations. This has proven invaluable in simulations of more complicated systems than simple liquids, namely linear polymers, which have very long relaxation times.

The extended system method was originally introduced by Nosé and subsequently developed by Hoover. The idea is to consider the heat bath as an integral part of the system by the addition of an artificial variable associated with a fictional "heat bath mass" to the equations of motion. An important feature of this method is that the temperature can be controlled without involving random numbers. Thus correlated motions are not impaired and this method describes kinetics and diffusion properties better. Because the time-evolution of the added variable is described by a second-order equation, heat may flow in and out of the system in an oscillatory fashion, leading to nearly periodic temperature fluctuations with the frequency proportional to the "heat bath mass".[141–143] The drawback of this thermostat is that it was shown to impart the canonical distribution as well as ergodicity of the thermostatted system. The time constant parameter in this thermostat controls the period of temperature fluctuations at equilibrium.

The Nosé-Hoover-chains is a modification of the Nosé-Hoover thermostat which includes not a single thermostat variable but a chain of variables.[144] A Nosé-Hoover thermostat with one variable does not guarantee ergodicity, especially for small or stiff systems. Chaining variables behave better for small or stiff cases, however, an infinite chain is required to completely correct these issues.

- Constant pressure simulations: The approaches to control the pressure are anologous to those used for the temperature control. The pressure can be maintained at a constant value by simply scaling the volume. It has also to be

noted that the volume of the cell can be varied uniformly in the three spatial directions, or that both the shape and the volume of the cell can be changed. An alternative is to couple the system to a 'pressure bath', analogous to a temperature bath.[138] The rate of change of pressure is given by

$$\frac{dP(t)}{dt} = \frac{1}{\tau_p}\left(P_{bath} - P(t)\right), \tag{56}$$

τ_p is the coupling constant, P_{bath} ir the pressure of the 'bath', and $P(t)$ is the actual pressure at time t. The volume of the simulation box is scaled by a factor λ, which is equivalent to scaling the atomic coordinates by a factor $\lambda^{1/3}$.

CHAPTER 2.
ION PAIRING OF [C10MIM][CL] IN MOLECULAR SOLVENTS

Many of the ILs chemical and physical properties, such as acidity, electrical conductivity, ability to solvate solutes of different polarities, or miscibility with water as well as with organic solvents, can in principle be tailored for specific needs.[14,27–30] At lower concentration of the IL in the molecular solvent, ion pairing is an important phenomenon where dynamic equilibrium between free ions, solvent-separated and contact ion pairs as well as higher-order neutral or charged ionic aggregates is established which is sensitive to the concentration of the IL.[145,146] Indeed, the low-concentration aqueous solutions of ILs behave as traditional electrolytes where ions are virtually completely solvated,[17,45,46,50,110,111] although in some instances ion pairing was detected even at rather low concentrations of the IL.[71,147] In acetonitrile, it seems that ionic aggregates do not break into separate ions, apparently due to the poorer hydrogen bonding accepting abilities.[48,49,53,54] At low concentrations in nonpolar solvents, lone contact ion pairs were seen to be the dominant association pattern for some ILs in dichloromethane.[58,59] In this thesis, the definition of the hydrogen bond in ionic liquids is considerably different from that of conventional hydrogen bonds. The interaction is significantly stronger and has not strong directionality compared to conventional hydrogen bonds.[99]

In one particular case, the NMR signal of the proton of the 2nd position in the solutions of [C10mim][Br] IL has displayed a rather strong solvent dependence as it was found to be the highest at about 10.6 ppm in DCM, and the lowest at about 8.9 ppm in water with the intermediate chemical shift at around 10.3 ppm recorded in ACN solvent.[148] These results clearly reflect the shifting equilibrium between ionic aggregates and free ions in these three solvents which differ in both polarity and capabilities for hydrogen bonding. To elucidate the effect of different molecular solvents on ion pairing at low concentrations of the IL, the ^{1}H NMR calculations of 1-decyl-3-methyl-imidazolium chloride [C10mim][Cl] in solutions of water, ACN and DCM were performed.

Chloride anion was selected because it has considerably less electrons compared to Br^- anion, therefore the calculations of the electronic structure is simplified as well as the computational burden is lower. As well, a new experimental NMR measurements of the [C10mim][Cl] IL dissolved in ACN, DCM and water were performed, where the molar fraction of the IL was equal to 10^{-5}.

To assess the equilibrium between different states of the ions and to get a detailed microscopic picture of ion pairing phenomenon in the studied mixtures of IL and three molecular solvents, an integrated computational approach was used. This approach incorporates classical molecular dynamics simulations for sampling the phase space of the molecular system at given thermodynamic conditions and a combined quantum mechanics/molecular mechanics model for calculations of the NMR shielding constants.[149,150] Such a computational scheme allows accounting for the solvent effects on the NMR properties in an effective and accurate manner.[151–157]

2.1 COMPUTATIONAL DETAILS

2.1.1 Classical MD simulations

Classical molecular dynamics simulations were performed in order to address structural features of the [C10mim][Cl] contact ion pair in the solutions of water, acetonitrile and dichloromethane as well as to generate a number a statistically uncorrelated molecular solute – solvent configurations to be used in the subsequent QM/MM calculations of the electronic NMR properties. All MD simulations have been carried out using the Amber12 program.[158] The geometries of the $C10mim^+$ cation in all-anti conformation of the decyl group, ACN and DCM molecules were optimized at the HF/6-31G* level of theory[159,160] using Gaussian09 program.[161] Lennard-Jones parameters were applied for the $C10mim^+$ cation and the chloride anion where the parameters based on the Amber force field were developed specifically for the imidazolium family of ionic liquids according to Liu et al.[162] For acetonitrile and dichloromethane, parameters from the general Amber force field[163,164] were employed. The point charges for C10mim, ACN and DCM molecules were derived by means of the restrained electrostatic potential, RESP, procedure[165] as implemented in the Antechamber module[166] of Amber12 program.[158] These point charges were based on the electrostatic potentials computed at the HF/6-31+G* level using Gaussian09 program, in accordance with

the procedure used in work of Liu et al.[162] The standard TIP3P potential was used for water molecules.[167] The solutions of [C10mim][Cl] in DCM, ACN and water were represented by one [C10mim][Cl] ion pair and 2030 DCM, 2490 ACN and 2735 water molecules, respectively. In addition, MD simulations were performed using two different initial conditions in each of the three cases – starting from the contact ion pair or from the configuration where both ions are free and completely solvated by the solvent. The initial configurations were constructed using Packmol program.[168]

MD simulations were carried out using the Sander module of Amber12. Periodic boundary conditions were employed, and a cut-off of 10 Å was used for nonbonded interactions. The SHAKE algorithm[169] was imposed to constrain all bonds involving hydrogen atoms, and the SETTLE scheme[170] was used to ensure rigidity of the water molecules in the simulations. The equations of motion were integrated using the leap-frog algorithm with the time step of 1 fs. All systems were simulated using the Langevin thermostat to control the temperature set to 297.15 K with the collision frequency of 3.0 ps^{-1}. For each of the simulated systems, an initial simulation in the NPT ensemble at the pressure set to 1 bar was conducted for 300 ps in order to equilibrate the density. Then, the simulation in the NVT ensemble followed for 200 ps, and finally continuing with the production run of 1 ns. Molecular configurations were recorded every 0.5 ps for further analysis.

2.1.2 Electronic structure calculations

To select a reliable electronic structure method for the calculation of the NMR isotropic shielding constants, a series of benchmark calculations on an 1,3-dimethylimidazolium, $C1mim^+$, cation was performed. The C_{2v} geometry of the isolated $C1mim^+$ cation was optimized by the B3LYP functional[171] together with the aug-cc-pVTZ basis set[172,173] using Gaussian09 program. To select a reliable DFT method, a series calculations using the B3LYP,[171] PBE0,[174] and KT3[175] density functionals as well as *ab initio* MP2 method were performed. The coupled cluster singles and doubles, CCSD, computations were performed to gauge the accuracy of the aforementioned methods. Basis sets due to Ahlrichs[176] (def2-X(Z)VP(D), where X=S, T, Q) and Dunning[172,173,177] (aug-cc-p(C)VXZ, where X=D, T, Q) were considered. Gauge-including atomic orbital, GIAO, approach was used to obtain origin-independent NMR isotropic shielding constants. The DFT calculations were performed using Gaussian09 program,[178] while MP2 and CCSD computations

were done using CFOUR.[179]

The so–called supermolecular approach to account for solvent effects on the NMR properties of the C10mim$^+$ cation was also employed. Here, the geometries of the C10mim$^+$ cation and of its aggregates with chloride anion as well as with water, ACN and DCM molecules were optimized using the B3LYP functional along with the 6-31++G** basis set.[160] Gaussian09 program was employed to carry out these geometry optimizations and calculations of NMR properties using the PCM model with default settings for all solvents of water, ACN and DCM.

The calculations of the NMR isotropic shielding constants have been carried out using the QM/MM method based on GIAO-DFT approach [150,180] implemented in the Dalton electronic structure program.[178] The point charges for ACN and DCM molecules used in the QM/MM calculations were derived by fitting to the electrostatic potential computed at the B3LYP/aug-cc-pVTZ method along with the polarizable continuum method, PCM,[181] according to the CHELPG procedure together with the constraint on the magnitude of the dipole moment.[182] These calculations were conducted using Gaussian09 program. For water molecules, point charges from the TIP3P force field[167] were used and the polarizable potential by Ahlström[115] was also employed for comparative purposes. The liquid–state results for NMR shielding constants are obtained as statistical averages over 100 molecular configurations selected from the MD trajectories at regular intervals of 10 ps. A spherical cut–off radius was applied centered at the center of mass of the C10mim$^+$ cation for every molecular configuration, resulting in an average number of 1050 water and DCM or 1290 ACN solvent molecules included in a single QM/MM calculation. The chemical shifts were evaluated with respect to the shielding constant of equivalent protons in TMS. The geometry of the isolated TMS has been here optimized at the Hartree-Fock level together with the 6-31+G* basis set in order to be consistent with the protocol adopted for the development of the AMBER type force field for the C10mim$^+$ cation applied in the MD simulations.[162] The shielding constant for the protons of TMS of 31.91 ppm was then obtained using the PBE0 exchange-correlation functional and the def2-TZVP basis set.

2.2 METHOD ANALYSIS

In order to select an appropriate electronic structure method for the computation of the ^{1}H NMR chemical shifts for imidazolium cations, a series of benchmark calculations on the C1mim$^+$ cation was performed. The structure and atom labeling of the C1mim$^+$ cation are shown in Figure 5. The relative chemical shifts of the C1mim$^+$ cation were considered as these are easier to compute accurately as compared to the istropic shielding constants due to the apparent cancelation of errors.

Because the QM/MM calculations of NMR chemical shifts were performed at the DFT level of theory, the PBE0 functional has been selected for the basis set analysis of the relative chemical shifts. The relative ^{1}H NMR chemical shifts for H2 and H4/5 protons are evaluated with respect to the arithmetic average of the protons in the methyl group of C1mim$^+$. The number of contracted basis functions is indicated in paranthesis for each basis in Table 1. As seen in Table 1, the relative chemical shifts are apparently well-converged for the most extensive basis set which is aug-cc-pCVQZ. The effect of tight core functions included to the Dunning-type basis sets is rather small. In general, we see that reasonable results for the relative ^{1}H NMR chemical shifts can be expected with all basis sets but Ahlrich's single valence type basis sets, thus corroborating the findings in ref.[183] Based on the results of the relative ^{1}H NMR chemical shifts the def2-TZVP basis set for further calculations of the NMR isotropic shielding constants of C10mim$^+$ cation was chosen. The choice is based on the relatively large size of the cation and it was proven to be appropriate for NMR properties of other organic molecules in the liquid phase.[152]

The results of relative ^{1}H NMR chemical shifts of the C1mim$^+$ cation computed using three different DFT functionals, the MP2 and CCSD approaches combined with the def2-TZVP basis set are collected in Table 2. Interestingly, we have found considerable differences between the relative chemical shifts computed using the correlated *ab initio* MP2 and CCSD methods. The PBE0 functional is seen to provide relative chemical shifts which are closest to the corresponding CCSD predictions. On this basis, the PBE0 exchange-correlation functional has been chosen along with the def2-TZVP basis set for all further calculations of NMR isotropic shielding constants of the imidazolium cations in this work.

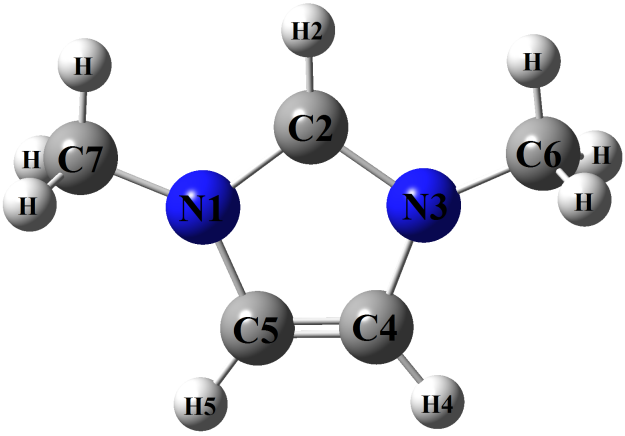

Figure 5: 1,3-Dimethylimidazolium cation, C1mim$^+$.

Table 1: Relative ^{1}H NMR chemical shifts (in ppm) for the C1mim$^+$ cation.

Basis set	H2	H4/5
def2-SVP(143)	3.50	3.47
def2-SVPD(228)	3.79	3.48
def2-TZVP(271)	3.88	3.61
def2-TZVPD(340)	3.99	3.57
def2-QZVP(669)	3.91	3.58
def2-QZVPD(738)	3.93	3.57
aug-cc-pVDZ(242)	3.88	3.52
aug-cc-pVTZ(529)	3.94	3.56
aug-cc-pVQZ(947)	3.91	3.55
aug-cc-pCVDZ(270)	3.86	3.52
aug-cc-pCVTZ(620)	3.92	3.55
aug-cc-pCVQZ(1177)	3.90	3.55

Table 2: Relative ^{1}H and ^{13}C NMR chemical shifts (in ppm) for the C1mim cation.

Method	H2	H4/5
PBE0	3.88	3.61
B3LYP	3.83	3.54
KT3	3.69	3.48
MP2	3.65	3.59
CCSD	3.89	3.57

2.3 ^{1}H NMR RESULTS SUPERMOLECULAR APPROACH

To predict molecular properties of solvated molecules, a supermolecular approach is widely used, where specific interactions between the solute and the solvent are accounted for by geometry-optimizing small solute-solvent molecular aggregates along with the PCM model to account for the bulk solvent effects. This approach allows for comparatively accurate molecular geometries which are indeed important as much as NMR chemical shifts are concerned. However, the energy-minimized structure of the molecular aggregate does represent only one point on the molecular potential energy hypersurface meaning that the dynamical solute-solvent effects remain here completely neglected.

The calculated NMR chemical shifts of the H2 atom for the geometry-optimized C10mim^{+} cation and its complexes with water, ACN and DCM molecules as well as with the Cl^{-} anion are presented in Table 3. Only the hydrogen-bonded complexes formed through the C2-H2 moiety of the imidazolium ring were considered. The optimized complexes are illustrated in Figure 6. Contrary to the case of the isolated ion pair,[184,185] the configuration of the [C10mim][Cl] aggregate where the chloride anion is situated on top of the C2-H2 bond is not a minimum on the potential energy surface when PCM is applied. The minimum on the potential energy surface is reached for the configuration with the chloride anion in the plane of the imidazolium ring as shown in Figure 6D. NMR chemical shifts given in Table 3 have been evaluated with respect to the ^{1}H NMR isotropic shielding constant of TMS of 31.62 ppm computed using the geometry of TMS optimized at the same level of theory as the molecular complexes. The experimental NMR measurements of the [C10mim][Cl] IL dissolved in ACN, DCM, and water where the molar fraction of the IL is equal to 10^{-5} in solutions were carried out by the experimental NMR group of the Institute of Chemical Physics at Vilnius University.

Table 3: Supermolecular results for the NMR chemical shifts of the H2 proton of the $C10mim^+$ cation

System	δ(H2), ppm
C10mim in water	8.03
C10mim + H_2O in water	10.02
C10mim in ACN	8.03
C10mim + ACN in ACN	9.05
C10mim + Cl in ACN	11.44
C10mim in DCM	8.00
C10mim + DCM in DCM	8.37
C10mim + Cl in DCM	12.20
Expmnt. (water)	8.66
Expmnt. (ACN)	9.23
Expmnt. (DCM)	10.83

Results showed that the chemical shift of the H2 atom in $C10mim^+$ cation is virtually the same in all three solvents if lone $C10mim^+$ cation is immersed in the PCM cavity. The inclusion of the hydrogen-bonded solvent molecule has a very large effect on the chemical shift of H2 proton, leading to the additional deshielding by around 2 and 1 ppm in water and ACN, respectively. Even though DCM has weak hydrogen bond accepting abilities, the shielding constant of H2 atom in the complex of $C10mim^+$ cation and DCM molecule is increased by substantial $\sim$0.4 ppm as compared to the case where DCM solvent is represented entirely by the dielectric continuum. The chemical shift of the H2 atom in the complex of the $C10mim^+$ cation with the water molecule of 10.02 ppm is considerably overestimated as compared to the experimental chemical shift of 8.66 ppm measured for the aqueous solution of the [C10mim][Cl] IL.

In ACN, supermolecular approach predicts that the equilibrium to be shifted towards the free ions rather than contact ion pairs. Experimental chemical shift of the H2 atom of 10.83 ppm measured for the [C10mim][Cl] solution in DCM is situated roughly in the middle of the corresponding chemical shifts predicted for the complexes of $C10mim^+$ with chloride anion and DCM molecule suggesting ample dissociation of the [C10mim][Cl] in DCM solution.

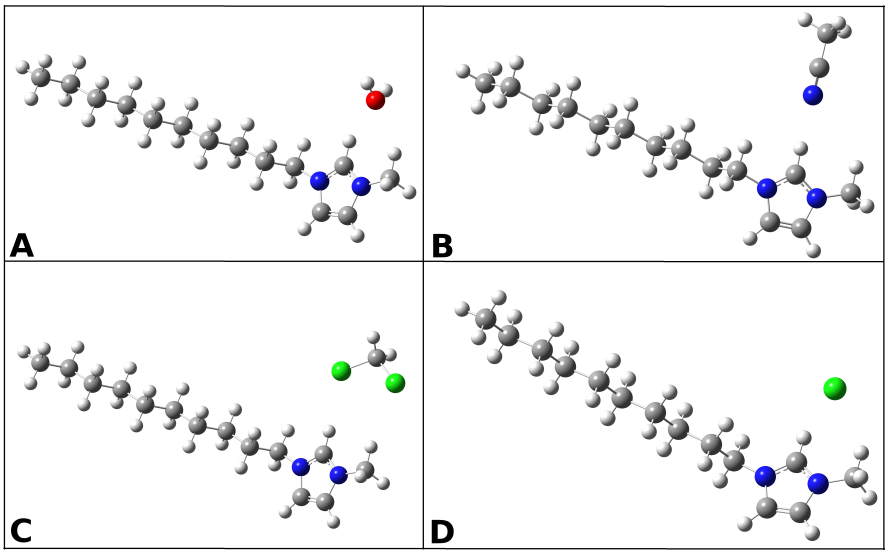

Figure 6: Energy-minimized complexes of the C10mim$^+$ cation with water (A), ACN (B), DCM (C) molecules as well as the Cl^- anion (D).

2.4 MD SIMULATIONS: STRUCTURAL ANALYSIS

In order to properly describe solvent effects it is important to consider a large number of solvent molecules around the solute. Classical MD simulations were performed to generate an appropriate number of solute-solvent configurations. MD simulations were performed for [C10mim][Cl] ionic pair dissolved in the solvents of different polarity: dichloromethane, acetonitrile and water with different number of molecules which were included into the system, 2030, 2490 and 2735 molecules, respectively. Radial distribution functions (RDFs), distributions of angles and dihedral angles of the first solvation shell for C10mim$^+$ cation in different solvents were considered, to inspect the local distribution of molecules around the imidazolium ring. Radial distribution function describes how the distribution of particles varies with the distance to the reference particle and the function is expressed as

$$g(r) = \frac{dN}{4\pi r^2 \rho dr}, \tag{57}$$

here, $\rho = N/V$ is the average number density of particles, where N is the number of particles in the system, r is the distance between the reference particle and any particle in the system, 4π – spacial angle.

The three solvents in two different cases were considered: in the first case, the [C10mim][Cl] ionic pair is dissociated and in the second case, the

[C10mim][Cl] ionic pair is not dissociated and have formed hydrogen bonding between H2 and Cl^- anion. The simulated cation-anion radial distribution functions revealed the most probable distance to find anion around H2 proton in DCM and ACN solutions at around 2.3 Å and 2.5 Å, respectively. The distance in water was not calculated because the [C10mim][Cl] ionic pair dissociates during equilibration stage of the MD simulations.

Based on the RDFs, the first solvation shell of the counterion can be defined according to a distance to the first minimum. By this definition, the structure of the first solvation shell around the proton at 2nd position was analyzed. The distribution of the hydrogen bond C2-H2...Cl^- angle in DCM and ACN solutions is presented in Fig. 7a. In ACN solvent, there is one clear peak at around 130°. Similar feature is observed in DCM solvent, with a peak at around 140–155°. The results of the angular distribution revealed that the hydrogen bond angle is strongly non–linear and the angle is found to be smaller in ACN rather than in DCM solvent. The distribution of the dihedral angle N1-C2-H2...Cl^- shown in Fig. 7b illustrates quite clearly that the chloride anion tends to be located out of the plane of the imidazolium ring with roughly the same probability of being on either side of it in both solvents. In addition, the anion is seen to have the preference for leaning more toward the methyl side rather than the decyl group side, apparently, due to the steric effects.

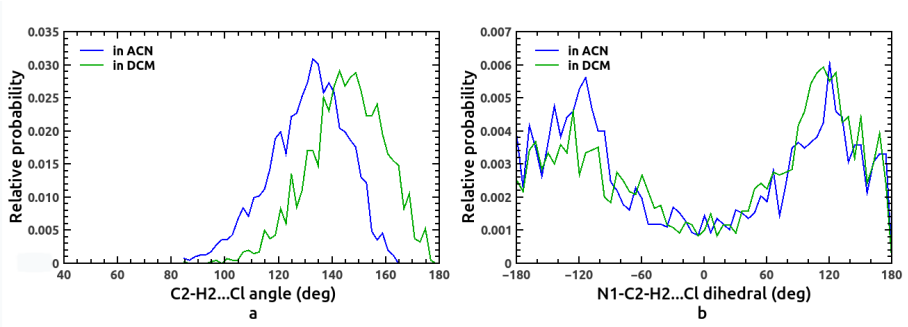

Figure 7: Angles and dihedral angles of [C10mim][Cl] ionic pair and solvent molecules around the C2-H2 moiety.

Figure 8 shows RDFs between the H2 atom of the free $C10mim^+$ cation and the electronegative atoms in the molecules of each of the three solvents: the oxygen atom of water, the nitrogen atom of ACN, and the chlorine atoms of DCM. These RDFs were recorded during MD simulations of dissociated [C10mim][Cl] ion pairs. The RDFs indicate some association of the $C10mim^+$ cation with the solvent molecules through C2–H2 bond of the imidazolium

ring. The association is proved by a sharp first peak at around 2.4 Å in ACN and other less pronounced two peaks at around 2.7 Å and 2.6 Å in DCM and water solutions, respectively. It is worth mentioning that the presence of the secondary peaks at around 6.0 Å, 6.5 Å and 6.2 Å in ACN, DCM and H_2O, respectively, is due to presence of solvent molecules around H4 and H5 protons of the imidazolium ring. Spherical integration of the first peaks in the RDFs in Figure 8 gives an average number of corresponding atoms of solvent molecules in the vicinity of the C2-H2 moiety. These numbers were found to be 3.7, 2.9 and 3.6 in DCM, ACN and aqueous solution, respectively. The spherical integration of the first peak of the RDF between H2 atom of imidazolium and carbon atom of DCM molecules extended up to 5.23 Å results in the coordination number of 2.8. Thereby, we barely see any specific interactions between the C10mim$^+$ cations and rather nonpolar DCM molecules.

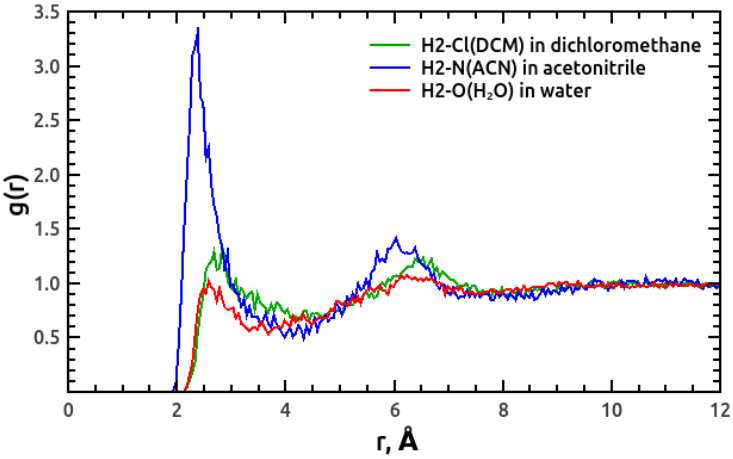

Figure 8: Radial distribution functions between H2 atom in C10mim$^+$ cation and Cl, N as well as O atoms in DCM, ACN and water, respectively.

To scrutinize the local distribution of the solvent molecules around the C2-H2 bond in the C10mim$^+$ cation in some more detail, the analysis of the distributions of the C2-H2...X angle and the N1-C2-H2...X dihedral angle were performed, where X corresponds to the O, N and Cl atoms in water, ACN and DCM molecules, respectively, see Figure 9. These distributions have been compiled by considering only those solvent molecules for which the distance between the H2 atom and O atom of water, N atom of ACN and Cl atoms of DCM does not exceed 3.7, 4.3 and 4.4 Å, respectively. These cutoff values are based on the RDFs shown in Figure 8. As seen in Figure 9a, the angular distri-

bution peaks at around 130°. The angular distribution shows that the solvent molecules tend to be located above the imidazolium ring within the applied thresholds for the atomic distances. The distributions of dihedrals shown in Figure 9b are very similar to the distribution of corresponding dihedral angles between the cation and the anion in the [C10mim][Cl] contact ion pair shown in Figure 7b, indicating again that solvent molecules tend to be positioned out of the imidazolium ring plane.

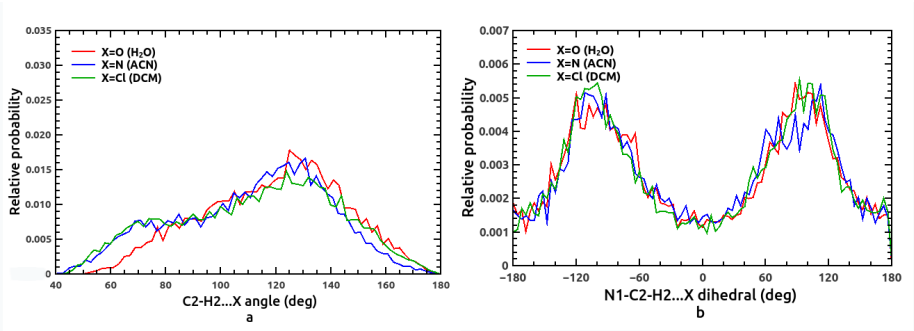

Figure 9: Angles and dihedral angles of the C10mim$^+$ cation and solvent molecules around the C2-H2 moiety.

2.5 ^{1}H NMR RESULTS BY QM/MM METHOD

The QM/MM results for the ^{1}H NMR isotropic shielding constants of the H2 proton in the imidazolium ring of the solvated C10mim$^+$ cation are presented in Table 4. Statistical errors are evaluated as standard deviations of the sample, and are provided in parentheses. The state of the [C10mim][Cl] ion pair in the system is indicated as FI for free ions or CP for contact ion pair. In the second column, the three integers given in parentheses indicate the numbers of solvent molecules – and chloride in case of the CP – promoted to the QM region closest to H2, H4 and H5 atoms, respectively. Each entry for the shielding constant in Table 4 is obtained as an average over 100 molecular configurations recorded during the MD simulation.

For the free C10mim$^+$ cation in aqueous solution, the NMR shieldings were computed using two types of the classical potential for all water molecules – the non-polarizable TIP3P as well a polarizable potential due to Ahlström *et al.*[115] The latter potential includes isotropic molecular dipole polarizability assigned to the oxygen atom in addition to the three partial atomic point charges. As seen in Table 4, the results for the shielding constant of the H2 proton com-

Table 4: NMR isotropic shielding constants, σ, (in ppm) of the H2 proton of the C10mim$^+$ cation in water, ACN and DCM.

System	QM region	σ(H2)
FI in water	C10mim	23.64 (0.07)
	C10mim†	23.62 (0.07)
	C10mim (1,1,1)	23.31 (0.08)
	C10mim (3,1,1)	23.08 (0.09)
FI in ACN	C10mim	23.62 (0.03)
	C10mim (1,1,1)	23.09 (0.05)
	C10mim (3,1,1)	23.00 (0.05)
CP in ACN	C10mim	23.30 (0.04)
	C10mim (2,1,1)	21.44 (0.08)
	C10mim (3,1,1)	21.50 (0.08)
FI in DCM	C10mim	24.02 (0.03)
	C10mim (1,1,1)	23.52 (0.06)
	C10mim (3,1,1)	23.41 (0.06)
CP in DCM	C10mim	23.23 (0.03)
	C10mim (2,1,1)	21.29 (0.09)
	C10mim (3,1,1)	21.33 (0.08)

† – computed using polarizable potential for water molecules.[115]

puted using both potentials are virtually identical, therefore it has been chosen to use non-polarizable potentials for all classical solvent molecules of water, ACN and DCM in all subsequent QM/MM calculations.

In the QM/MM scheme utilizing non-polarizable potentials, the inclusion of some of the solvent molecules to the quantum mechanically treated region of the model offers an improved description of electrostatic interactions between the solute and the solvent. In addition, a solute-solvent polarization as well as non-classical effects such as Pauli repulsion are introduced. It is typically mandatory to treat the solvent molecules forming the hydrogen bonds with the solute using the QM approach rather than to describe them by a classical potential, so that both the hydrogen bond donor and acceptor molecules are considered on an equal footing.[151–153,155,156] Thus, the QM part of the model was expanded by a few relevant solvent molecules as well as Cl^- anion in the case of the simulated contact ion pair. Here, up to 3 molecular species closest to the H2 atom were included to the region of the model treated quantum mechanically by DFT. In addition, two solvent molecules closest to the H4 and H5 atoms were also promoted to the QM part to make sure all hydrogen bonding interactions involving the imidazolium ring of $C10mim^+$ are accounted for consistently. As seen in Table 4, 3 solvent molecules,– or 2 solvent molecules plus the Cl^- anion in case of the contact ion pair,– is a sufficient expansion of the QM region to obtain a converged effect on the shielding constant of the H2 atom.

The improved description of intermolecular interactions has a marked effect on the shielding constant of the H2 proton. In the case of the free $C10mim^+$ cation, the shielding constant is decreased by around 0.5-0.6 ppm as compared to the case where only the cation is considered at the DFT level and all solvent molecules are represented by the point charge potential, for all three solutions. The effect is even stronger for the contact ion pair. Here, the shielding constant of the H2 atom is decreased by 1.8-1.9 ppm comparing to the case where both the anion and all solvent molecules are represented by the potential. As seen in Table 4, the hydrogen bonding between the $C10mim^+$ cation and the chloride anion has a significant modulating effect on the magnitude of the shielding constant of the H2 atom, while hydrogen bonding between $C10mim^+$ and solvent molecules as well as polarity of the solvent is clearly of less importance. Indeed, formation of the contact ion pair leads to the deshielding of the H2 atom by 1.5 and 2.1 ppm compared to the corresponding shielding constant of the free cation in ACN and DCM solution, respectively. However, the shield-

Table 5: NMR chemical shifts, δ, (in ppm) of the H2 proton in the imidazolium ring of the C10mim$^+$ cation in water, ACN and DCM evaluated with respect to TMS.

System	δ(H2)
FI in water	8.83
FI in ACN	8.91
CP in ACN	10.41
FI in DCM	8.50
CP in DCM	10.58
Expmnt. (water)	8.66
Expmnt. (ACN)	9.23
Expmnt. (DCM)	10.83

ing constants of the H2 atom for the contact ion pair differ by a mere 0.17 ppm in ACN and DCM solution. The shieldings of H2 proton for the free C10mim$^+$ are virtually identical in ACN and water, and it is somewhat larger in DCM by around 0.4 ppm.

Computational predictions for the ^{1}H NMR chemical shifts of the H2 atom in the [C10mim][Cl] contact ion pair and in the free C10mim$^+$ cation in the solutions of water, ACN and DCM are collected in Table 5. These results are based on the isotropic shielding constants of the H2 proton calculated using the most extensive QM region in the QM/MM calculations as given in Table 4. The experimental results for the NMR chemical shifts of the H2 atom of [C10mim][Cl] IL solutions in water, ACN and DCM are also included in Table 5.

The QM/MM result for the chemical shift of the H2 proton in the free C10mim$^+$ cation in aqueous solution of 8.83 ppm compares very well to the experimental shift of 8.66 ppm. This finding lends support to the assumption that [C10mim][Cl] IL completely dissociates into free fully solvated ions in aqueous solution at these very low concentrations. In ACN, experimental chemical shift is found to be in-between those computed for the contact ion pair and for the free C10mim$^+$ cation, being closer to the latter. Assuming that chemical equilibrium in ACN is established only between the dissociated state of the ions and the contact ion pairs formed via hydrogen bonding solely through the C2-H2 bond of the imidazolium ring, the fraction of the contact

ion pairs, $X_{\mathrm{ACN}}^{\mathrm{CP}}$, was evaluated according to

$$X_{\mathrm{ACN}}^{\mathrm{CP}} = \frac{\delta_{\mathrm{ACN}}^{\mathrm{exp}} - \delta_{\mathrm{ACN}}^{\mathrm{FI}}}{\delta_{\mathrm{ACN}}^{\mathrm{CP}} - \delta_{\mathrm{ACN}}^{\mathrm{FI}}}. \tag{58}$$

In eqn. 58, CP and FI indicate the contact ionic pair and free C10mim$^+$ cation, respectively. Using data in Table 5, it was found that the $X_{\mathrm{ACN}}^{\mathrm{CP}}$ is equal to 0.23 meaning that on average one ion pair out of four or five is found in the aggregated state. It means that acetonitrile is in fact able to break the contact ion pairs of the [C10mim][Cl] IL apart, and the equilibrium is shifted towards the free fully solvated ions at molar fraction of the IL as low as 10^{-5}. Apparently, the driving force behind this phenomenon is the ability of the ACN molecules to form hydrogen bonding with the C10mim$^+$ cation, even though ACN molecules do not possess strong hydrogen bond donating abilities to solvate chloride anions efficiently.

As seen in table 5, the NMR chemical shift of the H2 atom measured for the sample of [C10mim][Cl] solution in DCM is higher compare to applied QM/MM prediction for the chemical shift of this atom in the cation-anion contact ion pair by 0.25 ppm. These results indicate that dissociation of the [C10mim][Cl] IL into free ions does not occur in the rather nonpolar DCM solution even at this extremely low concentration of the IL. On one hand, the discrepancy between experimental measurements and computational predictions in DCM solution may be due to the inaccuracies of the applied computational scheme. On the other hand, experimental findings indicate that the ions of the [C10mim][Cl] IL may form larger ionic aggregates rather than separate contact ion pairs in DCM.

2.6 CONCLUSIONS OF CHAPTER 2

- Classical MD simulations showed that [C10mim][Cl] ionic liquid breaks into free ions in aqueous solution completely. The predicted NMR chemical shift of the H2 atom of the free C10mim$^+$ cation in aqueous solution is found to agree well with the experimental value of the chemical shift of H2 atom for [C10mim][Cl] in aqueous solution.

- In acetonitrile, around 23% of the ion pairs were found to form contact pairs and the rest are broken into free ions.

- The model suggests that ion pair dissociation does not take place in the nonpolar dichloromethane solvent.

- The QM/MM model predicted that the chemical shift of the H2 atom in C10mim cation is primarily modulated by the hydrogen bonding with the chloride anion, while the effect of the solvent is rather insignificant.

- The results of applied supermolecular approach to predict the NMR chemical shifts of the H2 atom in C10mim cation, showed that results are less consistent with the experimental data than those based on the MD-QM/MM scheme.

Based on the results, the statement of the thesis is postulated as follows:

At low concentration of 1-decyl-3-methyl-imidazole chloride ionic liquid in aqueous solution, complete dissociation of ionic pairs into free ions takes place. Dissociation of ionic pairs does not occur of this ionic liquid in dichloromethane solution. In acetonitrile, an equilibrium is established between dissociated ions and contact ion pairs that is shifted more towards free ions.

CHAPTER 3.
[C4MIM][CL] IL AND ITS MIXTURES WITH WATER

Water has over the last decade been increasingly considered as an integral part of ionic liquid materials.[186] The mixtures of IL and water may acquire unique properties which are not necessarily associated with any of the two components.[17,33–35,67] To disclose molecular mechanisms behind the physicochemical properties of IL/ water mixtures, various experimental and theoretical techniques have been called in order to provide a detailed insight into molecular structure and dynamics of these heterogeneous systems.[16,69] Classical molecular dynamics simulations have led to the general conclusion that solitary water molecules are dispersed throughout the bulk of the IL when water content is rather low.[69,71,73–75,187] Under these circumstances, the isolated water molecules are found to primarily form hydrogen bonds with the anions, acting as bridges between them.[71,73–77] When the molar fraction of water increases, clusters of water molecules begin to emerge, and nanostructural organization of the mixture is enhanced.[71,74,77,187,188] Eventually, a continuous water network is formed which percolates the entire system and surrounds ionic clusters.

Measurements of water ^{1}H NMR chemical shifts for the aqueous mixtures of 1-butyl-3-methylimidazolium chloride, [C4mim][Cl], ionic liquid, were performed varying the molar fraction of the IL, χ_{IL}, in the range of 10^{-3} to 0.98. The measurements of the [C4mim][Cl]/ water mixtures were carried out by the experimental NMR group at the Institute of Chemical Physics of Vilnius University. The ^{1}H NMR chemical shift of water exhibits non-monotonic dependence on the composition of an aqueous mixture of [C4mim][Cl] IL as illustrated in Figure 10a. A clear minimum is observed for the ^{1}H NMR chemical shift at a molar fraction of the IL of 0.34. The data in Figure 10a suggests that chemical equilibrium between various water–ionic and water–water molecular aggregates may vary with the composition of the mixture. Interestingly, a smooth increase of the ^{1}H NMR chemical shift of the proton at the 2nd

position in the imidazolium ring, H2, was observed previously for the increasing molar fraction of the IL in the [C4mim][Cl]/water mixture as illustrated in Figure 10b.[110] The shape of the curve in Figure 10b could simply imply that water molecules are gradually replacing chloride anions in the vicinity of the C2–H2 moiety with the increasing content of water in the mixture.[189] Indeed, the increasing chemical shift of water seen in Figure 10a for χ_{IL} in the range of 0.34–0.98 can be expected due to the relative proliferation of water molecules bound to strongly hydrophilic chloride anions.

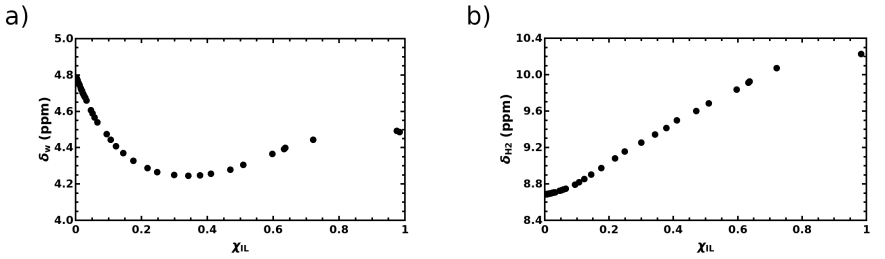

Figure 10: The ^{1}H NMR chemical shift of water, δ_{W}, (a) and of the proton at position 2 in the imidazolium ring of the C4mim$^+$ cation, δ_{H2}, (b) as a function of the molar fraction of the IL, χ_{IL}, in the mixture of [C4mim][Cl] IL and water.

To assess the structural organization of the [C4mim][Cl]/water mixtures reflecting the experimental NMR data in Figure 10, we relied on an integrated computational approach. This approach incorporates classical molecular dynamics simulations along with a combined quantum mechanics/molecular mechanics model to study various NMR parameters. In this work, this computationally expensive yet accurate computational technique is applied in order to provide rationalization of the experimental NMR data of [C4mim][Cl]/water mixtures.

3.1. COMPUTATIONAL METHODS

3.1.1 Classical MD simulations

Classical MD simulations were performed to address structural features of the neat [C4mim][Cl] IL and its mixtures with water. All MD simulations have been carried out using Amber18 program.[190] The geometry of the C4mim$^+$ cation was optimized at the HF/6-31G* level of theory using Gaussian09 program.[161] A Canongia-Lopes and Pádua potential was applied for the constituent ions of the [C4mim][Cl] IL,[191,192] and the TIP4P-Ew force

field was selected for water molecules.[193] Neat [C4mim][Cl] IL was simulated as a system of 1000 [C4mim] [Cl] ion pairs. An appropriate number of water molecules of 48, 1000 or 3000 was added to the 1000 ion pairs to get mixtures with molar fraction of the IL of 0.95, 0.50 or 0.25, respectively. The system of liquid water was represented by 1000 TIP4P-Ew water molecules. Initial configuration of each system was generated by placing ions and water molecules randomly in the simulation box by using the Packmol program.[168]

For the systems of neat IL and its mixtures with water, a short simulation of 50 ps in the NVT ensemble was executed at the temperature of 50 K after initial energy-minimization run. A series of ten 500 ps long simulations in the NPT ensemble followed where temperature was increased incrementally in steps of 50 K from 50 to 500 K. At 500 K, systems were simulated for 4 ns in the NPT ensemble. After that, all systems were cooled down to 298 K in steps of 50 K where the duration of each NPT simulation was 500 ps again. At ambient conditions, each system was simulated for 17 to 20 ns in the NPT ensemble to get converged mass densities. Then, the simulations in the NVT ensemble followed for 12 ns, and the trajectories recorded during the last 5 ns of the simulation were used in the structural analyses as well as for the QM/MM calculations. Similar protocol was executed to simulate liquid water, just all simulations have been carried out at ambient conditions, and the equilibration in the NPT ensemble for 500 ps was sufficient. Final simulation of liquid water at ambient conditions was carried out for 2.5 ns in the NVT ensemble.

MD simulations were carried out using the Sander module of Amber18. Periodic boundary conditions were employed, and a cutoff of 12 Å was used for nonbonded interactions. The SHAKE algorithm[169] was imposed to constrain all bonds involving hydrogen atoms. The equations of motion were integrated using the leap-frog algorithm with a time step of 1 fs. The temperature was controlled using the Langevin thermostat with a collision frequency of 3.0 ps^{-1}. The pressure was set to 1 bar in all MD simulations. The configurations were dumped at regular intervals of 10 ps during the production run phase.

3.1.2 QM/MM calculations

The QM/MM method[150,180] based on the gauge including atomic orbital method and density functional theory as implemented in the Dalton electronic structure program[178] has been used for the calculations of NMR isotropic shielding constants. The PBE0 exchange-correlation functional[174]

and Ahlrichs def2-TZVP basis set[176]—occasionally combined with the Pople style 3-21G basis[194]—were applied for the QM subsytem of the model. Classical subsytem was represented by point charges. The point charges for the C4mim$^+$ cations were derived by using the restrained electrostatic potential procedure, RESP,[165] implemented in the Antechamber module[166] of Amber18. The Hartree-Fock approach along with the 6-31G* basis set were used to optimize geometry of C4mim$^+$ cation and to compute potentials to be utilized in the RESP procedure using Gaussian 09 programs.[161] Point charges from the TIP3P potential[167] were used for water molecules. Condensed-phase results for NMR shielding constants are obtained as statistical averages over 100 molecular configurations selected from the MD trajectories at regular intervals of 50 ps for IL systems and of 20 ps for liquid water. A spherical cutoff radius has been applied centered at the center of mass of the central cation or water molecule for every molecular configuration, and the cut-off radius was set to 30 and 15 Å for IL systems and liquid water, respectively.

3.2 NEAT [C4MIM][CL] IL

3.2.1 Structural analysis

The radial distribution function between the H2 hydrogen atom in the C4mim$^+$ cations and the chloride anions in the neat [C4mim][Cl] IL is shown in Figure 11. Atom numbering in the C4mim$^+$ cation is represented in Fig-

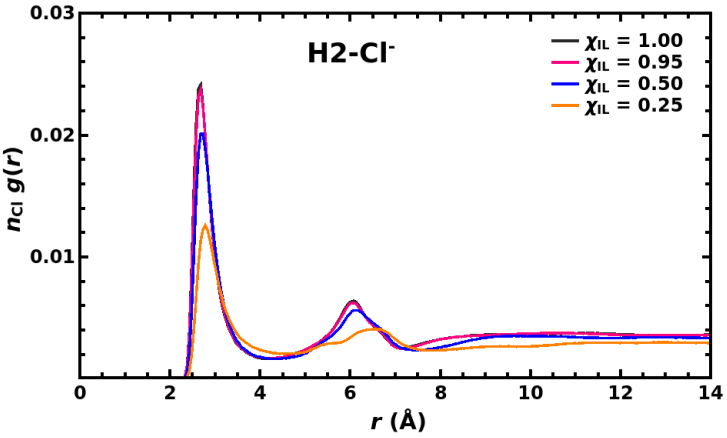

Figure 11: RDFs between H2 atom and Cl^- ion in neat [C4mim][Cl] IL and its mixtures with water, scaled by the number density of the chloride anions, n_{Cl}, for each specific system.

ure 12. The RDFs are scaled by appropriate number densities to facilitate the

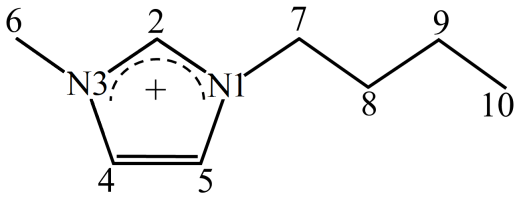

Figure 12: Atom numbering in C4mim$^+$ cation.

comparison of interionic and intermolecular distributions across systems of different composition.[195] A pronounced peak between 2.2 and 4.0 Å in Figure 11 demonstrates hydrogen bonding interaction between the C2-H2 moiety of imidazolium and the chloride anions.[99] The most probable distance is found to be 2.67 Å. Spherical integration of that peak up to 4 Å gives a coordination number of 1.47. Chlorides are also found to coordinate imidazolium through the C4-H4 and C5-H5 bonds. The RDFs of H4-Cl$^-$ and H5-Cl$^-$ shown in Figure 13 exhibit similar structure as that of H2-Cl$^-$ RDF in Figure 11. The most probable H4/5$\cdots$Cl$^-$ hydrogen bond lengths are equal to 2.67 Å, and spherical integration of H4-Cl$^-$ and H5-Cl$^-$ RDFs up to 4.0 Å gives the coordination numbers of 1.28 and 1.22, respectively. These results confirm the greater capacity of the C2-H2 moiety for hydrogen bonding as compared to that of C4-H4 or C5-H5.[99,196]

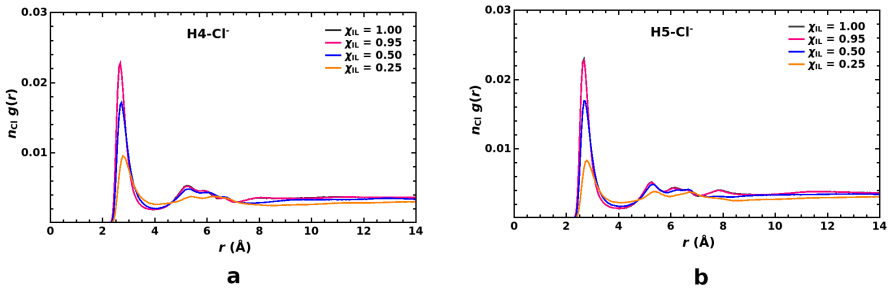

Figure 13: RDFs between H4 or H5 atom and Cl$^-$ ion in neat [C4mim][Cl] IL and its mixtures with water, scaled by the number density of the chloride anions, n_{Cl}, for each specific system.

The structural distribution of anions around the imidazolium ring was scrutinized in some more detail. The distribution of the C-H2$\cdots$Cl$^-$ angle which

is found of the sphere of 4 Å radius centered at the H2 atom were calculated and the results are presented in Figure 14. It is evident that hydrogen

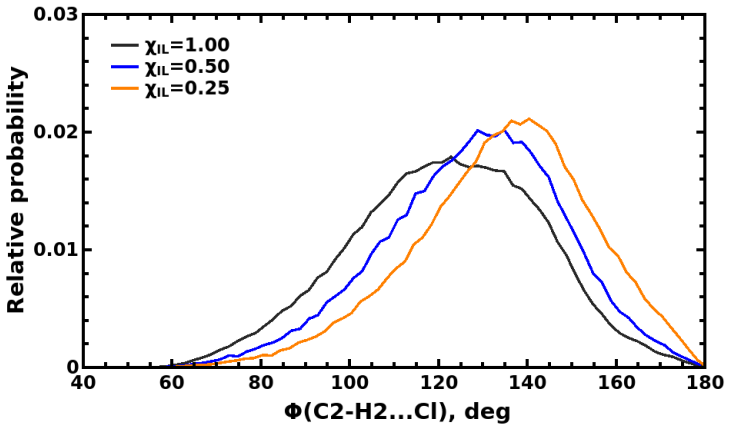

Figure 14: Distribution of the C2-H2$\cdots$Cl$^-$ angle, Φ, in neat [C4mim][Cl] IL and its mixtures with water for $R(\mathrm{H2}\cdots\mathrm{Cl}^-) \leq 4.0$ Å.

bond formed between the C2-H2 moiety and chloride is strongly non-linear. Thus the configuration of the linear C2-H2$\cdots$Cl$^-$ hydrogen bond which corresponds the global minimum of the potential energy surface for the isolated C4mim$^+$–Cl$^-$ ion pair is virtually absent in the neat liquid.[184] Some of the chloride anions are seen to approach the imidazolium ring from the top of the C2-H2 bond, and yet the most probable C2-H2$\cdots$Cl$^-$ angle lies in the range of around 110-140 deg. These findings are in line with the results of neutron diffraction measurements which indicate non-linear hydrogen bond between C2-H2 moiety and chloride in samples of 1,3-dimethyl-imidazolium chloride.[197] The distribution of the N1-C2-H2$\cdots$Cl$^-$ dihedral angle recorded in neat [C4mim][Cl] clearly shows that chloride anions tend to be located out of the plane of the imidazolium ring, see Figure 15. The distribution is symmetric with respect to the center point at 0 deg, and pronounced peaks at $\pm$120 deg indicate that anions rather prefer to stay on the methyl side of the C2-H2 bond. The location on the butyl side is less preferred likely due to the steric hindrance. These findings are confirmed evidently by spacial distribution function (SDF) of chloride anions around the imidazolium ring of C4mim$^+$ cation shown in Figure 16.

The distribution of the C4-H4$\cdots$Cl$^-$ and C5-H5$\cdots$Cl$^-$ angles in neat [C4mim][Cl] IL shown in Figure 17, exhibit similar shapes as that seen for the

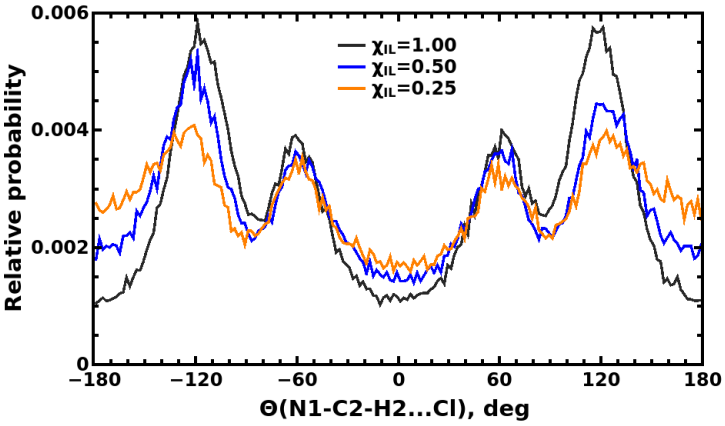

Figure 15: Distribution of the N1-C2-H2$\cdots$Cl$^-$ dihedral angle, Θ, in neat [C4mim][Cl] IL and its mixtures with water for $R(\mathrm{H2}\cdots\mathrm{Cl}^-) \leq 4.0$ Å.

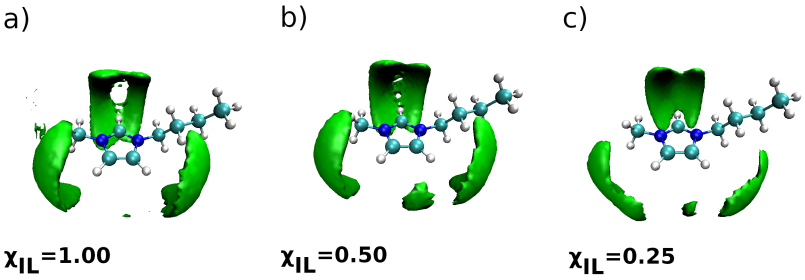

Figure 16: SDF of Cl$^-$ anions around the imidazolium ring of the C4mim$^+$ cation in (a) neat [C4mim][Cl] IL and its mixtures with water at χ_{IL} of (b) 0.50 and (c) 0.25.

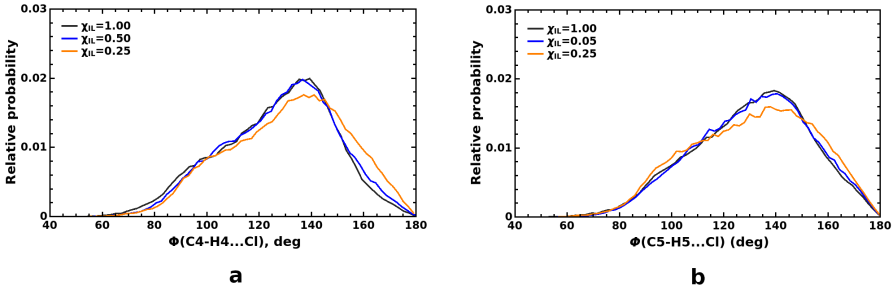

Figure 17: Distribution of the C4-H4$\cdots$Cl$^-$ angle, Φ, (a) and the C5-H5$\cdots$Cl$^-$ angle, Φ, (b) in neat [C4mim][Cl] IL and its mixtures with water for $R(\mathrm{H4}\cdots\mathrm{Cl}^-) \leq 4.0$ Å and $R(\mathrm{H5}\cdots\mathrm{Cl}^-) \leq 4.0$ Å, respectively.

distribution of the C2-H2$\cdots$Cl$^-$ angle in Figure 14. However, the most probable C4-H4$\cdots$Cl$^-$ and C5-H5$\cdots$Cl$^-$ angles are found to be around 140 degrees in both cases, thus somewhat larger as compared to the most probable angle of the C2-H2$\cdots$Cl$^-$ hydrogen bond. Again, part of the anions are found to be situated on top of the C4-H4 and C5-H5 bonds, and linear hydrogen bonds are rare. The distribution of the C5-C4-H4$\cdots$Cl$^-$ and C4-C5-H5$\cdots$Cl$^-$ dihedral angles illustrated in Figure 18, respectively, show pronounced maxima at $\pm$120 deg just as seen for the distribution of the N1-C2-H2$\cdots$Cl$^-$ dihedral angle in Figure 15, indicating that the chloride anions are located either on the butyl or the methyl side with equal probabilities. In addition, the probabilities for the anions to be located in the plain of the imidazolium ring are higher in these cases as compared to the corresponding case where anions are found in vicinity of the C2-H2 bond. The distributions seen in Figure 18 are rather different in the range of -90 to +90 degrees as compared to that shown in Figure 15. They suggest that chloride anions are also often found in the area between C4-H4 and C5-H5 bonds, and they prefer to be located roughly in the plain of the imidazolium ring in this case.

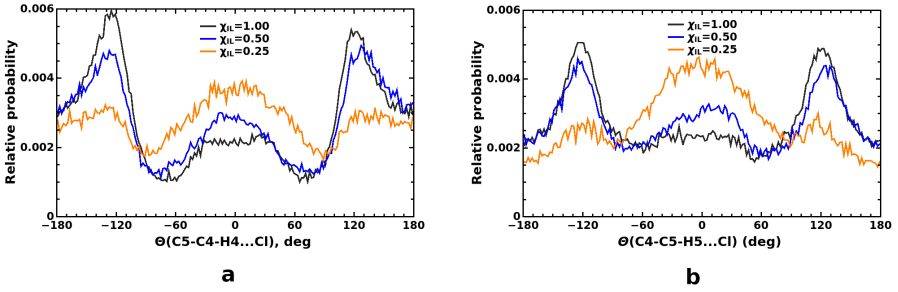

Figure 18: Distribution of the C5-C4-H4$\cdots$Cl$^-$ dihedral angle, Θ, (a) and the C4-C5-H5$\cdots$Cl$^-$ dihedral angle, Θ, (b) in neat [C4mim][Cl] IL and its mixtures with water for $R(\mathrm{H4}\cdots\mathrm{Cl}^-) \leq 4.0$ Å and $R(\mathrm{H5}\cdots\mathrm{Cl}^-) \leq 4.0$ Å, respectively.

The structural features of neat [C4mim][Cl] IL discussed above will definitely shape its ^{1}H NMR spectrum. The calculated NMR chemical shift of in particular H2 can differ by as much as 8-9 ppm between in-plane and on-top of the C2-H2 bond complexes of the isolated geometry-optimized ion pair of imidazolium cation and chloride anion.[107,183] Therefore, a molecular trajectory of neat [C4mim][Cl] IL was constructed which is composed of 100 snapshots dumped at regular intervals of 50 ps during production run of MD simulations in the NVT ensemble. A single C4mim$^+$ cation was selected in each

snapshot randomly to be considered as a central cation in the QM/MM calculations of ^{1}H NMR isotropic shielding constants. A spherical cut-off radius of 30 Å centered at the center of mass of the central cation was applied for every configuration, and thus around 830 ions were considered in each QM/MM calculation.

3.2.2 ^{1}H NMR Results

The QM/MM results for the ^{1}H NMR isotropic shielding constants in neat [C4mim][Cl] IL are collected in Table A1 in the Appendix. According to the most basic computational scheme, only the central cation is treated at the DFT level in every configuration while all other ions are represented by the point-charge potential. To evaluate the direct effect of the environment on the shielding constants of the C4mim$^+$ cation, calculations on the isolated central cation were also performed, that is, with all other ions removed. As seen in Table A1, the direct effect of the environment represented by point charges is to reduce the shielding constants of protons in imidazolium ring by 0.3-0.4 ppm. Meanwhile, the effect on the shieldings of hydrogen atoms in the methyl and butyl groups is smaller and practically does not exceed 0.2 ppm. It is known that non-electrostatic effects on the NMR properties of molecules involved in hydrogen bonding are typically important.[151,180,198] Therefore, the QM/MM calculations were performed when three additional ions were promoted to the QM region of the model, those which are closest to the H2, H4 and H5 atoms of imidazolium. As seen in Table A1, this improvement leads to further reduction of the shielding constants of H2, H4 and H5 atoms by as much as 0.4-0.5 ppm as compared to the case where the environment is kept classical entirely.

Further expansion of the QM region around the central cation is necessary to obtain a converged effect. Unfortunately, this implies a much increased computational burden. However, it was very recently reported that satisfactory results for the ^{1}H NMR shielding constants of [C4mim][Cl] IL can be obtained if modest 3-21G basis set is used for the ions around the central cation.[109] Therefore, the QM/MM calculations were repeated by keeping the def2-TZVP basis set for the central cation and switching to the 3-21G basis for the same three ions around the acidic hydrogens of the imidazolium ring as in previous calculations. Despite the reduced flexibility in the description of the electronic density of the additional ions, the results are virtually identical not only for the statistically-averaged shieldings as can be seen in Table A1 but rather astonishingly also for the shielding constants in all individual configurations as

well. However, it was observed that this effect is clearly due to the furtuitous cancellation of errors. As improving the 3-21G basis set by the diffuse functions leads to larger discrepancies for shieldings of atoms H2, H4 and H5 as compared to the case where def2-TZVP basis was used for all ions in the QM region of the model, see Table A1.

The QM region was further expanded by including 3 ions closest to the H2 atom and 2 ions closest to both the H4 and H5 atoms, thus 7 additional ions in total. For further QM/MM calculations the 3-21G basis set was used for all additional ions around the central cation. Compared to the previous QM/MM results in Table A1, further reduction of the shielding constants of atoms H2, H4 and H5 is observed. To calculate the ^{1}H NMR spectrum of neat [C4mim][Cl] IL consistenly, a series of QM/MM calculations were performed where entire first solvation shell of the C4mim$^+$ cation is treated quantum mechanically. To achieve this, all ions with at least one atom that has a distance not larger than 4 Å from atoms H2, H4 or H5, or from carbon atoms at positions 6, 8, 9 or 10 were included to the QM region. The amount of cations and anions thus promoted to the QM region are in the ranges of 9-14 and 3-7, respectively, with averaged numbers being, respectively, 11.1 and 4.9. Within the 4 Å sphere centered specifically at atom H2, one or two anions were always found, and the average number is 1.46 anions. The latter value compares excellently with the coordination number of chloride anions around the atom H2 of 1.47. The averaged number of anions coordinating both atoms H4 and H5 is 2.24, and in most cases 2 or 3 anions are included to the QM region on this end of the imidazolium ring.

As seen in Table A1, the results of these large-scale QM/MM calculations suggest that shielding constants of hydrogen atoms H2, H4 and H5 are practically converged with respect to the expansion of the QM region. The results showed that quantum mechanical treatment of ions around the methyl and butyl groups has rather small but notable and qualitatively different effect on the shielding constants of hydrogen atoms in these moieties. Compared to the case were the entire environment is treated classically, the shielding constants of hydrogens at positions 6, 7 and 8 are reduced by 0.36, 0.25 and 0.10 ppm, respectively, while those for hydrogens at position 9 and 10 are increased by 0.09 and 0.06 ppm. Also, the effect of ions beyond the first solvation shell on the shielding constants of the central cation was considered. This was achieved by repeating the large-scale calculations where first solvation shell is described quantum mechanically but all other ions are removed. Comparing the results

of these two large-scale models as given in Table A1, we deserve that the ^{1}H NMR spectrum of neat [C4mim][Cl] IL is indeed an essentially local property determined exclusively by the ions in the first solvation shell of the imidazolium cation.[109,199]

The comparison between the experimental and the predicted relative ^{1}H NMR spectra of neat [C4mim][Cl] IL is shown in Figure 19. In the Figure 19, the unit line is drawn to facilitate the comparison between calculated and measured chemical shifts: points above the unit line indicate overestimated chemical shift and *vice versa*. The calculated spectrum is based on the shielding con-

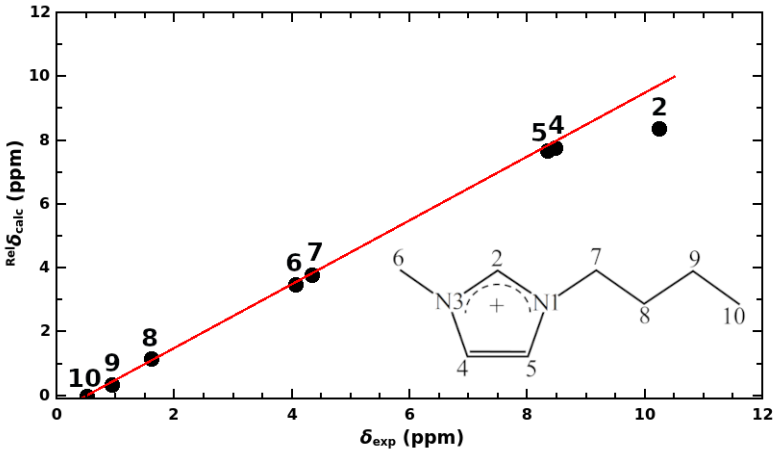

Figure 19: Calculated relative *vs* experimental ^{1}H NMR spectrum of neat [C4mim][Cl] IL at 298 K.

stants obtained by most extensive QM/MM calculations, and relative chemical shifts were evaluated with respect to the shielding constant of hydrogen atoms at position 10 in the imidazolium cation.[54] As seen in Figure 19, the agreement between calculated and experimental spectra of neat IL is very good in both qualitative and quantitative terms. Even the tight spacing of 0.1 ppm between the signals of atoms H4 and H5 is reproduced correctly. This is not the case if the effect of the ions beyond the first solvation shell were neglected, as seen in Table A1. However, the model is found to underestimate the chemical shift of the H2 atom by a substantial 1.4 ppm. Considering the high quantitative accuracy for all other NMR signals delivered by the present QM/MM model and the high sensitivity of the H2 chemical shift on the location of the H2 atom coordinating chloride anion with respect to the C2-H2 bond, it can be assumed that this discrepancy may be caused by incorrect angular distribu-

tion of the chloride anions around C2-H2 moiety. Apparently, this distribution should be shifted more towards higher values of the angle, and thus to more linear C2-H2$\cdots$Cl$^-$ hydrogen bonds. The results revealed that a refinement of the force field used in present MD simulations of neat IL may be necessary in order to improve the local distribution of ions around the C2-H2 moiety of imidazolium cations.

3.3 MIXTURES OF [C4MIM][CL] AND WATER

3.3.1 Structural analysis

In the case of the mixtures of [C4mim][Cl] and water, RDFs shown in Figures 11 and 13 suggest that small water admixture of $\chi_{\mathrm{w}} = 0.05$ has negligible effect on the local distribution of anions around the imidazolium ring. At this low content of water in the mixture, isolated water molecules are scattered across the simulation box, and they are found to form prolific hydrogen bonding interactions with chloride anions. This is signified by two pronounced peaks in the range of 1.7 to 4.0 Å in the RDF between hydrogen atoms of water and chloride anions in Figure 20. It was found that water molecules act as

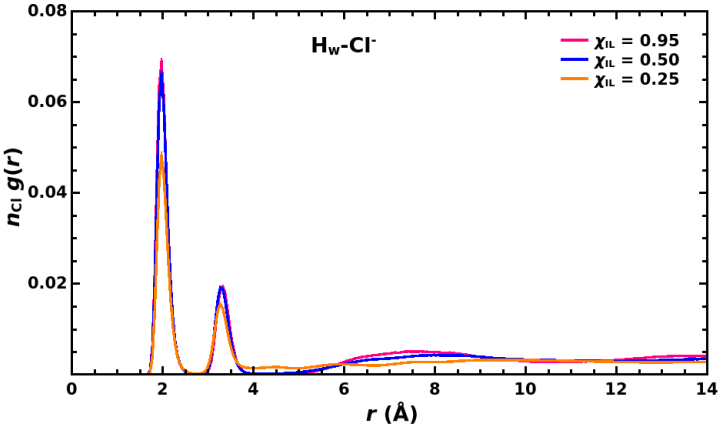

Figure 20: RDFs between hydrogen atoms of water and Cl$^-$ ions in neat [C4mim][Cl] IL and its mixtures with water, scaled by the number density of the chloride anions, n_{Cl}, for each specific system.

hydrogen-bonded links between chloride anions as also seen in previous MD simulations of mixtures of other imidazolium ILs and water.[74,76,187]

As also evident from Figure 20, the shape of this RDF stays virtually the

same when molar fraction of the IL drops to 0.50. Spherical integration of the first peak in these RDFs indicates that O-H bonds in water molecules form on average 1.00 and 0.98 hydrogen bonds with chloride anions when molar fraction of the IL is equal to 0.95 and 0.50, respectively. Visual inspection of the recorded trajectory for the mixture with $\chi_{\mathrm{IL}} = 0.50$ reveals a very characteristic structural pattern for water-anionic aggregates where typically two water molecules share two chloride anions simultaneously in the planar arrangament as illustrated in Figure 21a and corroborated by the SDF of Cl^- anions around the water molecules shown in Figure 21b. Furthermore, these aggre-

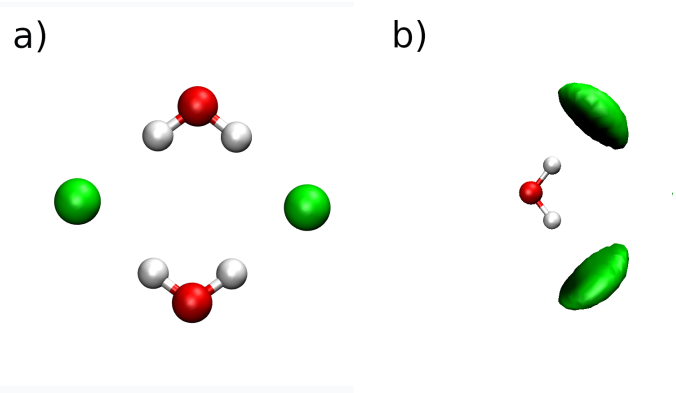

Figure 21: The structure of a typical aggregate between Cl^- anions and water molecules (a) and SDF of Cl^- anions around the water molecules in the mixtures with χ_{IL} of 0.50 and 0.25.

gates are also seen to conglomerate into longer polymer-like chains which are situated in the areas in-between the cations. The interactions between anions and water molecules are favoured so much that hydrogen bonding between water molecules is virtually absent. This is also suggested by the low intensity of the peak in the range of 1.6 to 2.3 Å in the RDF between hydrogen and oxygen atoms of water shown in Figure 22 for $\chi_{\mathrm{IL}} = 0.50$. The proliferation of water-anionic aggregates is accompanied by simultaneous exchange of anions by water molecules in the vicinity of the imidazolium ring as evident from the RDFs shown in Figures 11 and 13. This effect is also corroborated by the considerably increased intensity of the first peak in the RDF between H2 and oxygen atoms of water molecules shown in Figure 23 when χ_{IL} decreases from 0.95 to 0.50.

When molar fraction of water rises to 0.75, extensive chains of water-anionic hydrogen-bonded aggregates of the type $\cdots Cl^- \cdots (H\text{-}O\text{-}H)_n \cdots Cl^- \cdots (H\text{-}O\text{-}H)_m \cdots$ with n and m equal to 1, 2 or 3 are observed.

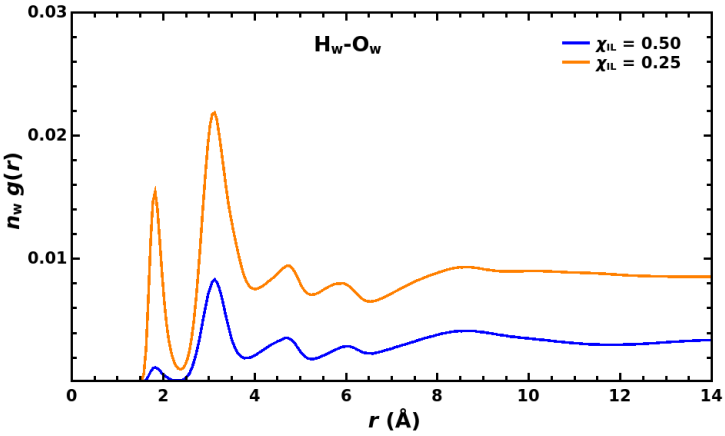

Figure 22: RDFs between hydrogen and oxygen atoms of water mixtures of [C4mim][Cl] and water, scaled by the number density of water, n_{w}, for each specific system.

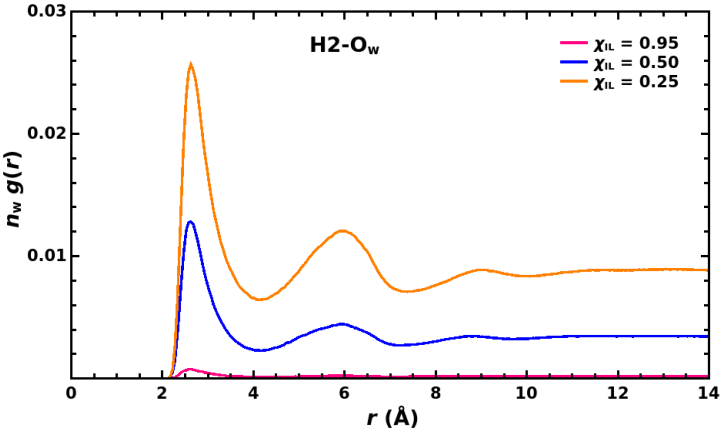

Figure 23: RDFs between H2 atom of C4mim^{+} cation and oxygen atom of water, scaled by the number density of water, n_{w}, for each specific system.

These aggregates are seen to surround aggregates of C4mim$^+$ cations, leading to strongly heterogeneous structure of the mixture.[16] Indeed, the RDFs between C10 atoms of imidazolium cations shown in Figure 24 reveal that aggregation of the butyl moieties of C4mim$^+$ is stimulated by the rising content of water in the mixture. Hydrogen bonding between water molecules is now also observed evidently, as the coordination number of Cl^- anions around O-H bonds of water molecules drops to 0.75 in the mixture with $\chi_{IL} = 0.25$. At the same time, the peak around 1.8 Å in the RDF shown in Figure 22 is seen to gain substantial intensity when molar fraction of water increases to 0.75.

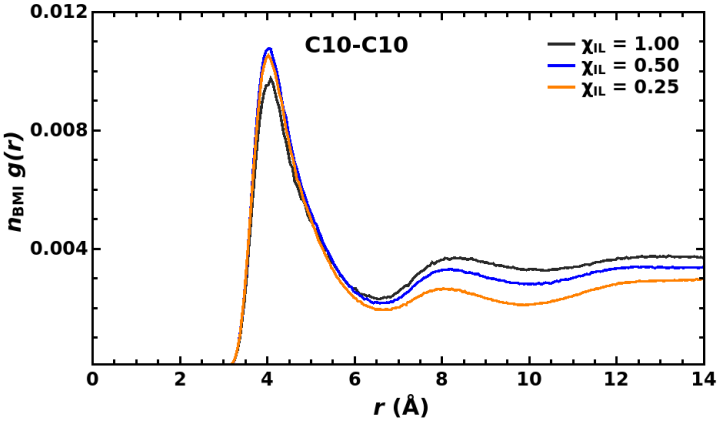

Figure 24: RDFs between C10 atoms of C4mim$^+$ cations in neat [C4mim][Cl] IL and its mixtures with water, scaled by the number density of imidazolium cations, n_{BMI}, for each specific system.

As evident from RDFs shown in Figures 11, 23 and 13, the exchange between chloride anions and water molecules around the imidazolium ring is intensified by the rising molar fraction of water in the mixture. The coordination number of chloride anions around the C2-H2 moiety drops from 1.47 in neat IL to 1.37 and 1.14 in mixtures with χ_{IL} of 0.50 and 0.25, respectively. The RDFs between H2 atoms of the imidazolium cations and oxygen atoms of water molecules in the simulated mixtures shown in Figure 23 support this finding. Spherical integration of the first peak in these RDFs up to 4 Å give the coordination number of 1.21 and 2.73 in systems with χ_{IL} of 0.50 and 0.25, respectively. Noteworthy, water molecules are found to approach the C2-H2 moiety of C4mim$^+$ cations already in the mixture of $\chi_{IL} = 0.95$ where the coordination number of oxygen atoms of water molecules by the H2 atoms was integrated to be as high as 1.74. Water molecules are thus indeed seen

to effectively screen electrostatic interactions between cations and anions in the mixture. Indeed, the SDF of oxygen atoms of water molecules around the C4mim$^+$ cation shown in Figure 25 indicates that water molecules tend to replace the anions in the vicinity of the imidazolium ring. Interestingly, water molecules and chloride anions show preference to virtually occupy the same areas around the imidazolium ring, compare SDFs shown in Figures 16 and 25.

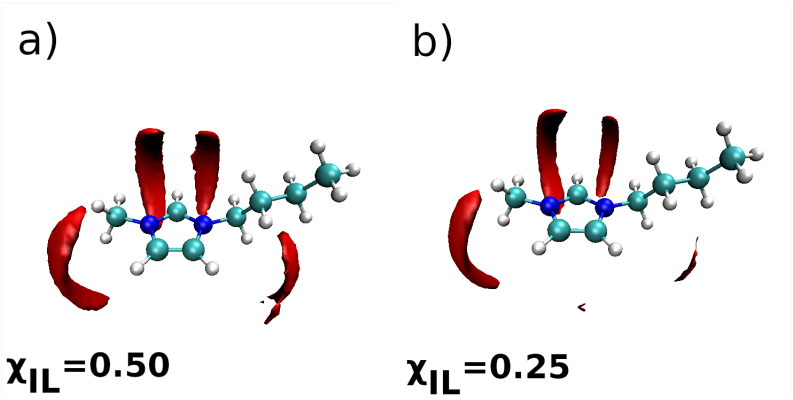

Figure 25: SDF of oxygen atoms of water molecules around the imidazolium ring of the C4mim$^+$ cation in the mixtures with χ_{IL} of (a) 0.50 and (b) 0.25.

Water is also found to affect structural distribution of anions around the C-H bonds in the imidazolium ring. As illustrated in Figure 14, a clear trend for the distribution of angles between C2-H2 bond and chloride anions to shift to higher values is observed with increasing content of water. Interestingly, chloride anions show increased tendency to also be located in the plane of the imidazolium ring in these mixtures as pronounced peaks around $\pm$120 deg in the distribution of the N1-C2-H2$\cdots$Cl$^-$ dihedral angle shown in Figure 15 decrease. While the distribution rises in the areas around 0 and 180 deg. These structural changes are clearly visible in the SDF of Cl$^-$ around the imidazolium ring calculated for the IL/water mixtures as shown in Figure 16, parts b and c. On the contrary, the angular distributions of chloride anions around the C4-H4 and C5-H5 bonds shown in Figure 17 are less sensitive to the molar fraction of water. However, the dihedral angle distributions shown in Figure 18 indicate the increasing preference for the chloride anions to stay in the region in-between the C4-H4 and C5-H5 moieties with the rising content of water in the mixture. The populations of anions on the methyl and butyl sides are decreased, especially in the system with $\chi_{\mathrm{IL}} = 0.25$.

3.3.2 ^{1}H NMR results

Heterogeneous nature of the three-component mixture between [C4mim][Cl] IL and water as well as slow dynamics of the ions and water molecules at ambient conditions implies complex chemical equilibrium in these systems. Therefore, the computational scheme was applied to calculations of NMR shieldings for specific types of water-ionic aggregates, and computational results are expected to be of suffcient quality in order to provide well-motivated rationalizations of the experimental data shown in Figure 10.

3.3.2.1 NMR shielding constant of the H2 atom of C4mim$^+$ cation

The QM/MM results for the ^{1}H NMR shielding constants of the H2 atom of C4mim$^+$ cation computed for the neat [C4mim][Cl] IL and for its mixtures with water are collected in Table 6. Distinct series of QM/MM calculations have been assigned an ID which are listed in second column in Table 6. The shielding constants provided in Table 6 are computed as time-averages over 100 molecular configurations. Statistical errors are evaluated as standard deviations of the sample and are provided in parentheses. Columns 3 to 6 give statistical information concerning the nature and amount of different species found around atom H2 of the central cation within the distance of 4 Å. The visualization of quantum mechanically treated subsystems in series **A** to **G** are showed in Figure 26.

As evident from Table 6, the value of the computed ^{1}H NMR shielding constant of the H2 atom in the imidazolium cation varies in the range of about 1 ppm depending on the structure of the local environment around the C2-H2 bond. However, coordination by chloride anions seems to be the major factor determining the value of the shielding constant. For both mixtures, the shielding constants computed for systems **B**, **C**, **E** and **F** with average number of chloride anions in the range of about 1 to 2 lead to rather similar values for the shielding constants. The computed shielding constants of the H2 atom are still larger in the mixtures than in the neat IL even in those cases where the average number of chlorides is larger than in the neat [C4mim][Cl]. These results are in line with the observed decrease of the chemical shift of the H2 atom with the increasing content of water in the mixture as illustrated in Figure 10b. In systems **D** and **G** with low average number of chloride anions near the C2-H2 moiety, a substantial increase in the shielding constants by as much as 1.3

Table 6: Calculated ^{1}H NMR isotropic shielding constants of the H2 atom of C4mim$^+$ cations, σ in ppm, in neat [C4mim][Cl] IL and its mixtures with water.

χ_{IL}	ID	Species around the H2 atom				σ
		Species	Min	Max	Aver.	
1.00	**A**	Cl^-	1	2	1.46	22.53 (0.09)
		C4mim$^+$	2	6	3.19	
0.50	**B**	Cl^-	1	2	1.20	22.69 (0.05)
		C4mim$^+$	0	3	0.83	
		H_2O	3	6	4.43	
	C	Cl^-	0	3	2.04	22.92 (0.05)
		C4mim$^+$	0	3	1.39	
		H_2O	2	5	3.94	
	D	Cl^-	0	2	0.23	23.77 (0.08)
		C4mim$^+$	1	5	2.51	
		H_2O	1	3	1.39	
0.25	**E**	Cl^-	0	1	0.99	23.00 (0.05)
		C4mim$^+$	0	4	1.47	
		H_2O	2	6	4.57	
	F	Cl^-	1	2	1.84	23.14 (0.06)
		C4mim$^+$	0	4	1.33	
		H_2O	2	7	4.65	
	G	Cl^-	0	1	0.01	23.80 (0.08)
		C4mim$^+$	0	3	1.45	
		H_2O	1	3	1.84	

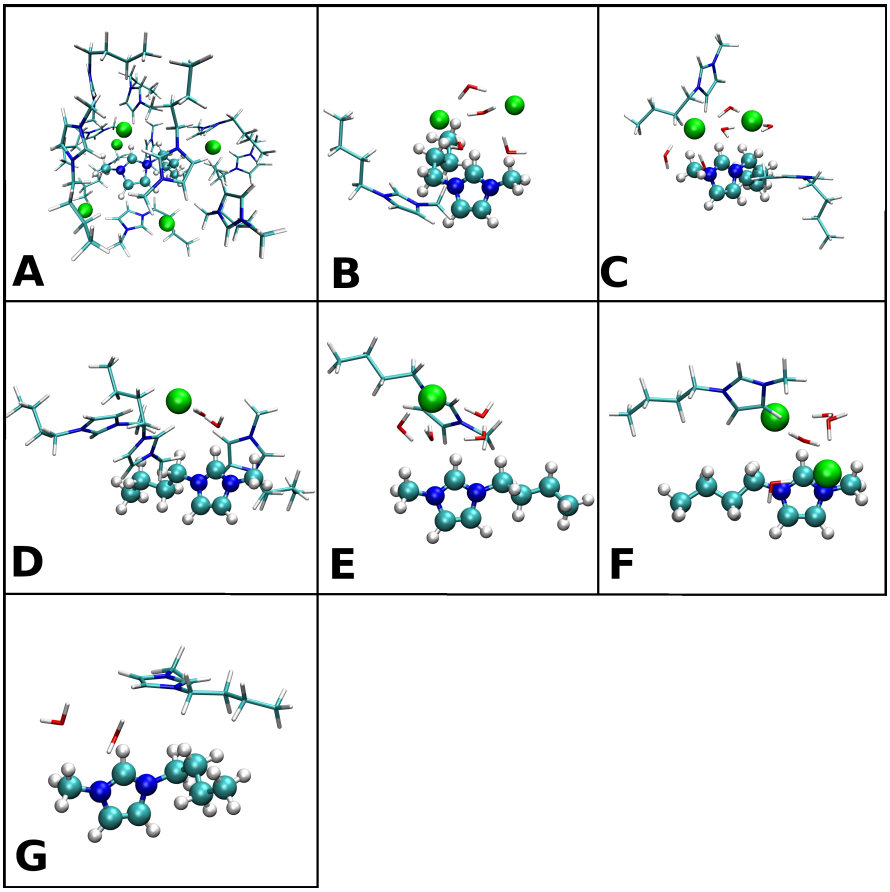

Figure 26: Visualization of a QM region in the QM/MM calculations for systems **A** to **G**. Central C4mim$^+$ cation is represented by the ball-and-stick model. Additional species included to the QM region around the central cation are represented by the stick model, except for chloride anions which are represented as green balls. Ions and water molecules described by the point charges in the QM/MM calculations are not shown. Note that the geometry of each system is taken from a single randomly selected configuration; the structure and composition of the quantum mechanically treated region changes from configuration to configuration in each specific system.

ppm is predicted as compared to the value computed for the neat IL, system **A**. These results are in line with previous observations mentioned in chapter 3 that the presence or the absence of the hydrogen bonding between C2-H2 group and the chloride anion is the main factor determining the shielding constant of the H2 atom in the imidazolium cation in liquid phase. The computational results showed that the observed monotonically decreasing chemical shift of the H2 atom with the increasing content of water in the mixture as illustrated Figure 10b is due to the gradual breakdown of the hydrogen bonding between the C2-H2 moiety of imidazolium cations and chloride anions. Notably, imidazolium chloride ILs are known to eventually dissociate into free fully solvated ions at the conditions of infinite dilution in an aqueous solution as was confirmed by results in chapter 3.

3.3.2.2 NMR shielding constants of water

The QM/MM results for the ^{1}H NMR shielding constants of water molecules in the mixtures of [C4mim][Cl] IL and water as well as in liquid water are presented in Table 7. First, a series of test calculations were performed which have led to a clear conclusion that the previously used cost-effective strategy to utilize a small 3-21G basis set for the quantum mechanically described environment of the C4mim$^+$ cation is not valid for the computations of the shielding constants of water molecules in the IL matrix, and the electronic structure of the entire QM region has to be described on an equal footing by using the same def2-TZVP basis set. In line with the high viscosity of the [C4mim][Cl] IL, it was observed that tumbling of the water molecules is hindered completely in the mixtures. Therefore, a statistical averages of the ^{1}H NMR shielding constants are provided for each hydrogen atom of the water molecule separately in Table 7.

The shielding constants provided in Table 7 are computed as time-averages over 100 molecular configurations. Statistical errors are evaluated as standard deviations of the sample and are provided in parentheses. In the case of the IL/water mixtures, shielding constants have been calculated for each proton of water molecule separately, designating the individual protons and corresponding shielding contants as H_a and H_b, and σ_a and σ_b, respectively. Column 2 contains information concerning the nature and amount of different species included to the QM region which are closest to each atom of the central water molecule. The visualization of quantum mechanically treated subsystems in series **H** to **M** are showed in Figure 27. The evolution of the ^{1}H NMR chem-

Table 7: Calculated ^{1}H NMR isotropic shielding constants of water molecules, σ in ppm, in pure water and its mixtures with [C4mim][Cl] IL.

χ_w	ID	Species around H_2O	σ_a	σ_b
0.05	**H**	H_a: 1 Cl^-; H_b: 1 Cl^-; O: none	26.44 (0.10)	26.84 (0.11)
		H_a: 1 Cl^-; H_b: 1 Cl^-; O: 2 C4mim$^+$	25.79 (0.11)	26.15 (0.11)
	I	H_a: 1 Cl^-; H_b: 1 Cl^-; O: 2 C4mim$^+$	27.17 (0.12)	26.66 (0.11)
0.50	**J**	H_a: 1 H_2O; H_b: 1 Cl^-; O: 2 C4mim$^+$	27.82 (0.11)	27.21 (0.11)
0.75	**K**	H_a: 1 H_2O; H_b: 1 H_2O; O: 2 C4mim$^+$	28.67 (0.12)	28.54 (0.10)
	L	H_a: 1 $_2O$; H_b: 1 H_2O; O: 1 H_2O, 1 C4mim$^+$	28.00 (0.10)	28.84 (0.12)
1.00	**M**	H_a: 3 H_2O; H_b: 3 H_2O; O: 4 H_2O	28.20 (0.09)	

ical shift of water with the changing composition of the mixture is referenced against the shielding constant of pure water. The ^{1}H NMR shielding constant of pure water was calculated as an average over 100 molecular snapshots, and 10 additional water molecules closest to the randomly selected central water molecule were included to the QM region in each snapshot. Present approach to obtain the value for the ^{1}H NMR shielding constant of pure water follows closely the computational scheme implemented in ref[123] where very accurate predictions of both ^{1}H and ^{17}O NMR shielding constants of pure water were obtained. The calculated value of the ^{1}H NMR shielding constant of pure water is marked as system **M** in Table 7.

In the case of the mixture with $\chi_{IL} = 0.95$, two series of QM/MM calculations were performed on a randomly selected water molecule, system **H**. In the first series, the two chloride anions forming hydrogen bonding to both the O-H bonds of the central water molecule were considered at the QM level. In the second series the QM region was further expanded to include also two C4mim$^+$ cations nearest to the oxygen atom site of the water molecule. As can be seen in Table 7, the effect of the quantum mechanical treatment of the ions in the immediate vicinity of the water molecule is mandatory to obtain correct values of the ^{1}H NMR shielding of water in the IL. In all subsequent calculations on water molecules in the IL-water mixtures, 1 closest species to each of the protons of the water molecule as well as two closest species to its oxygen atom were included to the QM region of the model. Also, the QM/MM calculations were performed on another randomly selected water molecule using the same computational scheme, system **I**. As evident from Table 7, the time-averages of the shielding constants for each proton in the same water molecule differ by as much as 0.5-0.7 ppm. This is a consequence of hindered rotation

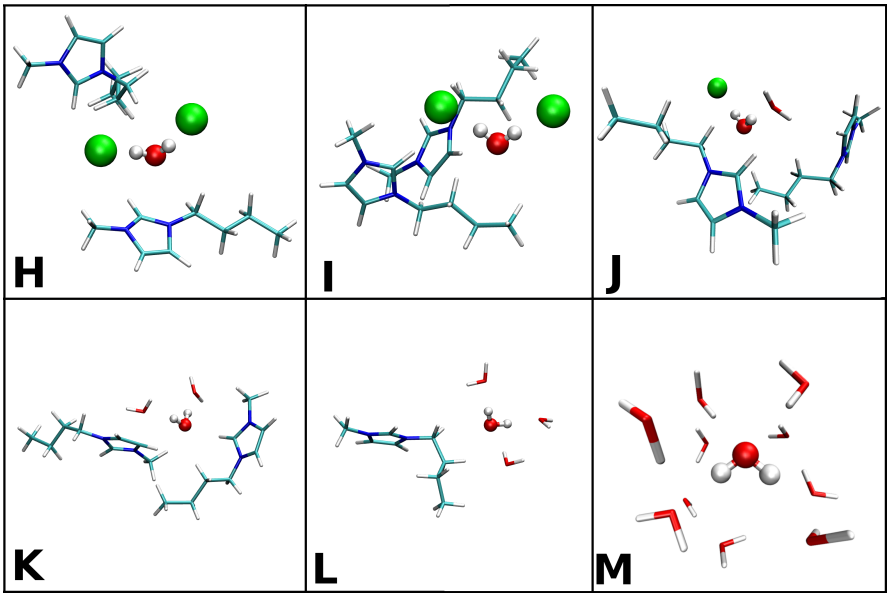

Figure 27: Visualization of a QM region in the QM/MM calculations for systems **H** to **M**. Central water molecule is represented by the ball-and-stick model. Additional species included to the QM region around the central water molecule are represented by the stick model, except for the chloride anions which are represented as green balls. Ions and water molecules described by the point charges in the QM/MM calculations are not shown. Note that the geometry of each system is taken from a single randomly selected configuration; the structure of the quantum mechanically treated region changes from configuration to configuration in each specific system.

of water molecules which is in turn caused by the strong hydrogen bonding interactions between water molecules Cl^- anions, as well as of local strongly anisotropic environment of the two O-H bonds of the water molecules. The results showed that ^{1}H NMR shieldings of the two water molecules **H** and **I** are rather different. This is caused by the difference in the local environment of the two water molecules as in the case of system **H** the two quantum mechanically treated cations are found to form hydrogen bonds with the water molecule through their C2-H2 moieties, whereas in system **I**, the C5-H5 bond of the first and the butyl group of the second imidazolium cation are found to coordinate the water molecule, see Figure 27.

Comparing to the shielding constant computed for liquid water, system **M**, both water molecules in the mixture with $\chi_{\mathrm{IL}} = 0.95$ display substantially lower values for their ^{1}H NMR shielding constants, thereby, implying larger chemical shifts for water molecules in the mixture than in pure liquid water. This result allows concluding that the rising curve of the chemical shift of water observed in Figure 10a when molar fraction of water streams to zero is due to the rising relative population of water molecules which form hydrogen bonding with the chloride anions. As discussed above, water molecules still form prolific aggregates with the chloride anions in the equimolar mixture of [C4mim][Cl] IL and water, and hydrogen bonding between water molecules is rather scarce in this system. Therefore, QM/MM calculations were performed for the water molecule where the two O-H bonds form hydrogen bonding with another water molecule and with chloride anion, system **J**. The result of the shielding constant computed for the hydrogen atom of the water molecule which is involved in hydrogen bonding with another water molecule is larger than of that which are involved in the hydrogen bonding with the anion. However, that shielding constant is still smaller than the corresponding value calculated for liquid water. This implies larger ^{1}H NMR chemical shift of water molecule in the mixture than in pure water, thus in contradiction to the experimental data seen in Figure 10a.

Turning to the mixture with largest content of water, $\chi_{\mathrm{w}} = 0.75$, QM/MM calculations on water molecules were performed for systems **K** and **L**. Here, both water molecules form hydrogen bonds to other water molecules. In system **L**, central water molecule also acts as a hydrogen bond acceptor for the third water molecule. In system **K** two $C4mim^+$ cations are found to be closest to the oxygen atom of the central water molecule. Noteworthy, all water molecules found in the vicinity of the central water molecule form hydrogen

bonding with chloride anions. As seen in Table 7, the computed ^{1}H NMR shielding constants of water are substantially larger than that of liquid water in three cases out of four. The computational results proved that initial lowering of the chemical shift of water seen in Figure 10a has to be caused by the water molecules which are free from hydrogen bonding with chloride anions, and possibly are found in the second solvation shell of the chloride anions. It is worth mentioning that the minimum chemical shift of water was recorded for the mixture with $\chi_{\mathrm{IL}} = 0.34$, see Figure 10a. However, water-anionic aggregates are seen to strongly prevail over the hydrogen bonded aggregates of water molecules even in the simulated mixture of $\chi_{\mathrm{IL}} = 0.25$. The computational results leads to the conclusion that the force fields selected for the IL and water in the present work in MD simulations are favoring water–anionic interactions too much, thus adding to the previously raised concern that the present force field applied for the IL may not be able to describe a local interionic structure of the imidazolium ring properly.

3.4 CONCLUSIONS OF CHAPTER 3

- The computed relative ^{1}H NMR spectrum of neat [C4mim][Cl] IL is found to be in a very good qualitative and quantitative agreement with the experimental data.

- A discrepancy was observed between the calculated and experimental results at the chemical shift of the C4mim$^+$ H2 atom, which was underestimated by 1.4 ppm. This discrepancy may be related to the possible inaccurate local distribution of Cl^- anions around the C2-H2 fragment of C4mim$^+$ cations in the neat IL, which may be caused by force field deficiencies used in MD modeling.

- Computational results showed that the decreased chemical shift of water molecules in the [C4mim][Cl]/water mixtures as compared to the chemical shift of neat water is due to the water molecules which form hydrogen bonds to other water molecules and not to the hydrophilic Cl^- anions.

- Hydrogen-bonded aggregates between chloride anions and water molecules proliferate when molar fraction of water diminishes. The QM/MM calculations predict larger chemical shift of water in these aggregates as compared to that of neat water. Therefore, relative proliferation of these water–anionic aggregates leads to the increasing chemical shift of water when molar fraction of the IL in the mixture rises from 0.34 to 0.98.

- The computations also have demonstrated that the decreasing chemical shift of the H2 atom in the C4mim$^+$ cations observed with the rising molar fraction of water in the mixture is due to the gradual replacement of chloride anions by water molecules in the vicinity of the C2-H2 moiety.

Based on the results, the statement of thesis is formulated as follows: In mixtures of 1-butyl-3-methyl-imidazole chloride ionic liquid and water, there is an equilibrium between the water molecules which form hydrogen bonds with each other and the water molecules which form hydrogen bonds with chloride anions; as the molar fraction of the ionic liquid in the binary mixture increases, the equilibrium changes, the population of the first type of aggregates decreases and this results in the non-monotonic evolution of the chemical shift of water observed experimentally.

CHAPTER 4.
MOLECULAR AGGREGATION IN LIQUID ACETIC ACID

Acetic acid is considered as a simple organic acid and an important substance in chemistry and biochemistry. Molecular association and understanding the intermolecular structure of neat acetic acid is still a subject of the investigations. Different experimental techniques and computational methods were used to investigate the intermolecular structure of the acetic acid. However, different experimental techniques indicate that different types of the molecular aggregates of the acetic acid molecules are formed in liquid AA such as cyclic dimers, linear solid-state-like chains and cyclic trimers and linear chains of at least three AA molecules.[86–90,94] Molecular simulations generally show that both cyclic and linear aggregates are formed in liquid AA.[200,201]

Capabilities of nuclear magnetic resonance for clarifying the local structure of glacial AA is limited because different aggregation patterns cannot be resolved in the NMR spectra due to the fast chemical exchange. A very curious, non-monotonic evolution of the ^{1}H NMR signal of the acidic proton of AA, and also substituted AA, has been recorded upon dilution with an inert solvent, e.g. carbon tetrachloride or cyclohexane.[202–205] With the increasing mole fraction of the inert component, progressive deshielding of the acidic proton is observed in a linear fashion up to a mole fraction of AA of roughly 5-10%. Further dilution of AA leads to a sudden increase in the shielding of this particular proton, and thus a clear maximum in the chemical shift is observed. There is experimental evidence that this maximum in the chemical shift of the acidic proton is largely due to the cyclic dimer of AA molecules.[206,207] Quite clearly, the increased shielding of the acidic proton in neat AA with respect to that of the cyclic dimer in apolar solution by as much as 0.1–0.6 ppm reflects the shift of equilibrium between different association patterns of AA molecules with the changing concentration of the inert component.[205] It has been demonstrated rather evidently that a simple equilibrium between monomer and cyclic dimer cannot explain this complex behavior, and linear aggregates have to be

considered.[204]

The aim of this work is to dissect the types of molecular self–aggregation of AA molecules in glacial acetic acid which are responsible for the increased shielding of the acidic proton. To this end, the classical MD simulations were performed of both liquid AA and cyclic dimers of AA in cyclohexane at infinite dilution conditions. Classical MD simulations were conducted using two different potentials – GAFF and OPLS, because the structure of liquid AA can depend on the force field. Quantitative analysis of the trajectories were performed to identify the amounts of different types of AA molecular aggregates in the neat liquid, including cyclic dimers and solid-state-like chain aggregates, but also other types of self-aggregates possessing considerable interaction energies.[201,208] The calculations of the ^{1}H NMR isotropic shielding constants were performed of the acidic proton by using a combined QM/MM approach along with a dynamic averaging scheme. One of the advantages of this computational scheme is that it will not only give a proper ensemble–average of the NMR shielding of the acidic proton in the liquid phase, but it will also allow evaluating the shielding of the proton in particular types of hydrogen bonded molecular aggregates, something that cannot be resolved by an ordinary NMR experiment.

4.1 COMPUTATIONAL DETAILS

4.1.1 Classical MD simulations

Rigid-body MD simulations in the NVT ensemble were performed using the molecular dynamics module of the Molsim program, v. 3.3.0.[209] Intermolecular interactions were modelled by the standard electrostatic Coulomb and a 12-6-type Lennard-Jones potential. Lennard-Jones parameters adopted to acetic acid and cyclohexane molecules have been taken from two families of classical force field – the optimized potential for liquid simulations, OPLS,[200,210] and the generalized Amber force field, GAFF.[163] Lorentz-Berthelot combining rules were applied to calculate the Lennard–Jones parameters for pairs of unlike atomic centers.

In this work, a *trans* conformation of C_s symmetry for acetic acid (AA) and a chair conformation of D_{3d} symmetry for cyclohexane molecules were considered. The *cis* conformation of acetic acid and twist-boat conformation of cyclohexane are omitted as they are too high in energy to form significant populations in the liquid state around room temperature.[211–213] Different methods

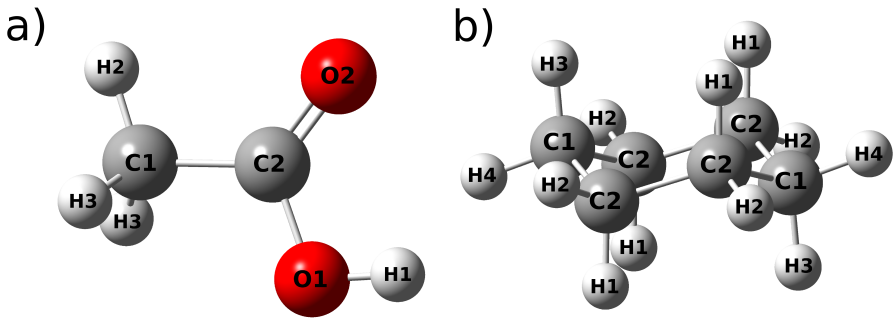

Figure 28: Atom labelling for acetic acid (a) and cyclohexane (b) molecules.

were applied to derive the geometries and point charges of the two molecules to be used along the OPLS and GAFF based Lennard–Jones parameters in the simulations. In the former case, molecular geometries were optimized at the density functional theory based B3LYP level[171] together with the Dunning's correlation consistent aug-cc-pVTZ basis set[172] and polarizable continuum model[181] to account for solvent effects. Atomic point charges were derived by fitting to the B3LYP/aug-cc-pVTZ/PCM based electrostatic potential according to the CHelpG scheme[182] imposing the constraint on the resulting dipole moment to match its DFT value. Molecular geometries and charges computed in the cyclohexane environment represented by PCM were used in the simulations of cyclohexane solutions of acetic acid cyclic dimer. In contrast, geometry and charges for the acetic acid molecules to be used in the simulation of neat liquid were derived using acetic acid as a solvent modelled by PCM. Gaussian 09 program[161] was utilized for geometry optimizations and CHelpG calculations, sticking to default parameters of PCM for the two considered solvents.

The point charges for acetic acid and for cyclohexane to be combined with the GAFF Lennard–Jones parameters were derived by using restrained electrostatic potential procedure[165] implemented in the Antechamber module[166] of Amber 12 program.[158] These point charges are based on the electrostatic potentials computed using Hartree-Fock approach along with the 6-31G* basis set[159,160] according to the Mertz-Kollman scheme[214] implemented in Gaussian 09. These calculations were carried out for the geometries of isolated molecules optimized at the HF/6-31G* level of theory. All force field parameters are presented in Table 8. The van der Waals parameters ε and σ are given in kJ mol^{-1} and Å, respectively. Atom labelling is presented in Figure 28.

Table 8: Force field parameters used in the MD simulations for acetic acid and cyclohexane molecules.

Atom	GAFF			OPLS			
	ε	σ	q	ε	σ	q_{chn}[a]	q_{aa}[b]
			Acetic acid				
C1	0.4577	3.40	-0.4646	0.2761	3.50	-0.2980	-0.3151
C2	0.3598	3.40	0.8811	0.4393	3.75	0.7914	0.8158
O1	0.8803	3.07	-0.6727	0.7113	3.00	-0.6083	-0.6201
O2	0.8786	2.96	-0.6192	0.8786	2.96	-0.6029	-0.6331
H1	0.0000	0.00	0.4511	0.0000	0.00	0.4150	0.4292
H2	0.0657	2.65	0.1414	0.1255	2.50	0.0882	0.0925
H3	0.0657	2.65	0.1414	0.1255	2.50	0.1073	0.1154
			Cyclohexane				
C1	0.4577	3.40	0.0354	0.2761	3.50	0.0575	
C2	0.4577	3.40	0.0354	0.2761	3.50	0.0591	
H1	0.0657	2.65	-0.0177	0.1255	2.50	-0.0257	
H2	0.0657	2.65	-0.0177	0.1255	2.50	-0.0330	
H3	0.0657	2.65	-0.0177	0.1255	2.50	-0.0261	
H4	0.0657	2.65	-0.0177	0.1255	2.50	-0.0322	

[a] – derived in cyclohexane solution modelled as PCM.

[b] – derived in acetic acid solution modelled as PCM.

Two systems have been simulated: an AA cyclic dimer in cyclohexane solution and neat AA using both OPLS and GAFF force fields. The first system was composed of an AA cyclic dimer along with 500 cyclohexane molecules. The second system of the neat acetic acid was represented by 800 AA molecules. In the simulations employing FF based on OPLS LJ parameters, the size of the cubic box was fixed to reproduce experimental density of neat liquid at 323 K and normal pressure – that is, 749.8 kg/m^3 for cyclohexane[215] and 1015.7 kg/m^3 for acetic acid.[216] In contrast, additional MD simulations were performed in the NPT ensemble using a force field based on GAFF Lennard–Jones parameters in order to obtain relaxed densities of both simulated systems. These rather standard simulations were conducted using Sander module of Amber 12 program,[158] following the lines as described in work[217] The size of the box in NVT simulations carried out using Molsim was adjusted according to the densities obtained from the simulations in the NPT ensemble.

All systems were simulated in the NVT ensemble using Berendsen thermostat[218] to control the temperature set to 323 K. Periodic boundary conditions

were employed, and electrostatic and Lennard–Jones interactions were cut off at half of the simulation box side. Equations of motion were integrated using velocity Verlet algorithm with a time step of 1 fs. To equilibrate the system, initial simulation of 400 ps was considered. The trajectory to be analyzed was recorded during the data production run of 1 ns.

4.1.2 QM/MM calculations

The QM/MM calculations of the ^{1}H NMR isotropic shielding constants have been carried out using the QM/MM module of the Dalton molecular electronic structure program,[178] release Dalton 2016.1. Gauge-including atomic orbitals have been employed to eliminate gauge-origin dependence of NMR shielding constants. The shielding constants have been computed using the KT3 exchange-correlation functional[175] along with the def2-TZVP basis set.[176] The KT3 functional was specifically designed to provide accurate NMR shielding constants and its potential for accurate prediction of liquid-phase NMR spectra were demonstrated in previous works.[152–154] The point charge based potentials were utilized to represent the classically described molecular subsystem. The point charges used for molecules in the MM region are the same as were used in our MD simulations employing the OPLS LJ parameters. These charges are thus listed in Table 8 under headings q_{chn} and q_{aa} for cyclohexane and acetic acid molecules, respectively. These charges were also used for systems simulated using GAFF based force fields because they describe the anisotropies of the electric potential created by the classical cyclohexane and AA molecules more accurately as compared to the charges derived using the RESP procedure.

Based on molecular trajectories obtained from the MD simulations, 4 sets of molecular configurations have been constructed for the QM/MM calculations of NMR shielding constants. Each set contains 100 configurations dumped at regular intervals of 10 ps. Every molecular configuration was processed by applying periodic boundary conditions so that the solute is translated to the center of the box. A spherical cut-off radius of 20 Å with the origin at the center of mass of the solute has subsequently been applied. Around 180 cyclohexane and around 350 acetic acid molecules along the solute are included to the QM/MM calculation. In most cases an additional AA molecule closest to the acidic proton of the central acetic acid was included to the quantum mechanically described region of the model. In this way, hydrogen bonding between the AA molecules are treated at the DFT level of theory. The liquid-

phase NMR isotropic shielding constant of the acidic hydrogen is evaluated as a statistical average over all molecular configurations and over all acidic hydrogens involved in hydrogen bonding where both the hydrogen bond donor and acceptor have been treated at the DFT level. As an example, in the liquid-phase shielding constant of the AA cyclic dimer in cyclohexane is an average over 200 entries.

Computed ^{1}H NMR isotropic shielding constants of acetic acid have been converted to chemical shifts with respect to the ^{1}H shielding constant of tetramethylsilane (TMS) equal to 31.95 ppm. This value was computed using the KT3/def2-TZVP method. The T_d geometry of TMS was optimized at the B3LYP/aug-cc-pVTZ/PCM level of theory using Gaussian 09. The calculated value for the ^{1}H NMR shielding constant of TMS appears to be the same for both geometries of TMS derived in acetic acid and cyclohexane. Test calculations showed that the effect of PCM on the computed shieldings of TMS is negligible.

4.2 STRUCTURAL ANALYSIS

Some of the intermolecular site-site radial distribution functions of liquid acetic acid simulated using GAFF and OPLS FFs are shown in Figure 29. As expected for a strongly self-associating liquid, these RDFs evidently confirm a pronounced local molecular ordering in the system. The sharp and tall first peaks in the RDFs illustrated in Figs. 29a and 29b suggest the abundance of the hydrogen bonding formed between the acidic proton and carbonyl oxygen. The most probable distance between H1 and O2 are found to be 1.69 and 1.76 Å based on simulations using OPLS and GAFF, respectively. The difference between the positions of the first maxima in the hydroxyl oxygen-carbonyl oxygen and acidic hydrogen-carbonyl oxygen RDFs is equal to 0.90 Å for both FF. Considering that the O-H bond length in acetic acid molecules is equal to 0.95 and 0.97 Å in the GAFF and OPLS based MD simulations, respectively, it was found that the hydrogen bond between the acidic hydrogen and carbonyl oxygen to statistically deviate from the ideal linear hydrogen bond configuration. Although, a pronounced peak in the range of 2.8 to 4.4 Å in the carbonyl oxygen-methyl carbon RDF shown in Fig. 29c indicates clearly that some hydrogen bonding between the carbonyl and methyl moieties is formed. The RDFs showed that linear solid-state-like aggregates are apparently formed in liquid AA. The intermolecular acidic hydrogen-hydroxyl

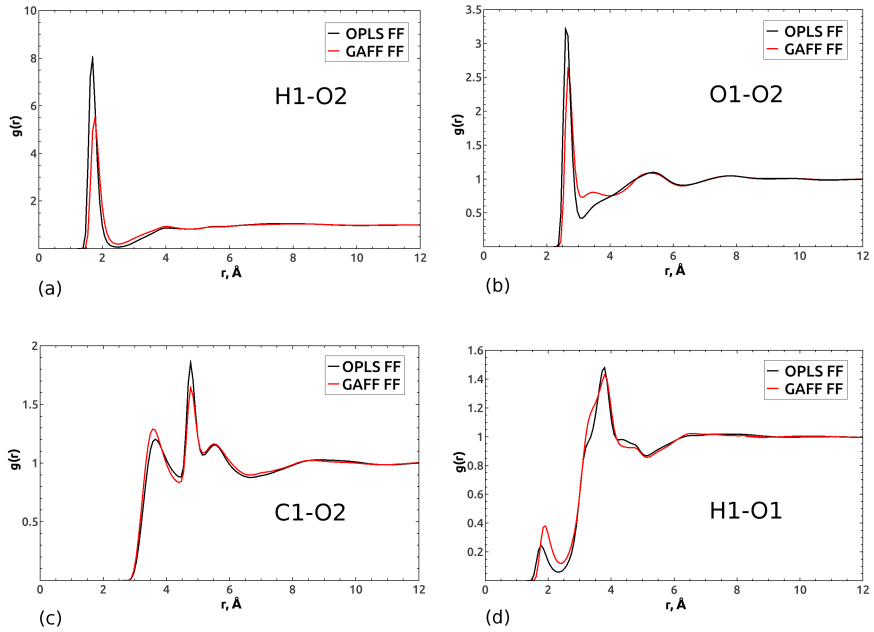

Figure 29: Intermolecular radial distribution functions of liquid AA at 323 K. See Fig. 28a for atom labelling.

oxygen RDF shows the formation of the hydrogen bond between the hydroxyl moieties of AA, see Fig. 29d, although apparently to a much lesser degree as compared to the dominating hydrogen bonding formed between the hydroxyl and carbonyl group. The results revealed that OPLS FF leads to shorter and more persistent hydrogen bonding between the acidic proton and the carbonyl oxygen as compared to GAFF. On the other hand, the hydrogen bonding between methyl group and carbonyl oxygen is slightly more pronounced in the case of GAFF, as is the hydrogen bonding between the hydroxyl groups.

The specifics regarding molecular association is not clear due to the statistically and spherically averaged RDFs. Therefore, a detailed analysis of molecular trajectories has been conducted aiming to dissect the types and abundances of different acetic acid hydrogen-bonded molecular aggregates formed in the neat liquid. Three types of hydrogen bond formed between any two AA molecules were considered including hydrogen bonds between acidic hydrogen and carbonyl or hydroxyl oxygen atoms as well as between methyl group and carbonyl oxygen. Keeping in mind a fair degree of arbitrariness regarding the definition of the hydrogen bond in computer simulation based analyses,[219,220] only the geometrical hydrogen bond definition will be used in

Table 9: Geometrical definition of the hydrogen bond of type D-H $\cdots$ A where D, H and A are the three atoms involved in the hydrogen bond with D and A denoting electronegative atoms in the donor and acceptor molecules, respectively.

Type	R(H/D $\cdots$ A)	$\angle$(H-A $\cdots$ D)
O1-H1 $\cdots$ O2	R(H1 $\cdots$ O2) $\leq$ 2.5 Å	$\angle$(H1-O1 $\cdots$ O2) $\leq 30^\circ$
O1-H1 $\cdots$ O1	R(H1 $\cdots$ O1) $\leq$ 2.4 Å	$\angle$(H1-O1 $\cdots$ O1) $\leq 30^\circ$
C1-H2/3 $\cdots$ O2	R(C1 $\cdots$ O2) $\leq$ 4.4 Å	$\angle$(H2/3-C1 $\cdots$ O2) $\leq 30^\circ$

this work. Specific geometrical criteria for all three types of hydrogen bond are listed in Table 9. Values for the cut-off distances of the hydrogen bonds are based on the position of the first minimum in the corresponding RDFs shown in Figs. 29a, c and d. Definitions of the hydrogen bond involving the hydroxyl group of AA are in fact very similar to those used in this work.[201]

Most of AA molecular aggregates which were considered are depicted in Figure 30. Specifically, in addition to the cyclic dimer **A** and the solid-state chain like dimeric unit **C**, other types of AA associates possessing considerable interaction energies were examined.[201,208,221] The higher order cyclic structures, in particular, cyclic trimers **B**, and cyclic aggregates up to and including hexamers were considered. Another important self-associate of AA molecules is dimer **D** which is similar to **C** but with the hydroxyl group of the donor forming the hydrogen bond to the hydroxyl rather than carbonyl oxygen of the acceptor. The dimer of type **E** is apparently stabilized by double hydrogen bonding between methyl groups and carbonyl oxygen atoms as well as by the anti-parallel configuration of the dipole moments. It has been proposed that dimers of type **F** having a high net dipole moment are prominently formed in AA solutions in protic polar solvents such as water or alcohol.[222,223]

The structural analysis was performed on two molecular trajectories obtained from GAFF and OPLS based simulations. The hydrogen bonds defining each aggregate are marked by dotted lines in Fig. 30. The statistical results are provided as averages over all the configurations in the trajectory.

Using the hydrogen bond definitions in Table 9, the analysis showed that on average 98.4 and 96.4% of AA molecules are involved in the hydrogen bonding between hydroxyl and carbonyl moieties either as a donor or as an acceptor in OPLS and GAFF based trajectories, respectively. The hydrogen bonding between hydroxyl groups is far less abundant, so that correspondingly only 9.0 and 16.4% of molecules are involved in this type of intermolecular interaction in OPLS and GAFF based simulations. In addition, it was investigated

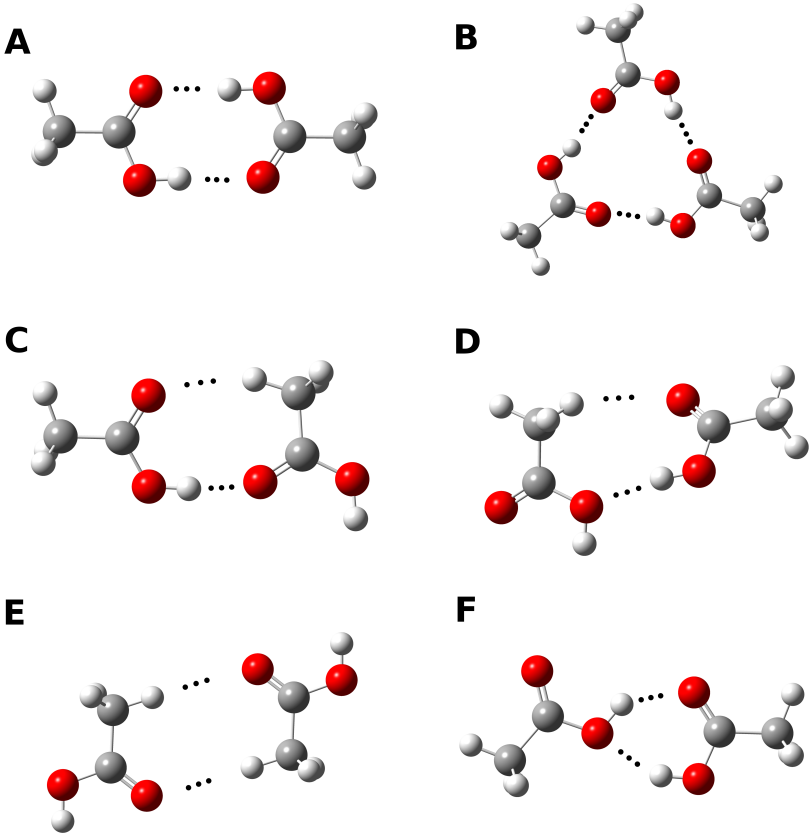

Figure 30: Molecular aggregates of hydrogen bonded AA molecules and their labelling.

Table 10: The molecules involved in various kinds of hydrogen-bonded associates in liquid acetic acid. Second column lists modifications to the hydrogen bond definitions given in Table 9.

Aggregate	Modif. to h. b. criteria	GAFF,%	OPLS,%
Cyclic dimer **A**		16.0	17.1
Cyclic trimer **B**		8.2	15.1
Cyclic tetramer		4.7	6.2
Cyclic pentamer		0.8	1.5
Cyclic hexamer		0.4	0.8
Chain-like aggregate **C**		5.4	4.4
	$\angle(\text{H2-C1}\cdots\text{O2}) \leq 50^\circ$	19.9	18.0
	$\angle(\text{H2-C1}\cdots\text{O2}) \leq 180^\circ$	37.2	33.4
Chain-like aggregate **D**		1.4	0.6
	$\angle(\text{H3-C1}\cdots\text{O2}) \leq 50^\circ$	6.1	3.3
	$\angle(\text{H3-C1}\cdots\text{O2}) \leq 180^\circ$	7.7	4.2
Dimer **E**		1.1	0.9
	$\angle(\text{H2-C1}\cdots\text{O2}) \leq 50^\circ$	4.4	3.4
Dimer **F**		0.0	0.0
	$\angle(\text{H1-O1}\cdots\text{O1}) \leq 50^\circ$	0.1	0.0

the amount of AA molecules the O-H group of which does not form hydrogen bond to neither the carbonyl nor the hydroxyl oxygen atom, and these amounts were found to be 3.5 and 5.9% for OPLS and GAFF based trajectories, respectively. It should be noted that the percentages discussed here are clearly non-additive as single AA molecule can be involved in several types of hydrogen bond simultaneously.[201]

A detailed analysis of molecular self-association in neat AA are collected in Table 10. The results showed that cyclic dimer **A** is not the dominating aggregation form of AA molecules in the liquid. However, a significant abundance of higher-order cyclic aggregates was found, and in particular cyclic trimers **B** are formed in substantial numbers, particularly in the OPLS based trajectory. In contrast to cyclic dimers and trimers, the cyclic tetramers and higher order cyclic aggregates are not planar and present folded configurations. This was noticed in previous MD simulations of liquid AA[224] and of AA in carbon tetrachloride solution.[225] As can be seen in Table 10, around 40 and 30% of AA molecules are involved in cyclic aggregates in OPLS and GAFF based trajectories, respectively.

As seen in Table 10, merely 4-5% of molecules are found to form solid-state like linear chain aggregates **C** using default O-H$\cdots$O and C-H$\cdots$O

hydrogen bond definitions given in Table 9. Visual inspection of these aggregates reveals the presence of dimeric units only, and thus chains composed of three or more monomers were not observed. Considering that simultaneous ideal linear hydrogen bond arrangement for both the O-H $\cdots$ O and C-H $\cdots$ O hydrogen bonds cannot be achieved in dimer **C** sterically, the adopted definition for the C-H $\cdots$ O hydrogen bond may be too severe here. Therefore, the analysis was repeated concerning the abundance of solid–state like linear aggregates by using a more relaxed threshold for the angle of the C-H $\cdots$ O hydrogen bond, keeping other criteria as defined in Table 10. In this way, a sensitivity of the results to the hydrogen bond definition is tested and also the softness of the C-H $\cdots$ O hydrogen bonds is taken into account.[226] As seen in Table 10, the abundance of this type of aggregate significantly increases even to 18–20% when the threshold for the C-H $\cdots$ O hydrogen bond angle is lifted to 50°. By removing the criterion for the angle at all and thus keeping only the criterion for the C-H $\cdots$ O hydrogen bond distance, we get an estimate of the upper limit for the concentration of the solid–state like linear aggregates in liquid AA. As seen in Table 10, the results concerning the concentration of these aggregates in liquid AA are very sensitive to the definition of the C-H $\cdots$ O hydrogen bond. The abundance of aggregate **D** is also dependent on the geometrical definition of the C-H $\cdots$ O hydrogen bond, but it is nevertheless low as compared to that of **C**. The same conclusion is valid for dimer of type **E**. The analysis suggested that AA dimer **F** is virtually non-existent in the neat liquid.

Comparing the results in terms of two force fields used in this work, the results show that OPLS FF favours cyclic structures more as compared to GAFF. The abundance of cyclic trimers is substantially higher using the OPLS FF. However, the abundance of cyclic dimer is found to be rather similar using both potentials. Considering the abundances of cyclic aggregates of AA molecules as mentioned above, at least 59 and 66% of molecules are involved in various types of linear aggregates in molecular trajectories based on OPLS and GAFF, respectively. The formation of linear chains is seen to be more prolific in the case of GAFF potential. The analysis showed that on average linear aggregates prevail over the cyclic ones. It means that the cyclic dimer is certainly not the dominating type of aggregation of AA molecules in the neat liquid. However, the amount of linear aggregates having the solid-state like chain arrangement depends very much on how the C-H $\cdots$ O hydrogen bond is defined geometrically. It was also noted that hydrogen bond cooperativity which is claimed

Table 11: The QM/MM results for the ^{1}H NMR isotropic shielding constants, σ_{iso}, and chemical shifts, δ, both in ppm, for the acidic proton of AA in liquid phase.

System	N	GAFF		OPLS		δ^{exp}
		σ_{iso}	δ	σ_{iso}	δ	
Cyclic dimer **A** in C_6H_{12}	200	23.17 (0.09)	8.78	21.91 (0.10)	10.04	12.10
Liquid AA	300	23.73 (0.08)	8.22	22.35 (0.08)	9.60	11.45
Cyclic dimer **A** in liq. AA	200			21.58 (0.09)	10.37	
Cyclic trimer **B** in liq. AA	300			21.89 (0.07)	10.06	
Aggregate **C** in liq. AA	100			22.02 (0.14)	9.93	
Aggregate **D** in liq. AA	100			23.41 (0.11)	8.54	
Monomer in liq. AA	100			25.06 (0.08)	6.89	

to be the driving force behind the stabilization of linear chains is due to the many-body polarization interactions.[227] These interactions are not accounted for by using pair-wise fixed-point-charge potentials in the MD simulations. Therefore, the content of these aggregates may be in fact underestimated by using these standard non-polarizable FFs.

It is worth noting that A cyclic dimer was always seen to remain intact in cyclohexane solution using either force field during the MD simulation. This effect was also observed in the MD simulation of AA cyclic dimer in liquid chloroform.[221] The hydrogen bond length in the cyclic dimer in cyclohexane was found to be the same as in the neat liquid as simulated using GAFF – that is, 1.76 Å. In the case of the OPLS FF, the charges for AA molecules in cyclohexane are smaller in magnitude as compared to those in neat AA, and thus the hydrogen bond length of AA cyclic dimer in cyclohexane of ca. 1.72 Å, is found to be slightly larger than in the neat liquid.

4.3 ^{1}H NMR CHEMICAL SHIFTS

The condensed-phase QM/MM results for the ^{1}H NMR isotropic shielding constants and chemical shifts of the acidic proton in acetic acid molecules are presented in Table 11.

The second column in Table 11 lists the number of entries, N, included in the averaging. The statistical errors for σ_{iso} are evaluated according to $s/\sqrt{N}$, where s is a corrected sample standard deviation, and are provided in parentheses. Chemical shifts are evaluated with respect to TMS. Experimental chemical shifts, δ^{exp}, are taken from Kimtys et al.[205] The result for neat liquid was obtained by considering three randomly selected AA molecules in each of the 100 configurations, so that the averaging is performed over 300 entries in this

case. As described in section of computational details, the shielding constants are averaged over those acidic protons which are involved in hydrogen bonding with both the hydrogen bond donor and acceptor described by the DFT approach.

In Table 11 a marked difference between the isotropic shielding constants computed for the GAFF and OPLS FF based trajectories is observed. A significant part of this difference originates from the different geometries of acetic acid molecules used in the MD simulation protocols utilizing the two potentials. In particular, the length of the O-H chemical bond is fixed at 0.95 and 0.97 Å in simulations using GAFF and OPLS FFs, respectively. The ^{1}H NMR isotropic shielding constants of the acidic proton in isolated AA molecules having the geometries as in GAFF and OPLS based simulations are computed to be 27.24 and 26.53 ppm, respectively. These calculations have been performed at the KT3/def2-TZVP level of theory using Dalton program. The lengthening of the O-H bond by ca. 0.02 Å thus leads to the deshielding of the acidic proton by ca. 0.7 ppm. Similarly, the lengthening of the chemical bond of the carbonyl moiety is known to lead to the pronounced deshielding of the ^{17}O nucleus.[151] The rest of the computed difference between the shielding constants for GAFF and OPLS based trajectories has to come from the difference in the distribution of the solvent molecules around the central quantum mechanically described AA molecule.

As seen from the results, a numerical agreement between the computed and experimental chemical shifts is unsatisfactory due to the combined systematic errors of exchange-correlation functional and basis set as well as inaccuracies in the molecular geometries and potentials used in both MD simulations and QM/MM calculations. However, the theoretical approach reproduces the observed decrease of the chemical shift of the acidic proton when going from the cyclic dimer in cyclohexane solution to the neat liquid. The computed increase in the shielding amounts to 0.56 and 0.44 ppm for the GAFF and OPLS based trajectories, and compares rather well to the corresponding experimental result of 0.65 ppm.[205] Even though cyclic dimer is a predominant form of AA aggregation in its low concentration solutions in inert solvents,[206,207] the chemical shift of 12.10 ppm observed at 10% mol. frac. of AA in cyclohexane at 323 K is admittedly due to the cyclic dimers, open dimers and monomers being in a dynamical equilibrium. The computational results for the shift of the ^{1}H NMR chemical shift of acidic proton in AA molecules going from low-concentration cyclohexane solution to the neat liquid should be seen as an

upper-bound estimate for the corresponding experimental shift as delivered by present computational approach.

To analyze underlying reasons behind the increased shielding of the acidic proton when going from acetic acid solution in cyclohexane to glacial AA, the QM/MM calculations. The ^{1}H NMR shieldings of the acidic proton have been performed for various types of AA molecular aggregates formed in the neat liquid. These calculations have been conducted on the molecular trajectory recorded during the MD simulation utilizing OPLS FF. The results presented in Table 11 show that the acidic protons of acetic acid molecules forming cyclic dimers are even more deshielded in the neat liquid than in cyclohexane solution. Therefore, a conclusion can be draw that cyclic dimer cannot be the dominating type of molecular aggregation in glacial acetic acid. Also, the calculations of the ^{1}H NMR isotropic shielding constants for acidic protons in cyclic trimers were performed. In these calculations, all three AA molecules forming the cyclic aggregate are treated at the DFT level, and remaining AA molecules are described by point charges. A small increase by ca. 0.3 ppm in the shielding is here observed compared to the cyclic dimer in the neat liquid. However, the chemical shift of acidic protons in cyclic trimers in the neat liquid is computed to be virtually equal to that of cyclic dimer in cyclohexane solution. Therefore, a possible proliferation of cyclic trimers in glacial acetic acid cannot account for the observed increase in the shielding of acidic protons going from cyclohexane solution to neat acetic acid, as was suggested in the literature.[85,228] The results lead to the general conclusion that the observed decrease of the chemical shift of the acidic proton by as much as 0.65 ppm as discussed above can hardly be explained by the possible prolific formation of higher–order cyclic aggregates in the neat liquid.

Regarding the chain–like aggregates of AA molecules, the QM/MM calculations for AA dimers of type **C** were first considered. The QM/MM calculations were performed for dimers **C** in neat liquid selected by imposing only the distance criterion for the C-H$\cdots$O hydrogen bond, because the content of these dimers in the neat liquid is rather low when the C-H$\cdots$O hydrogen bond definition is applied as specified in Table 9. No restrictions on the angle of this hydrogen bond were thus applied. In this way, the configuration space is significantly expanded in the case of dimer **C**. On the other hand, some of the dimers which are considered here should be seen as open dimers rather than the solid-state chain-like aggregates with a true C-H$\cdots$O hydrogen bond. As seen in Table 11, the chemical shift of the acidic proton in these dimers is

smaller as compared to that of cyclic dimers and cyclic trimers in neat liquid. Compared to the cyclic dimer in cyclohexane, the chemical shift of dimers **C** in neat liquid is smaller by 0.11 ppm, although the results in these two cases overlap within the statistical errors. The formation of aggregates of type **C** does lead to the decreased chemical shift of the acidic proton as compared to that of the cyclic dimer in cyclohexane, yet this effect is found to be too small in magnitude as compared to the corresponding experimental result.

As given in Table 11, the chemical shift of the acidic proton involved in the hydrogen bonding between the hydroxyl moieties in dimer of type **D** is lower by 1.50 ppm as compared to that of cyclic dimer in cyclohexane solution. It could be in fact expected that the acidic proton involved in the hydrogen bond between hydroxyl moieties is shielded more than that in the hydrogen bond between the hydroxyl and carbonyl groups, because the latter hydrogen bond is considerably stronger. The computed interaction energy of isolated dimer **C** is larger by ca. 2.5-3.0 kcal/mol than that of aggregate **D**, depending on the level of theory.[201,221] The acidic hydrogen is even more shielded in the monomeric AA molecules in liquid AA. We refer to AA molecule as monomer if the O-H group of it does not participate in hydrogen bonding as per definition of hydrogen bond in Table 9. It should be noted that the QM/MM calculations for the monomeric AA molecules were still carried out by promoting the nearest AA molecule to the acidic hydrogen atom of the central AA molecule to the QM region of the model.

Based on the results, it can be concluded that the observed lowering of the chemical shift of acidic protons in acetic acid molecules going from cyclohexane solution to neat AA is due to the rising relative populations of the acetic acid aggregates with hydrogen bonding between hydroxyl moieties and of monomeric AA molecules. Rather large values for the isotropic shieldings of the acidic proton in these molecules as compared to those involved in the strong hydrogen bond between hydroxyl and carbonyl groups means that even comparatively small amounts of AA monomers and of protons involved in hydrogen bonds between hydroxyl groups can make a significant effect on the overall chemical shift. Even though the hydrogen bonding between the hydroxyl and carbonyl moieties is prolific, the amount of AA molecules connected by the hydrogen bond between hydroxyl groups is not a negligible as found in the present study and literature.[201] Recent Raman spectroscopic measurements also indicate that monomeric AA molecules constitute an important structural unit of neat AA.[229]

4.4 CONCLUSIONS OF CHAPTER 4

- Cyclic dimers and higher–order cyclic associates are formed in quite significant amounts, so that ca 40 and 30% of AA molecules are involved in cyclic aggregates in OPLS and GAFF based trajectories, respectively. However, the linear aggregates are more abundant, so that ca 50 and 41% of AA molecules are involved in chain–like aggregates, respectively.

- The formation of solid-state linear-chain like aggregates in glacial AA leads to only minor lowering of the chemical shift of the acidic proton as compared to that of the cyclic dimer in cyclohexane.

- The lowering of the chemical shift of the acidic proton should originate from the rising relative populations of the acetic acid aggregates with hydrogen bonding between hydroxyl moieties and of monomeric acetic acid molecules with the diminishing concentration of cyclohexane.

Based on the results, the statement of the thesis is formulated as:

Cyclic dimers are not the dominant type of aggregation of acetic acid molecules in pure acetic acid. The experimentally observed decrease in ^{1}H NMR the chemical shift of the acidic proton of acetic acid in the binary mixture with cyclohexane with increasing molar fraction of AA is a combined effect of the proliferation of open dimers, dimers with hydrogen bonding between hydroxyl group, and monomeric acetic acid molecules.

Appendix I

Table A1: The QM/MM based ^{1}H NMR isotropic shielding constants (in ppm) of C4mim$^+$ cation in pure [C4mim][Cl] IL simulated at the temperature of 298 K. The KT3 functional and def2-TZVP basis set were used in the QM/MM calculation unless stated otherwise. All entries for shielding constants are arithemtic averages over 100 molecular configurations with central cation selected randomly in each configuration. Statistical errors calculated as sample standard deviations are given in paranthesis. The first column indicates the number of ions included to the QM region along with the central cation. Here, the three integers given in parentheses indicate the numbers of ions promoted to the QM region closest to H2, H4, and H5 atoms, respectively. Second column indicates point-charge potential used for classical C4mim$^+$ cations. Refer to Figure 12 in the main text for atom labeling in C4mim$^+$ cation. Experimental data for ^{1}H NMR chemical shifts of neat [C4mim][Cl] IL are listed in the last two lines of the table.

To QM	Pot.	H2	H4	H5	H6	H7	H8	H9	H10
(0,0,0)	—	24.01 (0.03)	24.34 (0.03)	24.30 (0.03)	27.81 (0.01)	27.49 (0.02)	29.79 (0.02)	30.45 (0.03)	30.62 (0.02)
(0,0,0)	RESP	23.59 (0.04)	23.98 (0.04)	23.99 (0.04)	27.77 (0.02)	27.35 (0.03)	29.83 (0.04)	30.46 (0.03)	30.84 (0.03)
(1,1,1)	RESP	23.08 (0.09)	23.57 (0.09)	23.57 (0.10)	27.73 (0.03)	27.32 (0.04)	29.81 (0.05)	30.44 (0.04)	30.84 (0.03)
(1,1,1)[a]	RESP	23.04 (0.10)	23.53 (0.10)	23.54 (0.10)	27.74 (0.04)	27.33 (0.04)	29.82 (0.05)	30.45 (0.04)	30.86 (0.03)
(1,1,1)[b]	RESP	23.19 (0.08)	23.70 (0.08)	23.70 (0.08)	27.77 (0.03)	27.37 (0.04)	29.85 (0.05)	30.48 (0.04)	30.86 (0.03)
(3,2,2)[a]	RESP	22.44 (0.08)	23.22 (0.10)	23.23 (0.08)	27.63 (0.05)	27.20 (0.06)	29.79 (0.05)	30.45 (0.05)	30.93 (0.03)
$R \leq 4.0$ Å[a,c]	RESP	22.53 (0.09)	23.21 (0.10)	23.11 (0.08)	27.41 (0.05)	27.10 (0.06)	29.73 (0.06)	30.54 (0.06)	30.90 (0.05)
$R \leq 4.0$ Å[a,c]	—	22.61 (0.09)	23.02 (0.10)	23.08 (0.10)	27.39 (0.06)	27.14 (0.08)	29.84 (0.07)	30.60 (0.06)	31.03 (0.06)
Exp. δ (this work)[d]		10.23	8.33	8.47	4.05	4.34	1.61	0.94	0.50
Exp. δ (Cha *et al.*)[e]		10.22	8.34	8.47	4.08	4.36	1.63	0.96	0.53

[a] – def2-TZVP basis for central cation, 3-21G basis for all additional ions.

[b] – def2-TZVP basis for central cation, 3-21++G basis for all additional ions.

[c] – all ions that are within the 4 Å distance from H2, H4 and H5 as well as from carbons 6, 8, 9 and 10 have been included to the QM region.

[d] – ^{1}H NMR chemical shifts of neat [C4mim][Cl] measured at 298 K in this work.

[e] – ^{1}H NMR chemical shifts of neat [C4mim][Cl] measured at 298 K in Phys. Chem. Chem. Phys. 16 (2012), 9591. Numerical values provided by Prof. D. Kim (Sogang University, Korea).

Bibliography

[1] Weingärtner. *Angew. Chem. Int. Ed.* **2008**, *47*, 654–670.

[2] Walden, P. *Bull. Acad. Imper. Sci. (St. Petersburg)* **1914**, *8*, 405–422.

[3] H.Hurley, F.; Wier, T. P. *J. Electrochem. Soc.* **1951**, *98*, 207–212.

[4] Welton, T. *Coord. Chem. Rev.* **2004**, *248*, 2459–2477.

[5] Wilkes, J. S.; Zaworotko, M. J. *J. Chem. Soc., Chem. Commun.* **1992**, *13*, 965–967.

[6] Wilkes, J. S. *Green Chem.* **2002**, *4*, 73–80.

[7] Wang, Y.-L.; Bin, L.; Sarman, S.; Mocci, F.; Lu, Z.-Y.; Yuan, J.; Laaksonen, A.; Fayer, M. D. *Chem. Rev.* **2020**, *120*, 5798–5877.

[8] Niedermeyer, H.; Hallett, J. P.; Villar-Garcia, I. J.; Hunt, P. A.; Welton, T. *Chem. Soc. Rev.* **2012**, *41*, 7780–7802.

[9] Soukup-Hein, R. J.; Warnke, M. M.; Armstrong, D. W. *Annu. Rev. Anal. Chem.* **2009**, *2*, 145–168.

[10] Lei, Z.; Dai, C.; Chen, B. *Chem. Rev.* **2014**, *114*, 1289–1326.

[11] MacFarlane, D. R.; Forsyth, M.; Howlett, P. C.; Kar, M.; Passerini, S.; Pringle, J. M.; Ohno, H.; Watanabe, M.; Yan, F.; Zheng, W.; Zhang, S.; Zhang, J. *Nat. Rev. Mater.* **2016**, *1*, 15005.

[12] Zhang, S.; Sun, J.; Zhang, X.; Xin, J.; Miao, Q.; Wang, J. *Chem. Soc. Rev.* **2014**, *43*, 7838–7869.

[13] Watanabe, M.; Thomas, M. L.; Zhang, S.; Ueno, K.; Yasuda, T.; Dokko, K. *Chem. Rev.* **2017**, *117*, 7190–7239.

[14] Somers, A. E.; Howlett, P. C.; MacFarlane, D. R.; Forsyth, M. A. *Lubricants* **2013**, *1*, 3–21.

[15] Janssen, C. H. C.; Macías-Ruvalcaba, N. A.; Aguilar-Martínez, M.; Kobrak, M. N. *Int. Rev. Phys. Chem.* **2015**, *34*, 591–622.

[16] Wang, Y.-L.; Li, B.; Sarman, S.; Mocci, F.; Lu, Z.-Y.; Yuan, J.; Laaksonen, A.; Fayer, M. D. *Chem. Rev.* **2020**, *120*, 5798–5877.

[17] Ma, C.; Laaksonen, A.; Liu, C.; Lu, X.; Ji, X. *Chem. Soc. Rev.* **2018**, *47*, 8685–8720.

[18] Castner, E. W.; Margulis, C. J.; Maroncelli, M.; Wishart, J. F. *Annu. Rev. Phys. Chem.* **2011**, *62*, 85–105.

[19] Wood, N.; Stephens, G. *Phys. Chem. Chem. Phys.* **2010**, *12*, 1670–1674.

[20] Yang, Z.; Pan, W. *Enzyme Microb. Technol.* **2005**, *37*, 19–28.

[21] Hallett, J. P.; Welton, T. *Chem. Rev.* **2011**, *111*, 3508–3576.

[22] Chauvin, Y.; L.Mussmann.; H.Olivier. *Angew. Chem., Int. Ed. Engl.* **1996**, *34*, 2698–2700.

[23] MacFarlane, D. R.; Tachikawa, N.; Forsyth, M.; Pringle, J. M.; Howlett, P. C.; Elliott, G. D.; Davis, J. H.; Watanabe, M.; Simon, P.; Angell, C. A. *Energy Environ. Sci.* **2014**, *7*, 232–250.

[24] Li, B.; Ma, K.; Wang, Y.-L.; Turesson, M.; Woodward, C. E.; Forsman, J. *Phys. Chem. Chem. Phys.* **2016**, *18*, 8165–8173.

[25] Zhang, W.; Wei, S.; Wu, Y.; Wang, Y.-L.; Zhang, M.; Roy, D.; Wang, H.; Yuan, J.; Zhao, Q. *ACS Nano* **2019**, *13*, 10261–10271.

[26] Sadanandhan, A. M.; Khatri, P. K.; Jain, S. L. *J. Mol. Liq.* **2019**, *295*, 111722–111729.

[27] Swatloski, R. P.; Spear, S. K.; Holbrey, J. D.; Rogers, R. D. *J. Am. Chem. Soc.* **2002**, *104*, 4974–4975.

[28] Zakeeruddin, S. M.; Grätzel, M. *Adv. Funct.Mater.* **2009**, *19*, 2187–2202.

[29] Bates, E. D.; Mayton, R.; Ntai, I.; James, H.; Davis, J. *J. Am. Chem. Soc.* **2002**, *124*, 926.

[30] HasiburRahman, M.; Siaj, M.; Larachi, F. *Chem. Eng. Process.* **2010**, *49*, 313–322.

[31] Visser, A. E.; Swatloski, R. P.; Reichert, W. M.; Mayton, R.; Sheff, S.; Wierzbicki, A.; Davis, J. H.; Rogers, R. D. *Chem. Commun.* **2001**, *0*, 135–136.

[32] Kohno, Y.; Ohno, H. *Chem. Commun.* **2012**, *48*, 7119–7130.

[33] Fujita, K.; MacFarlane, D. R.; Forsyth, M. *Chem. Commun.* **2005**, *0*, 4804–4806.

[34] Fujita, K.; Forsyth, M.; MacFarlane, D. R.; Reid, R. W.; Elliott, G. D. *Biotechnol. Bioeng.* **2006**, *94*, 1209–1213.

[35] Nanda, R. *Phys. Chem. Chem. Phys.* **2016**, *18*, 25801–25805.

[36] Gómez, E.; González, B.; Domínguez, A.; Tojo, E.; Tojo, J. *J. Chem. Eng. Data* **2006**, *51*, 696–701.

[37] Seddon, K. R.; Stark, A.; Torres, M.-J. *Pure Appl. Chem.* **2000**, *72*, 2275–2287.

[38] Stoppa, A.; Hunger, J.; Buchner, R. *J. Chem. Eng. Data* **2009**, *54*, 472–479.

[39] Buzzeo, M. C.; Hardacre, C.; Compton, R. G. *ChemPhysChem* **2006**, *7*, 176–180.

[40] Najafabadi, A. T.; Gyenge, E. *Carbon* **2014**, *71*, 58–69.

[41] Matsubara, Y.; Grills, D. C.; Kuwahara, Y. *ACS Catal.* **2015**, *5*, 6440–6452.

[42] Weingärther, H. *Angew. Chem. Int. Ed.* **2008**, *47*, 654–670.

[43] Stassen, H. K.; Ludwig, R.; Wulf, A.; Dupont, J. *Chem. Eur. J.* **2015**, *21*, 8324–8335.

[44] Köddermann, T.; Wertz, C.; Heintz, A.; Ludwig, R. *ChemPhysChem* **2006**, *7*, 1944–1949.

[45] Boruń, A. *J. Mol. Liq.* **2019**, *276*, 214–224.

[46] Giesecke, M.; M'eriguet, G.; Hallberg, F.; Fang, Y.; Stilbs, P.; Furó, I. *Phys. Chem. Chem. Phys.* **2015**, *17*, 3402–3408.

[47] Dupont, J.; Suarez, P. A. Z.; De Souza, R. F.; Burrow, R. A.; Kintzinger, J.-P. *Chem. Eur. J.* **2000**, *6*, 2377–2381.

[48] Zhou, Y.; Gong, S.; Xu, X.; Yu, Z.; Kiefer, J.; Wang, Z. *J. Mol. Liq.* **2020**, *299*, 112159–112166.

[49] Zheng, Y.-Z.; Zhou, Y.; Deng, G.; Yu, Z.-W. *J. Mol. Struct.* **2016**, *1124*, 207–215.

[50] Remsing, R. C.; Liu, Z.; Sergeyev, I.; Moyna, G. *J. Phys. Chem. B* **2008**, *112*, 7363–7369.

[51] Fumino, K.; Stange, P.; Fossog, V.; Hempelmann, R.; R.Ludwig. *Angew. Chem., Int. Ed* **2013**, *52*, 12439–12442.

[52] Zheng, Y.-Z.; Wang, N.-N.; Luo, J.-J.; Zhou, Y.; Yu, Z.-W. *Phys. Chem. Chem. Phys.* **2013**, *15*, 18055–18064.

[53] Ekka, D.; Roy, M. N. *RSC Adv.* **2014**, *4*, 19831–19845.

[54] Marekha, B. A.; Kalugin, O. N.; Bria, M.; Takamuku, T.; Gadv zurić, S.; Idrissi, A. *ChemPhysChem* **2017**, *18*, 718–721.

[55] McDaniel, J. G.; Son, C. Y. *J. Phys. Chem. B* **2018**, *122*, 7154–7169.

[56] Consorti, C. S.; Suarez, P. A. Z.; de Souza, R. F.; Burrow, R. A.; Farrar, D. H.; Lough, A. J.; Loh, W.; da Silva, L. H. M.; Dupont, J. *J. Phys. Chem. B* **2005**, *109*, 4341–4349.

[57] Cade, E. A.; Petenuci III, J.; Hoffmann, M. M. *ChemPhysChem* **2016**, *17*, 520–529.

[58] Hunger, J.; Stoppa, A.; Buchner, R.; Hefter, G. *J. Phys. Chem. B* **2008**, *112*, 12913–12919.

[59] Nama, D.; Anil Kumar, P. G.; Pregosin, P. S.; Geldbach, T. J.; Dyson, P. J. *Inorg. Chim. Acta* **2006**, *359*, 1907–1911.

[60] Cha, S.; Lee, M.; Kim, D. *ChemPhysChem* **2019**, *20*, 482–488.

[61] Sung, W.; Kim, D. *Phys. Chem. Chem. Phys.* **2016**, *18*, 27529–27535.

[62] Ludwig, R. *Angew. Chem., Int. Ed.* **2011**, *40*, 1808–1827.

[63] Schröder, U.; Wadhawan, J. D.; Compton, R. G.; Marken, F.; Suarez, P. A. Z.; Consorti, C. S.; de Souza, R. F.; Dupont, J. *New J. Chem.* **2000**, *24*, 1009–1015.

[64] Fletcher, K. A.; Pandey, S. *J. Phys. Chem. B* **2003**, *107*, 13532–13539.

[65] Freire, M. G.; Carvalho, P. J.; Fernandes, A. M.; Marrucho, I. M.; Queimada, A. J.; Coutinho, J. A. P. *J. Colloid Interface Sci.* **2007**, *314*, 621–630.

[66] Holbrey, J. D.; Seddon, K. R. *J. Chem. Soc., Dalton Trans.* **1999**, pages 2133–2140.

[67] Fujita, K.; MacFarlane, D. R.; Forsyth, M.; Yoshizawa-Fujita, M.; Murata, K.; Nakamura, N.; Ohno, H. *Biomacromolecules* **2007**, *8*, 2080–2086.

[68] Kohno, Y.; Saita, S.; Murata, K.; Nakamura, N.; Ohno, H. *Polym. Chem.* **2011**, *2*, 862–867.

[69] Bhargava, B. L.; Yasaka, Y.; Klein, M. L. *Chem. Commun.* **2011**, *47*, 6228–6241.

[70] Klimavicius, V.; Gdaniec, Z.; Kausteklis, J.; Aleksa, V.; Aidas, K.; Balevicius, V. *J. Phys. Chem. B* **2013**, *117*, 10211–10220.

[71] Guti'errez, A.; Atilhan, M.; Alcalde, R.; Trenzado, J. L.; Aparicio, S. *J. Mol. Liq.* **2018**, *255*, 199–207.

[72] Feng, S.; Voth, G. A. *Fluid Ph. Equilibria* **2010**, *294*, 148–156.

[73] Hanke, C. G.; Lynden-Bell, R. M. *J. Phys. Chem. B* **2003**, *107*, 10873–10878.

[74] Kowsari, M. H.; Mohammad Torabi, S. *J. Phys. Chem. B* **2020**, *124*, 6972–6985.

[75] Bernardes, C. E. S.; Minas da Piedade, M. E.; Canongia Lopes, J. N. *J. Phys. Chem. B* **2011**, *115*, 2067–2074.

[76] D'Angelo, P.; Serva, A.; Aquilanti, G.; Pascarelli, S.; Migliorati, V. *J. Phys. Chem. B* **2015**, *119*, 14515–14526.

[77] Jiang, W.; Wang, Y.; Voth, G. A. *J. Phys. Chem. B* **2007**, *111*, 4812–4818.

[78] Jeffrey, G. *An Introduction to Hydrogen Bonding;* Oxford University Press, 1997.

[79] Steiner, T. *Angew. Chem. Int. Ed.* **2002**, *41*, 48–76.

[80] Watson, J. D.; Crick, F. H. C. *Nature* **1953**, *171*, 737–738.

[81] Pauling, L.; Corey, R. B. *Proc. Natl. Acad. Sci. U. S. A.* **1951**, *37*, 235–240.

[82] Armstrong, G.; Buggy, M. *J. Mater. Sci.* **2005**, *40*, 547–559.

[83] Frurip, D. J.; Curtiss, L. A.; Blander, M. *J. Am. Chem. Soc.* **1980**, *102*, 2610–2616.

[84] Nahringbauer, I. *Acta Chem. Scand.* **1970**, *24*, 453–462.

[85] Clark, J. H.; Emsley, J. *J. Chem. Soc., Dalton Trans.* **1973**, *0*, 2154–2159.

[86] Bertagnolli, H. *Chem. Phys. Lett.* **1982**, *93*, 287–292.

[87] Heisler, I. A.; Mazur, K.; Yamaguchi, S.; Tominaga, K.; Meech, S. R. *Phys. Chem. Chem. Phys.* **2011**, *13*, 15573–15579.

[88] Nakabayashi, T.; Kosugi, K.; Nishi, N. *J. Phys. Chem. A* **1999**, *103*, 8595–8603.

[89] Takamuku, T.; Kyoshoin, Y.; Noguchi, H.; Kusano, S.; Yamaguchi, T. *J. Phys. Chem. B* **2007**, *111*, 9270–9280.

[90] Flakus, H. T.; Hachuła, B. *Vib. Spectrosc.* **2011**, *56*, 170–176.

[91] Lütgens, M.; Friedriszik, F.; Lochbrunner, S. *Phys. Chem. Chem. Phys.* **2014**, *16*, 18010–18016.

[92] Tokushima, T.; Horikawa, Y.; Harada, Y.; Takahashi, O.; Hiraya, A.; Shin, S. *Phys. Chem. Chem. Phys.* **2009**, *11*, 1679–1682.

[93] Wu, J. *Phys. Chem. Chem. Phys.* **2014**, *16*, 22458–22461.

[94] Fathi, S.; Bouazizi, S.; Trabelsi, S.; Gonzalez, M. A.; Bahri, M.; Nasr, S.; Bellissent-Funel, M.-C. *J. Mol. Liq.* **2014**, *196*, 69–76.

[95] Krishna, N. R., Berliner, L. J., Eds. *Biological Magnetic Resonance;* Kluwer, New York, 1998.

[96] Damodaran, K. In *Annual Reports on NMR Spectroscopy;* Elsevier Ltd, 2016; pages 215–244.

[97] Marekha, B. A.; Kalugin, O. N.; Bria, M.; Idrissi, A. *Phys. Chem. Chem. Phys.* **2015**, *17*, 23183–23194.

[98] Katsuyba, S. A.; Griaznova, T. P.; Vidis, A.; Dyson, P. J. *J. Phys. Chem.* **2009**, *113*, 5046–5051.

[99] Tsuzuki, S.; Tokuda, H.; Mikami, M. *Phys. Chem. Chem. Phys.* **2007**, *9*, 4780–4784.

[100] Noell, J.; Morokuma, K. *Chem. Phys. Lett.* **1975**, *36*, 465–469.

[101] Muller, R.; Warshel, A. *J.Phys.Chem.* **1995**, *99*, 17516–17524.

[102] Warshel, A.; Levitt, M. *J. Mol. Biol.* **1976**, *103*, 227–249.

[103] Singh, U. C.; Kollman, P. A. *J. Comput. Chem.* **1986**, *7*, 718–730.

[104] Field, M. J.; Bash, P. A.; Karplus, M. *J. Comput. Chem.* **1990**, *11*, 700–733.

[105] Thompson, M. A. *J. Phys. Chem.* **1996**, *100*, 14492–14507.

[106] Bagno, A.; D'Amico, F.; Saielli, G. *J. Phys Chem. B* **2006**, *110*, 23004–23006.

[107] Bagno, A.; D'Amico, F.; Saielli, G. *ChemPhysChem* **2007**, *8*, 873–881.

[108] Mao, J.; Steckel, J.; Yan, F.; Dhumal, N.; Kim, H.; Damodaran, K. *Phys. Chem. Chem. Phys.* **2016**, *18*, 1911–1917.

[109] Saielli, G. *Molecules* **2020**, *25*, 2085–2096.

[110] Cha, S.; Ao, M.; Sung, W.; Moon, B.; Ahlström, B.; Johansson, P.; Ouchid, Y.; Kim, D. *Phys. Chem. Chem. Phys.* **2014**, *16*, 9591–9601.

[111] Pierola, I. F.; Agzenai, Y. *J. Phys. Chem. B* **2012**, *116*, 3973–3981.

[112] Warshel, A.; Levitt, M. *J. Mol. Biol.* **1976**, *103*, 227–249.

[113] Szabo, A.; Ostlund, N. S. *Modern Quantum Chemistry: Introduction to Advanced Electronic Structure Theory;* Dover, 1996.

[114] Kongsted, J.; Osted, A.; Mikkelsen, K. V.; Christiansen, O. *Mol. Phys.* **2002**, *100*, 1813–1828.

[115] Ahlström, P.; Wallqvist, A.; Engström, S.; Jönsson, B. *Mol. Phys.* **1989**, *68*, 563–581.

[116] Sholl, D.; Steckel, J. A. *Density Functional Theory: A Practical Introduction;* Wiley, New Jersey, 2009.

[117] Hohenberg, P.; Kohn, W. *Phys. Rev.* **1964**, *136*, B864–B871.

[118] Koch, W.; Holthausen, M. C. *A Chemist's Guide to Density Functional Theory;* Wiley VCH Verlag GmbH, Weinheim, second ed., 2001.

[119] Helgaker, T.; Jaszunski, M.; Ruud, K. *Chem. Rev.* **1999**, *99*, 293–352.

[120] Gauss, J. *J. Chem. Phys.* **1993**, *99*, 3629–3643.

[121] Ruud, K.; Helgaker, T.; Kobayashi, R.; Jørgensen, P.; Bak, K. L.; Jensen, H. J. *J. Chem. Phys.* **1994**, *100*, 81788185.

[122] Olsen, J.; Jørgensen, P. *J. Chem. Phys.* **1985**, *82*, 3235–3240.

[123] Kongsted, J.; Nielsen, C. B.; Christiansen, O.; Ruud, K. *J. Chem. Phys.* **2007**, *126*, 34510–34518.

[124] Verlet, L. *Phys. Rev.* **1967**, *159*, 98–103.

[125] Hockney, R.; Eastwood, J. *Computer Simulations Using Particles;* McGraw–Hill, New York, 1981.

[126] Swope, W. C.; Anderson, H. C.; Berens, P. H.; Wilson, K. R. *J. Chem. Phys.* **1982**, *76*, 637–649.

[127] Allinger, N.; Yuh, Y.; Lii, J.-H. *J. Am. Chem. Soc.* **1989**, *111*, 8551–8565.

[128] Mayo, S.; Olafson, B.; III, W. G. *J. Phys. Chem.* **1990**, *94*, 8897–8909.

[129] Rappe, A.; Casewit, C.; Colwell, K.; III, W. G.; Skiff, W. *J. Am. Chem. Soc.* **1992**, *114*, 10024–10035.

[130] Mackerell, A.; Bashford, D.; Bellott, M.; Dunbrack, R. L.; Evanseck, J. D.; Field, M. J.; Fischer, S.; Gao, J.; Guo, H.; Ha, S.; Joseph-McCarthy, D.; Kuchnir, L.; Kuczera, K.; Lau, F. T. K.; Mattos, C.; Michnick, S.; Ngo, T.; Nguyen, D. T.; Prodhom, B.; Reiher, W. E.; Roux, B.; Schlenkrich, M.; Smith, J. C.; Stote, R.; Straub, J.; Watanabe, M.; Wiórkiewicz-Kuczera, J.; Yin, D.; Karplus, M. *J. Phys. Chem.* **1998**, *102*, 3586–3616.

[131] Cornell, W.; Cieplak, P.; Bayly, C. I.; Gould, I. R.; Merz, K. M.; Ferguson, D. M.; Spellmeyer, D. C.; Fox, T.; Caldwell, J. W.; Kollman, P. A. *J. Am. Chem. Soc.* **1995**, *117*, 5179–5197.

[132] Oostenbrink, C.; Villa, A.; Mark, A.; van Gunsteren, W. *J. Comput. Chem.* **2004**, *25*, 1656–1676.

[133] Leach, A. *Molecular modelling: Principles and applications*, Vol. 15; Addison Wesley Longman Limited, 1996.

[134] Sigfridsson, E.; Ryde, U. *J. Comput. Chem.* **1998**, *19*, 377–395.

[135] Green, D.; Tidor, B. *J. Phys. Chem. B* **2003**, *107*, 10261–10273.

[136] Steinbach, P.; Brooks, B. *J. Comput. Chem.* **1994**, *15*, 667–683.

[137] Woodcock, L. *Chem. Phys. Lett.* **1971**, *10*, 257–261.

[138] Berendsen, H.; Postma, J.; van Gunsteren, W.; DiNola, A.; Haak, J. *J. Chem. Phys.* **1984**, *81*, 3684–3690.

[139] Andersen, H. *J. Chem. Phys.* **1980**, *72*, 2384–2393.

[140] Allen, M. P.; Tildesley, D. J. *Computer Simulation of Liquids;* Oxford University Press, 1991.

[141] Nosé, S. *J. Chem. Phys.* **1984**, *81*, 511–519.

[142] Nosé, S. *Mol. Phys.* **1984**, *52*, 255–268.

[143] Hoover, W. *Phys. Rev. A* **1984**, *31*, 1695–1697.

[144] Martyna, G.; Klein, M.; Tuckerman, M. *J. Chem. Phys.* **1992**, *97*, 2635–2645.

[145] Stassen, H. K.; Ludwig, R.; Wulf, A.; Dupont, J. *Chem. Eur. J.* **2015**, *21*, 8324–8335.

[146] Boruń, A. *J. Mol. Liq.* **2019**, *276*, 214–224.

[147] Wang, H.; Liu, M.; Zhao, Y.; Xuan, X.; Zhao, Y.; Wang, J. *Sci. China Chem.* **2017**, *60*, 970–978.

[148] Balevicius, V.; Gdaniec, Z.; Aidas, K.; Tamuliene, J. *J. Phys. Chem. A* **2010**, *114*, 5365–5371.

[149] Olsen, J. M. H.; Kongsted, J. *Adv. Quantum Chem.* **2011**, *61*, 107–143.

[150] Nielsen, C. B.; Christiansen, O.; Mikkelsen, K. V.; Kongsted, J. *J. Chem. Phys.* **2007**, *126*, 154112–154130.

[151] Aidas, K.; Møgelhøj, A.; Kjær, H.; Nielsen, C. B.; Mikkelsen, K. V.; Ruud, K.; Christiansen, O.; Kongsted, J. *J. Phys. Chem. A* **2007**, *111*, 4199–4210.

[152] Aidas, K.; Mikkelsen, K. V.; Kongsted, J. *Phys. Chem. Chem. Phys.* **2010**, *12*, 761–768.

[153] Eriksen, J. J.; Olsen, J. M. H.; Aidas, K.; Ågren, H.; Mikkelsen, K. V.; Kongsted, J. *J. Comput. Chem.* **2011**, *32*, 2853–2864.

[154] Kongsted, J.; Aidas, K.; Mikkelsen, K. V.; Sauer, S. P. A. *J. Chem. Theory Comp.* **2008**, *4*, 267–277.

[155] Møgelhøj, A.; Aidas, K.; Mikkelsen, K. V.; Sauer, S. P. A.; Kongsted, J. *J. Chem. Phys.* **2009**, *130*, 134508–134520.

[156] Møgelhøj, A.; Aidas, K.; Mikkelsen, K. V.; Kongsted, J. *Chem. Phys. Lett.* **2008**, *460*, 129–136.

[157] Murugan, N. A.; Aidas, K.; Kongsted, J.; Rinkevicius, Z.; Ågren, H. *Chem. Eur. J.* **2012**, *18*, 11677–11684.

[158] Amber 12, University of California, San Francisco. Case, D. A.; Darden, T. A.; Cheatham III, T. E.; Simmerling, C. L.; Wang, J.; Duke, R. E.; Luo, R.; Walker, R. C.; Zhang, W.; Merz, K. M.; Roberts, B.; Hayik, S.; Roitberg, A.; Seabra, G.; Swails, J.; Götz, A. W.; Kolossváry, I.; Wong, K. F.; Paesani, F.; Vanicek, J.; Wolf, R. M.; Liu, J.; Wu, X.; Brozell, S. R.; Steinbrecher, T.; Gohlke, H.; Cai, Q.; Ye, X.; Wang, J.; Hsieh, M.-J.; Cui, G.; Roe, D. R.; Mathews, D. H.; Seetin, M. G.; Salomon-Ferrer, R.; Sagui, C.; Babin, V.; Luchko, T.; Gusarov, S.; Kovalenko, A.; Kollman, P. A. **2012**.

[159] Hehre, W. J.; Ditchfield, R. J.; Pople, J. A. *J. Chem. Phys.* **1972**, *56*, 2257–2261.

[160] Hariharan, P. C.; Pople, J. A. *Theor. Chim. Acta* **1973**, *28*, 213–222.

[161] Gaussian 09 Revision A.02, Gaussian Inc. Wallingford CT. Frisch, M. J.; Trucks, G. W.; Schlegel, H. B.; Scuseria, G. E.; Robb, M. A.; Cheeseman, J. R.; Scalmani, G.; Barone, V.; Mennucci, B.; Petersson, G. A.; Nakatsuji, H.; Caricato, M.; Li, X.; Hratchian, H. P.; Izmaylov, A. F.; Bloino, J.; Zheng, G.; Sonnenberg, J. L.; Hada, M.; Ehara, M.; Toyota, K.; Fukuda, R.; Hasegawa, J.; Ishida, M.; Nakajima, T.; Honda, Y.; Kitao, O.; Nakai, H.; Vreven, T.; Montgomery, J. A., J.; Peralta, J. E.; Ogliaro, F.; Bearpark, M.;

Heyd, J. J.; Brothers, E.; Kudin, K. N.; Staroverov, V. N.; Kobayashi, R.; Normand, J.; Raghavachari, K.; Rendell, A.; Burant, J. C.; Iyengar, S. S.; Tomasi, J.; Cossi, M.; Rega, N.; Millam, J. M.; Klene, M.; Knox, J. E.; Cross, J. B.; Bakken, V.; Adamo, C.; Jaramillo, J.; Gomperts, R.; Stratmann, R. E.; Yazyev, O.; Austin, A. J.; Cammi, R.; Pomelli, C.; Ochterski, J. W.; Martin, R. L.; Morokuma, K.; Zakrzewski, V. G.; Voth, G. A.; Salvador, P.; Dannenberg, J. J.; Dapprich, S.; Daniels, A. D.; Farkas, O.; Foresman, J. B.; Ortiz, J. V.; Cioslowski, J. **2009**.

[162] Liu, Z.; Huang, S.; Wang, W. *J. Phys. Chem. B* **2004**, *108*, 12978–12989.

[163] Cornell, W. D.; Cieplak, P.; Bayly, C. I.; Gould, I. R.; Merz, K. M.; Ferguson, D. M.; Spellmeyer, D. C.; Fox, T.; Caldwell, J. W.; Kollman, P. A. *J. Am. Chem. Soc.* **1995**, *117*(19), 5179–5197.

[164] Wang, J.; Wolf, R. M.; Caldwell, J. W.; Kollman, P. A.; Case, D. A. *J. Comp. Chem.* **2004**, *25*(9), 1157–1174.

[165] Bayly, C. I.; Cieplak, P.; Cornell, W.; Kollman, P. A. *J. Phys. Chem.* **1993**, *97*(40), 10269–10280.

[166] Wang, J.; Wang, W.; Kollman, P. A.; Case, D. A. *J. Mol. Graphics Mod.* **2006**, *25*, 247–260.

[167] Jorgensen, W. L. *J. Am. Chem. Soc.* **1981**, *103*, 335–340.

[168] Martínez, L.; Andrade, R.; Birgin, E. G.; Martínez, J. M. *J. Comp. Chem.* **2009**, *30*, 2157–2164.

[169] Ryckaert, J.-P.; Ciccotti, G.; Berendsen, H. J. C. *J. Comp. Phys.* **1977**, *23*, 327–341.

[170] Miyamoto, S.; Kollman, P. A. *J. Comp. Chem.* **1992**, *13*, 952–962.

[171] Becke, A. D. *J. Chem. Phys.* **1993**, *98*, 5648–5652.

[172] Kendall, R. A.; Dunning, Jr., T. H.; Harrison, R. J. *J. Chem. Phys.* **1992**, *96*, 6796–6806.

[173] Dunning, T. H. *J. Chem. Phys.* **1989**, *90*, 1007–1023.

[174] Adamo, C.; Barone, V. *J. Chem. Phys.* **1999**, *110*, 6158.

[175] Keal, T. W.; Tozer, D. J. *J. Chem. Phys.* **2004**, *121*, 5654–5660.

[176] Weigend, F.; Ahlrichs, R. *Phys. Chem. Chem. Phys.* **2005**, *7*, 3297–3305.

[177] Woon, D. E.; Dunning Jr., T. H. *J. Chem. Phys.* **1995**, *103*, 4572–4585.

[178] The Dalton quantum chemistry program system. Aidas, K.; Angeli, C.; Bak, K. L.; Bakken, V.; Bast, R.; Boman, L.; Christiansen, O.; Cimiraglia, R.; Coriani, S.; Dahle, P.; Dalskov, E. K.; Ekström, U.; Enevoldsen, T.; Eriksen, J. J.; Ettenhuber, P.; Fernández, B.; Ferrighi, L.; Fliegl, H.; Frediani, L.; Hald, K.; Halkier, A.; Hättig, C.; Heiberg, H.; Helgaker, T.; Hennum, A. C.; Hettema, H.; Hjertenæs, E.; Høst, S.; Høyvik, I.-M.; Iozzi, M. F.; Jansík, B.; Jensen, H. J. Aa.; Jonsson, D.; Jørgensen, P.; Kauczor, J.; Kirpekar, S.; Kjærgaard, T.; Klopper, W.; Knecht, S.; Kobayashi, R.; Koch, H.; Kongsted, J.; Krapp, A.; Kristensen, K.; Ligabue, A.; Lutnæs, O. B.; Melo, J. I.; Mikkelsen, K. V.; Myhre, R. H.; Neiss, C.; Nielsen, C. B.; Norman, P.; Olsen, J.; Olsen, J. M. H.; Osted, A.; Packer, M. J.; Pawlowski, F.; Pedersen, T. B.; Provasi, P. F.; Reine, S.; Rinkevicius, Z.; Ruden, T. A.; Ruud, K.; Rybkin, V. V.; Sałek, P.; Samson, C. C. M.; de Merás, A. S.; Saue, T.; Sauer, S. P. A.; Schimmelpfennig, B.; Sneskov, K.; Steindal, A. H.; Sylvester-Hvid, K. O.; Taylor, P. R.; Teale, A. M.; Tellgren, E. I.; Tew, D. P.; Thorvaldsen, A. J.; Thøgersen, L.; Vahtras, O.; Watson, M. A.; Wilson, D. J. D.; Ziolkowski, M.; Ågren, H. **2014**.

[179] Matthews, D. A.; Cheng, L.; Harding, M. E.; Lipparini, F.; Stopkowicz, S.; Jagau, T.-C.; Szalay, P. G.; Gauss, J.; Stanton, J. F. *J. Chem. Phys.* **2020**, *152*, 214108–214143.

[180] Kongsted, J.; Nielsen, C. B.; Mikkelsen, K. V.; Christiansen, O.; Ruud, K. *J. Chem. Phys.* **2007**, *126*, 034510–034518.

[181] Tomasi, J.; Mennucci, B.; Cammi, R. *Chem. Rev.* **2005**, *105*, 2999–3093.

[182] Breneman, C. M.; Wiberg, K. B. *J. Comp. Chem.* **1990**, *11*, 361–373.

[183] Chen, S.; Vijayaraghavan, R.; MacFarlane, D. R.; Izgorodina, E. I. *J. Phys. Chem. B* **2013**, *117*, 3186–3197.

[184] Hunt, P. A.; Gould, I. R. *J. Phys. Chem. A* **2006**, *110*, 2269–2282.

[185] Hunt, P. A.; Kirchner, B.; Welton, T. *Chem. Eur. J.* **2006**, *12*, 6762–6775.

[186] Kohno, Y.; Ohno, H. *Chem. Commun.* **2012**, *48*, 7119–7130.

[187] Ghoshdastidar, D.; Senapati, S. *J. Phys. Chem. B* **2015**, *119*, 10911–10920.

[188] Abe, H.; Takekiyo, T.; Shigemi, M.; Yoshimura, Y.; Tsuge, S.; Hanasaki, T.; Ohishi, K.; Takata, S.; Suzuki, J. *J. Phys. Chem. Lett.* **2014**, *5*, 1175–1180.

[189] Wang, J.; Liu, Y.; Li, W.; Gao, G. *RSC Adv.* **2018**, *8*, 28604–28612.

[190] Amber 18, University of California, San Francisco. Case, D. A.; Ben-Shalom, I. Y.; Brozell, S. R.; Cerutti, D. S.; Cheatham, III, T. E.; Cruzeiro, V. W. D.; Darden, T. A.; Duke, R. E.; Ghoreishi, D.; Gilson, M. K.; Gohlke, H.; Goetz, A. W.; Greene, D.; Harris, R.; Homeyer, N.; Huang, Y.; Izadi, S.; Kovalenko, A.; Kurtzman, T.; Lee, T. S.; LeGrand, S.; Li, P.; Lin, C.; Liu, J.; Luchko, T.; Luo, R.; Mermelstein, D.; Merz, K. M.; Miao, Y.; Monard, G.; Nguyen, C.; Nguyen, H.; Omelyan, I.; Onufriev, A.; Pan, F.; Qi, R.; Roe, D.; Roitberg, A.; Sagui, C.; Schott-Verdugo, S.; Shen, J.; Simmerling, C. L.; Smith, J.; Salomon-Ferrer, R.; Swails, J.; Walker, R. C.; Wang, J.; Wei, H.; Wolf, R. M.; Wu, X.; Xiao, L.; York, D. M.; Kollman, P. A. **2018**.

[191] Canongia Lopes, J. N.; Deschamps, J.; Pádua, A. A. H. *J. Phys. Chem. B* **2004**, *108*, 2038–2047.

[192] Canongia Lopes, J. N.; Pádua, A. A. H. *J. Phys. Chem. B* **2006**, *110*, 19586–19592.

[193] Horn, H. W.; Swope, W. C.; Pitera, J. W.; Madura, J. D.; Dick, T. J.; Hura, G. L.; Head-Gordon, T. *J. Chem. Phys.* **2004**, *120*, 9665–9678.

[194] Gordon, M. S.; Stephen Binkley, J.; Pople, J. A.; Pietro, W. J.; Hehre, W. J. *J. Am. Chem. Soc.* **1982**, *104*, 2797–2803.

[195] Verma, A.; Stoppelman, J. P.; McDaniel, J. G. *Int. J. Mol. Sci.* **2020**, *21*, 403–427.

[196] Katsyuba, S. A.; Griaznova, T. P.; Vidiš, A.; Dyson, P. J. *J. Phys. Chem. B* **2009**, *113*, 5046–5051.

[197] Hardacre, C.; Holbrey, J. D.; McMath, S. E. J.; Bowron, D. T.; Soper, A. K. *J. Chem. Phys.* **2003**, *118*, 273–278.

[198] Cossi, M.; Crescenzi, O. *J. Chem. Phys.* **2003**, *118*, 8863–8873.

[199] Chen, S.; Izgorodina, E. I. *Phys. Chem. Chem. Phys.* **2017**, *19*, 17411–17425.

[200] Briggs, J. M.; Nguyen, T. B.; Jorgensen, W. J. *J. Phys. Chem.* **1991**, *95*, 3315–3322.

[201] Xu, W.; Yang, J. *J. Phys. Chem. A* **2010**, *114*, 5377–5388.

[202] Reeves, L. W. *Can. J. Chem.* **1961**, *39*, 1711–1720.

[203] Capparelli, A. L.; Hertz, H. G.; Tutsch, R. *J. Phys. Chem.* **1978**, *82*, 2023–2029.

[204] Goldman, M. A.; Emerson, M. T. *J. Phys. Chem.* **1973**, *77*, 2295–2299.

[205] Kimtys, L. L.; Balevičius, V. J. *Adv. Mol. Relax. Int. Pr.* **1979**, *15*, 151–161.

[206] Tjahjono, M.; Cheng, S.; Li, C.; Garland, M. *J. Phys. Chem. A* **2010**, *114*, 12168–12175.

[207] Tjahjono, M.; Allian, A. D.; Garland, M. *J. Phys. Chem. B* **2008**, *112*, 6448–6459.

[208] Davies, J. A.; Hanson-Heine, M. W. D.; Besley, N. A.; Shirley, A.; Trowers, J.; Yang, S.; Ellis, A. M. *Phys. Chem. Chem. Phys.* **2019**, *21*, 13950–13958.

[209] Reščič, J.; Linse, P. *J. Comp. Chem.* **2015**, *36*, 1259–1274.

[210] Jorgensen, W. L.; Maxwell, D. S.; Tirado-Rives, J. *J. Am. Chem. Soc.* **1996**, *118*, 11225–11236.

[211] Maçôas, E. M. S.; Khriachtchev, L.; Pettersson, M.; Fausto, R.; Räsänen, M. *J. Am. Chem. Soc.* **2003**, *125*, 16188–16189.

[212] Dixon, D. A.; Komornicki, A. *J. Phys. Chem.* **1990**, *94*, 5630–5636.

[213] Squillacote, M.; Sheridan, R. S.; Chapman, O. L.; Anet, F. A. L. *J. Am. Chem. Soc.* **1975**, *97*, 3244–3246.

[214] Chandra Singh, U.; Kollman, P. A. *J. Comput. Chem.* **1984**, *5*, 129–145.

[215] Tanaka, Y.; Hosokawa, H.; Kubota, H.; Makita, T. *Int. J. Thermophys.* **1991**, *12*, 245–264.

[216] Hafez, M.; Hartland, S. *J. Chem. Eng. Data* **1976**, *21*, 179–182.

[217] Aidas, K.; Olsen, J. M. H.; Kongsted, J.; Ågren, H. *J. Phys. Chem. B* **2013**, *117*, 2069–2080.

[218] Berendsen, H. J. C.; Postma, J. P. M.; van Gunsteren, W. F.; DiNola, A.; Haak, J. R. *J. Chem. Phys.* **1984**, *81*, 3684–3690.

[219] Prada-Gracia, D.; Shevchuk, R.; Rao, F. *J. Chem. Phys.* **2013**, *139*, 084501–084507.

[220] Kumar, R.; Schmidt, J. R.; Skinner, J. L. *J. Chem. Phys.* **2007**, *126*, 204107–204119.

[221] Chocholoušová, J.; Vacek, J.; Hobza, P. *J. Phys. Chem. A* **2003**, *107*, 3086–3092.

[222] Nakabayashi, T.; Sato, H.; Hirata, F.; Nishi, N. *J. Phys. Chem. A* **2001**, *105*, 245–250.

[223] Nakabayashi, T.; Nishi, N. *J. Phys. Chem. A* **2002**, *106*, 3491–3500.

[224] Riniker, S.; Horta, B. A. C.; Thijssen, B.; Gupta, S.; van Gunsteren, W. F.; Hünenberger, P. H. *ChemPhysChem* **2012**, *13*, 1182–1190.

[225] Gavezzotti, A. *Chem. Eur. J.* **1999**, *5*, 567–576.

[226] Steiner, T. *Chem. Commun.* **1997**, *0*, 727–734.

[227] Nochebuena, J.; Cuautli, C.; Ireta, J. *Phys. Chem. Chem. Phys.* **2017**, *19*, 15256–15263.

[228] Akitt, J. W. *J. Chem. Soc., Faraday Trans. 1* **1977**, *73*, 1622–1628.

[229] Wu, J. *Phys. Chem. Chem. Phys.* **2014**, *16*, 22458–22461.

NOTES

NOTES

NOTES

Vilnius University Press
Saulėtekio ave. 9, LT-10222 Vilnius
El. p. info@leidykla.vu.lt, www.leidykla.vu.lt
bookshop.vu.lt, journals.vu.lt
Print run copies 20